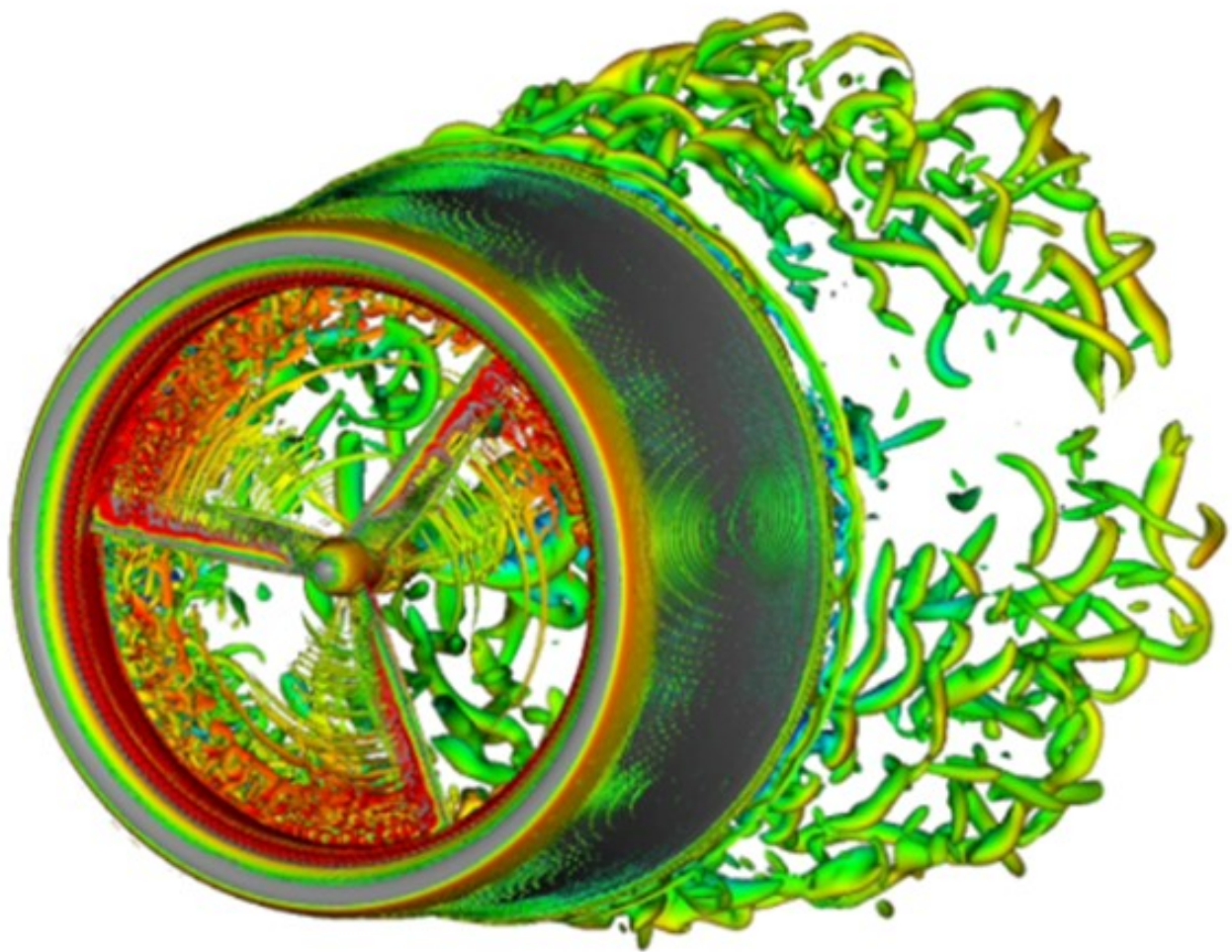


Computational analysis of ducted wind turbines noise

Luca Anselmi



Computational analysis of ducted wind turbines noise

by

L. Anselmi

to obtain the degree of Master of Science
at the Delft University of Technology,
to be defended publicly on Monday 4th December, 2017 at 9:30 AM.

Student number: 4474929
Project duration: February 27th, 2017 – December 4th, 2017
Thesis committee: Dr. F. Avallone, TU Delft, supervisor
Prof.dr. D. Casalino, TU Delft
Dr.ir. M. Snellen, TU Delft
Dr.ir. S. Mertens, WindChallenge

An electronic version of this thesis is available at <http://repository.tudelft.nl/>.

Summary

As the suitable locations for large wind farms in the mainland are limited, wind energy generation in the urban environment is gaining interest. The Diffuser Augmented Wind Turbine (DAWT) is a promising concept where the turbine is embedded into an airfoil-shaped diffuser (also named shroud or duct), which has the function of increasing the mass flow across the rotor. Such device is designed to overcome the low wind speed present in urban locations.

Noise regulations represent a limit to the installation of wind turbines in urban areas. To the author's knowledge, the far-field noise generated by DAWTs has been investigated only by Hashem et al. [31], who reported noise increase up to 20 dB compared to unaugmented turbines. However, the noise generation mechanisms are not clear yet. Furthermore, only partial data [15] on the fluid-dynamic behaviour of DAWT when operating in yawed inflow conditions are present, with no information on the noise pattern.

The current study investigates both the fluid-dynamic and acoustic fields for a ducted wind turbine using a computational approach. The commercial DonQi turbine is taken as reference. The fluid-dynamic flow field is computed using the Lattice-Boltzmann Method solver Exa PowerFLOW. The Ffowcs-Williams and Hawkings (FW-H) analogy is employed to compute the far-field noise. Three cases are investigated: the ducted turbine at 0° and 7.5° yaw angles and the unducted turbine at 0° yaw angle.

The fluid-dynamic analysis reveals that the presence of the diffuser accelerates the flow in the tip region, resulting in a significant increase of the thrust and the power produced by the turbine. In correspondence, the tip vortices present a higher intensity. These vortices interact with the boundary layer of the diffuser and form long vortical structures convected beyond the diffuser trailing edge. The presence of a yaw angle creates a non-axisymmetrical velocity pattern at the rotor disk, resulting in a power drop of 10.8%. However, no stall on the blades is detected. Contrarily to the observations by Cresswell et al. [15], a separation region is formed on the diffuser suction side.

Regarding the far-field noise, the directivity pattern for the unducted turbine presents a zone of low noise above the rotor. The addition of a diffuser causes a noise increase by approximately 5 dB upwind and downwind and by up to 15 dB in the low noise region, resulting in a more uniform noise distribution. This effect is ascribed to the higher flow speed in the tip region and to the diffraction of acoustic waves by the diffuser. Increasing the yaw angle to 7.5° is found not to have a relevant impact on the far-field noise.

Acknowledgements

Delft, 4th December 2017

As every journey, also this one must come to an end. These nine months working on my thesis project close a chapter which started two years ago. If I look back at summer 2015, when I left my beloved Cantalupa, I realise how many things have changed. These two years in Delft (and Munich) have changed me so much, both from a personal and professional point of view.

I will always look back at this period of this life with great joy and satisfaction for all the targets that I achieved, all the memories I made and all the amazing experiences I have been through. There are people without which I would not be where I am right now, to whom I owe my deep gratitude.

First of all, I would like to thank my supervisor Dr. Francesco Avallone, who showed a great motivation and interest towards my work from the first to the last day of the project. His availability for any issue, his expertise, his patience and his advice about any matter (also non-technical) were for sure larger than it usually happens for MSc students. I am also indebted to Prof.dr. Damiano Casalino, who decisively helped me to improve the quality of my work and to have a deeper understanding of the phenomena happening in my research. Then, I am grateful to Dr.ir. Mirjam Snellen and Dr.ir. Sander Mertens for the interest shown towards my study by being part of my Thesis Committee. Finally, I am thankful to all the academic and support staff which contributed to my education in these two years.

Completing my studies would not have possible without all the friends that I met during these two years. Name all of you would be a titanic effort, but I have no doubt you will recognise yourself in the following list. Thanks to all the people in BEST Delft and to my friends in BEST across Europe. The memories, the experience, the personal development and the fun moments that I had with you are simply unaccountable. Thanks to my local Italian family, the whole 'Karting & More' group, for all the enjoyable moments, chats and dinners that I had with you. Thanks to my friends from the departed office room 6.08, with whom I shared countless coffees, interesting discussions and pleasant talks. Thanks to my friends in Italy, in Cantalupa and around, that make me feel as if I never left every time I was coming back home. Thanks to my fellows from SET and to all my friends that are not in these groups but that know to have a place in my life.

Finally and foremost, I would like to acknowledge my family. Nothing would have been possible without your unconditional support during these years, which allowed me following my dreams and becoming the person I am right now.

Luca

Contents

Summary	iii
1 Introduction	1
1.1 Background	1
1.2 Problem statement and research goals	2
1.3 Approach overview.	3
1.4 Thesis outline.	4
2 Basic concepts of aeroacoustics	5
2.1 Acoustics basics	5
2.1.1 What is sound.	5
2.1.2 How to measure sound.	5
2.1.3 Sound spectra.	7
2.2 Sound propagation and generation.	8
2.2.1 Wave equation for propagation	8
2.2.2 Wave equation for sound sources	9
2.2.3 Lighthill analogy	9
2.2.4 Ffowcs Williams - Hawkings (FW-H) analogy.	10
2.2.5 Effect of surfaces	11
2.2.6 Doppler effect and convective amplification.	11
2.3 Wind turbine noise.	12
2.3.1 Aerodynamic noise sources	12
2.4 Duct modes.	13
3 Diffuser Augmented Wind Turbines	15
3.1 History and literature	15
3.1.1 History.	15
3.1.2 DonQi Urban Windmill	16
3.1.3 Analytic approaches	18
3.1.4 Computational results	18
3.1.5 Experimental results	19
3.2 DAWT theory	20
3.2.1 Working principles	20
3.2.2 Useful properties	20
3.2.3 Performance of yawed turbine.	22
4 Methodology	25
4.1 Flow solver	25
4.1.1 Basics of Lattice-Boltzmann Methods.	25
4.1.2 Lattice creation in PowerFLOW	29
4.2 Acoustic solver	31
4.2.1 FW-H analogy implementation	31
4.2.2 Sampling criteria	31

5	Setup	33
5.1	Geometry	33
5.2	Coordinate system	37
5.3	Lattice	39
5.4	Acoustic settings	42
5.5	Simulation settings.	45
5.5.1	Global characteristics	45
5.5.2	Boundary conditions	46
5.5.3	Time-convergence of simulations.	47
5.5.4	Measurements	47
6	Validation	51
6.1	Forces convergence	51
6.2	Acoustic convergence	53
6.3	Diffuser pressure coefficient.	55
7	Results - Fluid-dynamics	57
7.1	Thrust and power	57
7.2	Average field	59
7.2.1	Symmetry planes	60
7.2.2	Axial planes	61
7.3	Instantaneous field	63
8	Results - Acoustics	67
8.1	Sound Power Level Spectrum	67
8.1.1	Comparison between FW-H solid and FW-H permeable	67
8.1.2	PWL spectrum in the three cases	67
8.2	Overall sound pressure level and directivity	70
8.3	Circumferential Fourier modes and duct modes analysis.	72
9	Conclusions and recommendations	75
9.1	Conclusions.	75
9.2	Recommendations	76
	Bibliography	79

Nomenclature

Latin lower case symbol list

Symbol	Unit	Description
c	m/s	Lattice speed
c	m/s	Speed of sound
dx	m	Voxel length
\mathbf{e}	m/s	Microscopic velocity
f	Hz	Frequency
f	$[-]$	Particles distribution function
\mathbf{f}	N	External forces density
f_{ac}	Hz	Acoustic data sampling frequency
f_{fl}	Hz	Fluid data sampling frequency
f_s	Hz	Sampling frequency
h	m	Tip clearance
l	m	Blade chord
k	$[-]$	Axial eigenvalue
k	$[-]$	Von Karman constant
m	kg/s	Mass source
m	$[-]$	Circumferential mode
p	Pa	Acoustic pressure
r	m	Radial distance from rotor axis
r_s	m	Distance from origin
ts	s	Timestep
t_w	$kgm^{-1}s^{-2}$	Shear wall stress
\mathbf{u}	m/s	Flow velocity
u^*	ms	Friction velocity
u^+	$[-]$	Dimensionless velocity
\mathbf{v}	m/s	Velocity vector
\mathbf{x}	m/s	Particle position
y	m	Distance from the wall
y^+	$[-]$	Dimensionless wall distance
\mathbf{w}	$[-]$	Particle collision weights

Latin upper case symbol list

Symbol	Unit	Description
B	[-]	Number of blades
C_p	[-]	Pressure coefficient
C_P	[-]	Power coefficient
C_t	[-]	Local thrust coefficient
C_T	[-]	Rotor thrust coefficient
D	[-]	Doppler factor
H	[-]	Heaviside function
$H1$	m	Hub ellipsoid of revolution length
$H2$	m	Hub cylinder length
I	Wm^{-2}	Sound intensity
\mathbf{I}	N	Unit stress tensor
L	m	Diffuser chord
M	[-]	Mach number
Nu	[-]	Nusselt number
P	W	Rotor power
\mathbf{P}	N	Fluid stress tensor
P_{ac}	W	Total sound power
Q	Nm	Rotor torque
R	m	Rotor radius
R_{hub}	m	Hub radius
S	m^2	Integration surface
T	N	Rotor thrust
T	K	Temperature
$T_{i,j}$	N	Lighthill stress tensor
U	m/s	Axial speed
V	m/s	Velocity magnitude

Greek symbol list

Symbol	Unit	Description
α	[-]	Radial eigenvalue
Γ	$m s^{-3}$	Circulation
Γ	K^{-1}	Acoustic damping
λ	m	Wavelength
ρ	$kg m^{-3}$	Air density
Σ	m^2	FW-H surface
τ	[-]	Relaxation time
τ	N	Viscous stress tensor
Ψ	m^3	FW-H volume
ω	s^{-1}	Vorticity magnitude
ω_h	s^{-1}	Harmonic frequency
Ω	s^{-1}	Collision operator
Ω	[-]	Rotational speed

Subscripts and superscripts

<i>bare</i>	Relative to bare turbine
<i>DAWT</i>	Relative to ducted turbine
<i>diff</i>	Relative to diffuser
<i>eq</i>	Relative to equilibrium distribution
∞	Free-stream conditions
<i>in</i>	Diffuser inlet location
<i>m</i>	Relative to mode <i>m</i>
<i>max</i>	Maximum
<i>min</i>	Minimum
<i>obs</i>	Relative to observer location
<i>out</i>	Diffuser outlet location
<i>r</i>	Relative to rotor
<i>ref</i>	Reference value
<i>rms</i>	Root-mean-square
<i>source</i>	Relative to noise source
<i>thr</i>	Diffuser throat location
0	Standard conditions

Acronyms

BEM	Blade Element Momentum
BPF	Blade Passing Frequency
CAA	Computational AeroAcoustics
CAD	Computer Aided Drafting
CAE	Computer Aided Engineering
CFD	Computational Fluid Dynamics
DAWT	Diffuser Augmented Wind Turbine
FFT	Fast Fourier Transform
LES	Large Eddies Simulation
OASPL	OverAll Sound Pressure Level
PWL	sound PoWer Level
RANS	Reynolds-Averaged-Navier-Stokes
SPL	Sound Pressure Level
TSR	Tip-Speed-Ratio
URANS	Unsteady Reynolds-Averaged-Navier-Stokes
VLES	Very Large Eddies Simulation

Introduction

1.1. Background

The problem of energy generation is widely considered one of the biggest challenges for humanity in the next future.

On one side, the energy consumption in the world is increasing and it is expected to increase in the next years. In 2050, the world energy requirements might even double the current energy consumption [2]. On the other, the contemporary energy production system is mostly based on fossil fuels, such as oil, coal and natural gas [24]. These production methods have been proven to affect the climate, representing a threat to the environment and future human generations. A large-scale, fast and sustainable development of new energy production systems is therefore needed. These reasons brought to several international agreements to fight the climate change. The latest is the Paris climate agreement, signed in April 2016 by 195 countries, with the target of keeping the global rise of the temperature below 2 degrees compared to pre-industrial levels.

Wind energy has emerged in the last years as a reliable resource to represent a significant share of the power production in the near future. In EU, in 2016 wind energy covered 10.4 % of the electricity demand and 51 % of the total power capacity installations [20]. The share of electricity consumption provided by wind power is expected to rise to 29.6 % in 2030, offering more than 550,000 jobs [21].

Nowadays, most of the wind power comes from wind farms in the mainland, featuring wind turbines with rated power in the order of 500 kW to 3-4 MW. However, onshore wind farms can be located only on specific sites, which must have abundant wind resource, respect acoustic and visual regulations and not be too far from the locations where the energy is consumed. Since such sites are limited, other locations need to be considered.

In particular, there are two types of locations where wind energy is more suitable to expand in the next years. The first is offshore: large-scale wind farms can be built in the sea to exploit the higher wind speeds of such an open environment, employing turbines with size up to 8 MW. The second is urban locations: these involve a smaller scale of wind production, in the order of 500 W to 10 kW, with the critical advantage of producing the electricity very near to where it is consumed.

Indeed, urban wind energy allows both the reduction of losses in electric transportation and the direct use of the electricity from the customer. The latter entails that the produced electricity is no longer inserted into the grid, but directly stored or consumed, which can result in an economic benefit for the customer.

However, the urban environment places challenges in wind power generation. The presence of buildings increases the surface roughness, leading to lower wind speeds and higher turbulence. Furthermore, the urban environment limits the maximum height of the turbine and it is subject

to noise limitations. Several solutions have been proposed during the years, as using buildings to concentrate the wind resource in the so-called Building Augmented Wind Turbines (BAWTs), and as turbines with vertical axis of rotation, named Vertical Axis Wind Turbines (VAWTs) [43]. Examples of such designs are shown in Figure 1.1.

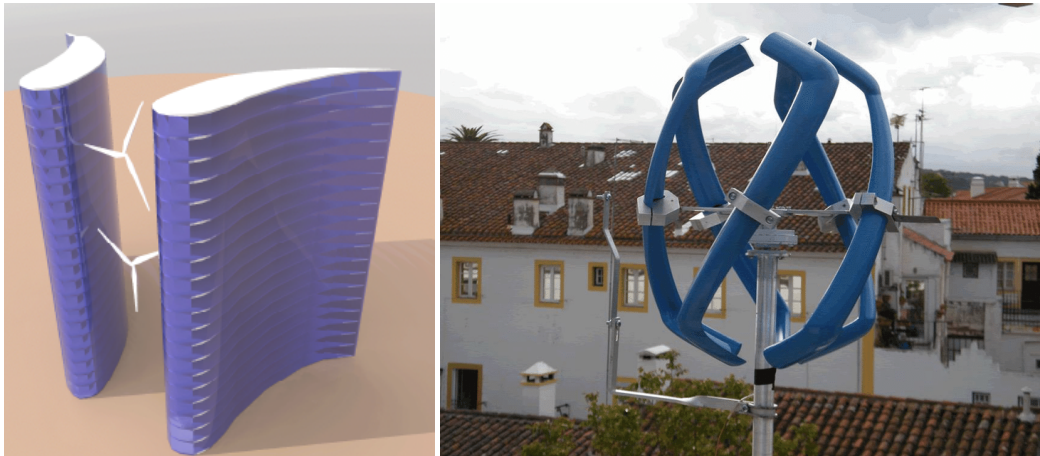


Figure 1.1: Artist impression of Building Augmented Wind Turbine (left) and picture of a Vertical Axis Wind Turbine (right) [43]

Another wind turbine concept that is suitable for urban sites is the Diffuser Augmented Wind Turbine (DAWT), which is the main subject of the current research. The basic idea behind DAWTs is to embed the turbine within a diffuser (also named duct or shroud) in order to accelerate the wind and hence increase the mass flow across the rotor, to compensate the low wind speeds. This device allows exceeding the Betz limit referred to rotor area, i.e. the maximum fraction of power which can be extracted by a rotor compared to the power of the wind, which has been shown to be equal to 0.593 [62]. DAWTs find their natural implementation in small-scale turbines: on a higher scale, the high wind speeds would cause a significant increase in the loads experienced by the turbine. This would require higher costs in the structure, including rotor, diffuser and tower, making it not economically convenient [39].

Surprisingly, despite being mainly apt for urban sites, where noise regulations are a significant limitation to power output, no acoustic study about DAWT can be found in the literature. A detailed analysis of the noise produced by these turbines is therefore needed with a view to a possible wide-scale implementation.

1.2. Problem statement and research goals

Despite the fact that research on Diffuser Augmented Wind Turbines has been ongoing for more than 50 years, several crucial open questions remain. In fact, the scientific community has not agreed yet on a thorough aerodynamic theory that can explain the behaviour of DAWT.

The information available is relative to a wide variety of design and implementations, making difficult to compare the results and coming to definitive conclusions. Furthermore, a joint optimisation of the diffuser geometry and the blades geometry represents a challenging task, and in the literature there is no evidence that it has ever been performed. 1-D momentum models have been developed, but they are built on straightforward assumptions that cannot explain the 3-D behaviour of a turbine. Semi-analytical models as the one by Bontempo and Manna [6] need complete datasets to be used as a reference, which are not available in the literature.

The DonQi Urban Windmill, which will be described in detail in Paragraph 3.1.2, is used as a reference case. There is no study in literature about this design in yawed inflow condition, i.e. when the angle between the wind direction and the rotor axis (defined as yaw angle) is not equal to zero.

Acoustic effects can differ to a great extent with the presence of a yaw angle [46] and such state is recurrent in the lifecycle of a DAWT, which is typically too heavy to rotate with the change in wind direction. Therefore, the DonQi Windmill needs to be simulated in yawed conditions.

For what concerns the acoustic analysis, it is worth mentioning that, even in the absence of a dedicated study, researchers have contrasting opinions on the noise produced by a DAWT. The first trend evaluates that a DAWT would be less noisy than an analogous turbine with same rotor geometry and no duct. The diffuser would indeed reduce the magnitude of the tip vortices, which are a relevant source of noise, thanks to the small gap between the inner side of the diffuser and the blade tip [39] [49] [56]. In other studies, there is the opinion that the accelerated inflow compared to a non-ducted wind turbine would result in an increase of the vorticity shed by the blades and hence of the noise produced by the turbine [31] [50]. Clearly, it emerges that a study on significant cases would give precious insights into the involved phenomena.

Given these premises, the goals of the current study are the following.

- *Create a baseline setup*

Before being able to run the simulations and obtaining the computational results, it is necessary to create a setup for the case. The setup is built so that it can be used for the future research activity on the DonQi turbine.

- *Analyse the fluid-dynamic flow field in nominal conditions*

The flow field in nominal conditions, i.e. with yaw angle of 0° , is investigated, with a focus on the difference between the fields with and without a diffuser. Insights into the power and thrust produced by the device are given. The velocity field and the characteristics of the vortices are discussed, in order to explain the performance of the turbine and make predictions on the noise pattern. The flow field analysis results in a complete dataset which can be used in semi-analytical models.

- *Analyse the performance of the DonQi turbine in yawed conditions*

A few designs of diffuser augmented wind turbine has been found not to decrease their performance under small yaw angles [15]. The DonQi turbine is tested with a yaw angle of 7.5° and its flow characteristics are compared with the case with nominal conditions.

- *Analyse the noise characteristics*

The far-field noise in both nominal and yawed conditions are analysed and compared, including the sound power level of the device and its noise directivity pattern. A modal analysis is performed to envision simple insights into the far-field noise characteristics.

1.3. Approach overview

In order to perform an acoustic analysis of the DonQi windmill, a computational aeroacoustics (CAA) approach has been chosen. In early stages, CAA solvers have been limited by the computational capacity of the machines, resulting in excessively long simulation time that made them unpopular in research activities. Nowadays, CAA has become more and more relevant, with the ability to solve more complex cases, increasing its usage among institutions and companies.

CAA has been considered the most adequate methodology for the current study. Compared to performing experiments, the CAA approach has several advantages. These include: absence of background noise; being able to obtain more detailed results by increasing the computational time; placing microphones in the flow region without perturbing it. Furthermore, with experiments it is arduous to measure all the flow field details, as the tip vortex interactions. Semi-empirical models, as the Brooks-Pope-Marcolini (BPM) model [8], are not suitable for the present case. This is due

both to the unavailability of empirical data and to the difficulty in adapting the flow properties in the present situation to the analytical model because of the complicated flow features.

Since no CAD files are available for the turbine, the required geometry is created from scratch with SolidWorks based on the previous work from NLR [44] [45] and Van Dorst [61]. The geometry is designed with the CAE software SolidWorks. This DonQi Windmill is investigated for the availability of experimental and analytic data which are employed as benchmark.

About the solution of the flow and acoustic field, the computational software Exa PowerFLOW, which employs Lattice-Boltzmann Methods (LBM), is preferred to Ansys Fluent and other Navier-Stokes solvers. The LBM is chosen for its computational efficiency and for its effectiveness in tackling unsteady problems thanks to its intrinsic low dissipation and dispersion properties [9] [41]. The application of PowerFLOW to unsteady problems represents an emerging practice, with successful employment in aircraft aeroacoustics, both at component level and for the full aircraft [11]. The acoustic data are then obtained by means of the Ffowcs Williams - Hawkins (FW-H) analogy, which calculates noise through the sound propagation from an integration surface where the noise sources are assumed to be located. The analogy is used in order to reduce the high amount of computational time that a direct resolution of the acoustic pressure field would require.

Following the research goals, three significant cases are created and compared:

- the first is the baseline case, which employs the turbine embedded within a diffuser (ducted) and 0° yaw angle;
- the second case features the same turbine, but without diffuser (unducted or bare), keeping the same yaw angle of 0° ;
- the last case uses the ducted turbine as the baseline case, in yawed inflow conditions with a 7.5° angle between wind direction and rotor axis.

1.4. Thesis outline

After the end of the introduction, the present research is composed of the following chapters.

- In Chapter 2, the basic concepts of aeroacoustics, important for the correct understanding of the research, are introduced.
- Chapter 3 explains briefly the history of how the DAWT design was developed and its working principles.
- Chapter 4 shortly introduces the methodology used for the present study: the flow solver and the acoustic solver are presented, as well as basics of Lattice-Boltzmann Methods and FW-H analogy.
- In Chapter 5, the setup created in PowerFLOW to perform the computation is described. This includes the geometry, the lattice, the simulation settings and the acoustic settings.
- Chapter 6 presents the validation of the current methodology and setup, through a comparison with previous analytical, computational and experimental data.
- The flow description is presented in Chapter 7. This comprises instantaneous field, average field, thrust and power produced by the rotor.
- Chapter 8 deals with the acoustic analysis of the turbine.
- Finally, Chapter 9 concludes the report, with a summary of the findings and recommendations for future work.

2

Basic concepts of aeroacoustics

The present Chapter introduces the fundamental concepts of acoustics and aeroacoustics, which are necessary for the correct understanding of this study. The first part focuses on the basics of acoustics, including the definition of sound, the description of the physical properties commonly employed for sound measurement and the interpretation of a sound spectrum. Then, the features of sound generation and propagation are briefly introduced by means of the wave equations and of the analogies developed by Lighthill and Ffwoes-Williams and Hawkings. In the third section, the sound generation mechanisms in a wind turbine are shortly discussed. Finally, the concept of duct mode and its utility is introduced.

2.1. Acoustics basics

2.1.1. What is sound

Before the start of an acoustic analysis, it is worth defining what sound is.

Sound can be defined as a pressure perturbation, which propagates as a longitudinal wave with a finite speed and which can be detected by human ear.

Such pressure perturbation can be caused by many sources, which will be explained in Section 2.2.2. Typical examples can be the vibration of a guitar chord and of our vocal chords, the oscillation of a rope or the periodic movement of a siren.

The sound then propagates as a wave in a medium. The sound wave is defined as a longitudinal wave since the particles of the medium are displaced in the same direction of the wave propagation direction, as can be seen in Figure 2.1. This is a significant difference compared to transverse waves, which displace the medium in the plane perpendicular to the wave propagation direction. Examples of transverse waves are sea waves and light.

The sound propagates with the finite speed c , commonly defined as the speed of sound. The value of c depends on several parameters, such as the density and temperature of the medium. In water c has a values of 1500 m/s , while in dry air at the standard condition of 20 degrees Celsius it is $c_0 = 344\text{ m/s}$.

Sound is defined only in the wave frequency range detectable by human ear. Such interval includes approximately sound wave frequencies of 20 Hz to 20 kHz. The values above this range are classified as ultrasound, the ones below this range as infrasound.

2.1.2. How to measure sound

Sound involves a wide range of pressure variations. For instance, the threshold of hearing is $2 \cdot 10^{-5}\text{ Pa}$, whereas the threshold of pain amounts to 200 Pa . Since the difference can be of several orders of magnitude, a logarithmic scale is practical and commonly used to measure sound.

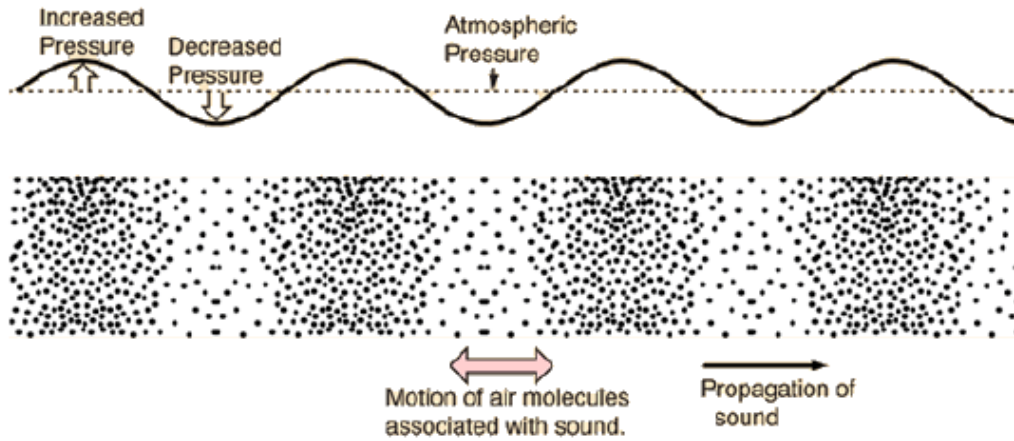


Figure 2.1: Mechanism of sound propagation [47]

Several physical quantities can be used to measure sound: the most popular are the Sound Power Level and the Sound Pressure Level. All of them adopt the decibel scale and are obtained through the logarithm of the ratio of two homogeneous quantities: therefore, they are non-dimensional quantities.

The Sound Pressure Level (SPL) is defined as

$$SPL = 20 \log \left(\frac{p_{rms}}{p_{ref}} \right) \quad (2.1)$$

where p_{rms} is the root mean square of the acoustic pressure, measured in Pascal, and in air $p_{ref} = 2 * 10^{-5} Pa$ the reference pressure value correspondent to the threshold of hearing. Typical Sound Pressure Levels are shown in Table 2.1.

Example noise source	SPL [dB]
Threshold of pain	140
Jackhammer	120
Stereo music	100
Inside a car	90
Office	70
Wind Turbine	50
Inside a bedroom	30
Whispering	20
Threshold of hearing	0

Table 2.1: Everyday life examples of SPL [36]

Due to spherical spreading (see Paragraph 2.2.1), SPL is dependent on the distance between the observer and the source. In order to express the power of the source, the Sound Power Level (PWL) can be adopted.

$$PWL = 10 \log \left(\frac{P_{ac}}{P_{ref}} \right) \tag{2.2}$$

where P_{ac} is the total sound power emitted by the source, defined in Watt as $P_{ac} = \int I dS$ and $P_{ref} = 10^{-12} W$. $I = \frac{p_{rms}^2}{\rho_0 c_0}$ is the acoustic intensity, measured in W/m^2 , with $\rho_0 = 1.225 kg/m^3$ and S the integration surface. Conversely to SPL, the PWL does not depend on the distance from the source, and it is, therefore, an intrinsic property of the source.

2.1.3. Sound spectra

A useful tool for analysing the sound produced by any device is the sound spectra. The sound spectra is a diagram that shows the energy associated to each frequency. It is computed from the time diagram of the pressure variations by using the well known Fourier Transform, as can be seen in Figure 2.2. The Fourier Transform use Fourier series to represent the signal as a sum of cosines and sines. Each cosine or sine forms a mode of a particular frequency, whole contribution to the power spectrum can be computed with the Fast Fourier Transform (FFT) algorithm.

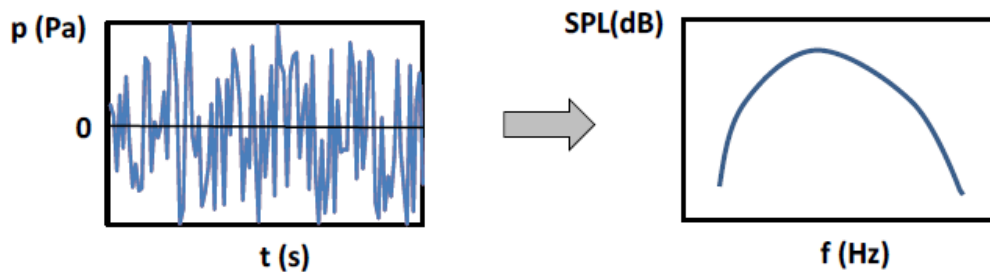


Figure 2.2: Fourier transform: from pressure variations in time (left) to sound spectra in frequency domain (right) [47]

In the sound spectra, different types of frequency bands can be adopted. The two most common are constant frequency bands over the whole domain and proportionally increasing bands, as octaves or third-octaves. Constant bandwidth are mostly used when having fine frequency resolution is needed to detect pure tones and their precise frequency, while octaves are employed especially for noise measurements. According to this choice, both the shape and the sound level shown in the spectra will be different, as can be noticed in Figure 2.3.

The *OverAll Sound Pressure Level* (OASPL) is defined as the total energy contained in the spectrum, integrated over all the resolved frequencies.

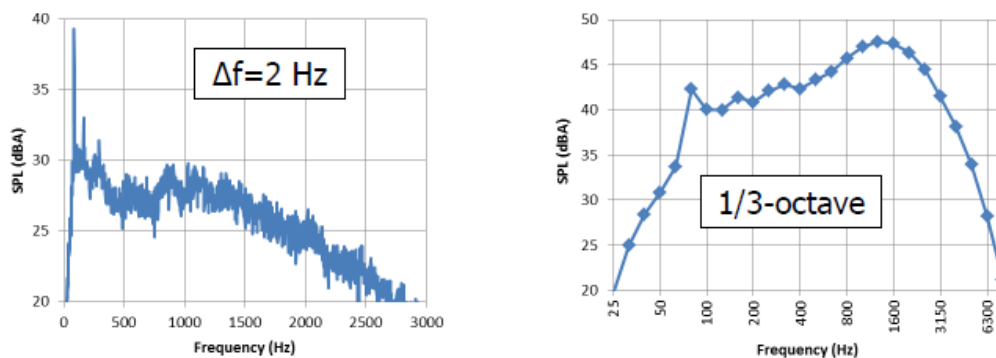


Figure 2.3: Same signal processed with constant bandwidth (left) and one-third octave (right) [47]

It has to be pointed out that human ear is not equally sensitive to all frequencies. For instance, the hearing threshold is higher at low frequencies and lower at frequencies around 3-4 kHz. A quantity which accounts for these differences is the so-called *A-weighted SPL*, whose symbol is dB(A). Noise regulations are usually based on dB(A) and reducing it is a key factor for low-noise design. An example of the same sound spectrum in dB and dB(A) can be seen in Figure 2.4.

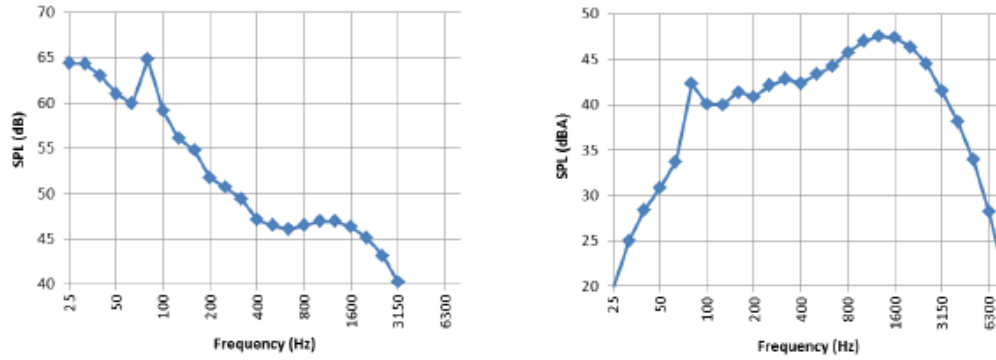


Figure 2.4: Same signal not weighted (left) and weighted with A-level (right) [47]

Finally, from the spectrum it is possible to identify tonal and broadband noise. A *tone* is defined as the sound radiated at a single discrete frequency, as the noise obtained by striking a piano key, while *broadband noise* is characterised by a mixture of different frequencies, as the sound from a waterfall [4]. In the left side of Figure 2.3, there is a tone at approximately 100 Hz, while all the frequency range above 500 Hz is an example of broadband noise.

2.2. Sound propagation and generation

2.2.1. Wave equation for propagation

In order to define the characteristics of sound generation and propagation, the *wave equation* should be derived. The starting point is represented by the basic equations describing the motion of the fluid, namely the conservation of mass and momentum.

The mass conservation is given by

$$\frac{\partial \rho}{\partial t} + \nabla \cdot (\rho \mathbf{v}) = m \quad (2.3)$$

With v the fluid velocity and m the mass source term.

For the momentum conservation, it is valid

$$\frac{\partial(\rho \mathbf{v})}{\partial t} + \nabla \cdot (\mathbf{P} + \rho \mathbf{v} \mathbf{v}) = \mathbf{f} + m \mathbf{v} \quad (2.4)$$

Where \mathbf{f} represents the external forces density, $m \mathbf{v}$ the momentum injection. \mathbf{P} is the fluid stress tensor, related to the pressure and the viscous stress tensor τ through $\mathbf{P} = p\mathbf{I} - \tau$, with \mathbf{I} the unit tensor.

In order to arrive at the wave equation for sound propagation, some assumptions need then to be done. These assumptions are the following.

- Viscous effects, as the term τ , are neglected. For sound propagation, the magnitude of viscous phenomena is significantly lower than inertial phenomena.
- External forces \mathbf{f} are neglected.

- The linear approximation, which neglects second order effects as the term $\rho \mathbf{v}\mathbf{v}$ in Eq. 2.4, is valid. This approximation is clearly valid only when considering small perturbations.
- Isentropic flow is assumed. The assumption is valid since the propagation of the sound wave is much faster than heat transfer.
- The mass and momentum injection terms are considered equal to zero.

The whole derivation of the wave equation can be found in [53]. In the end, the homogeneous wave equation for sound propagation is obtained.

$$\frac{1}{c_0^2} \frac{\partial^2 p}{\partial t^2} - \nabla^2 p = 0 \quad (2.5)$$

2.2.2. Wave equation for sound sources

The basic fluid-dynamics equations, namely the mass and momentum conservation, can be re-arranged in order to derive an inhomogeneous wave equation. This equation needs to describe also the sources of sound, besides the propagation phenomenon.

The same assumptions made to derive the homogeneous equation for sound propagation are done, except:

- The external forces \mathbf{f} are not neglected.
- The mass and momentum injection terms are not null.

The inhomogeneous equation for sound generation can then be derived.

$$\frac{1}{c_0^2} \frac{\partial^2 p}{\partial t^2} - \nabla^2 p = \frac{\partial m}{\partial t} - \nabla * \mathbf{f} \quad (2.6)$$

It is easy to notice that Eq. 2.6 resembles Eq. 2.5, with the addition of two source terms at the right-hand side.

The first noise source is the mass source, the unsteady injection of mass $\frac{\partial m}{\partial t}$. Since this mass source term does not contain any spatial derivative, it can be defined as a *monopole*, which radiates in all the radial directions with the same intensity. Examples of monopole sources can be sirens or the displacement of air due to the rotation of a propeller.

The second term representing a noise source is $\nabla * \mathbf{f}$. It can be noticed that, if force field \mathbf{f} would be constant, for the presence of the divergence operator the term would be null. This means that only a non-uniform force field is able to generate noise. Such a source is defined as *dipole*: it characterised by *directivity*, which means it radiates more efficient in some directions than in others. Dipole sources are for instance the moving forces due to the change of position of the blade.

The sound field created by monopoles and dipoles can be seen in Figure 2.5.

2.2.3. Lighthill analogy

The monopole and the dipole are the two simplest types of sources. However, they do not cover all the phenomena of sound generation by turbulent flow, which cannot be explained either with monopoles or with dipoles. In order to discover other source mechanisms, a more exact solution of the Navier-Stokes equations is required.

James Lighthill used an aero-acoustics analogy to obtain an equation that is formally exact, without approximating the basic fluid-dynamics equations. The equation can be expressed as

$$\frac{1}{c_0^2} \frac{\partial^2 \rho}{\partial t^2} - \frac{\partial^2 \rho}{\partial x_i^2} = \frac{\partial^2 T_{i,j}}{\partial x_i \partial x_j} + \frac{\partial m}{\partial t} - \frac{\partial \mathbf{f}}{\partial x_i} \quad (2.7)$$

The analogy consists in assuming that the observer is surrounded by a stagnant fluid characterised everywhere by uniform sound speed, density and pressure (c_0, ρ_0 and p_0). The propagation part of the equation, at the left-hand side, corresponds therefore to the homogeneous equation for wave propagation, Eq. 2.5, referred to the density. Any difference from the ideal behaviour that characterises the propagation is assumed to be equivalent to a source of sound for the observer. No other assumption is made, including the simplifications explained in 2.2.1. Even though the equation is formally exact, it is meaningful only in the case of a limited noise source region in an uniform stagnant fluid.

It can be noticed that a new source term is present, the Lighthill's stress tensor $T_{i,j}$, which can be written as

$$T_{i,j} = \rho v_i v_j - \tau_{i,j} + (p - c_0^2 \rho) \delta_{i,j} \quad (2.8)$$

where $\delta_{i,j} = 1$ if $i = j$, $\delta_{i,j} = 0$ if $i \neq j$.

Each term represents a deviation from the ideal acoustic behaviour described by Eq. 2.5: such a deviation is equivalent to a different source of sound for the observer. In detail, these deviations are:

- $\rho u_i u_j$ are the non-linear Reynolds stresses, which diverge from the linear approximation of small perturbations;
- $\tau_{i,j}$ are the viscous stresses;
- $(p - c_0^2 \rho)$ is the deviation from homentropic behaviour.

All these sources are present in the term with double space derivative, which makes them quadrupole sources. Free turbulence is indeed an example of quadrupole. The sound field created by a quadrupole can be seen in Figure 2.5.

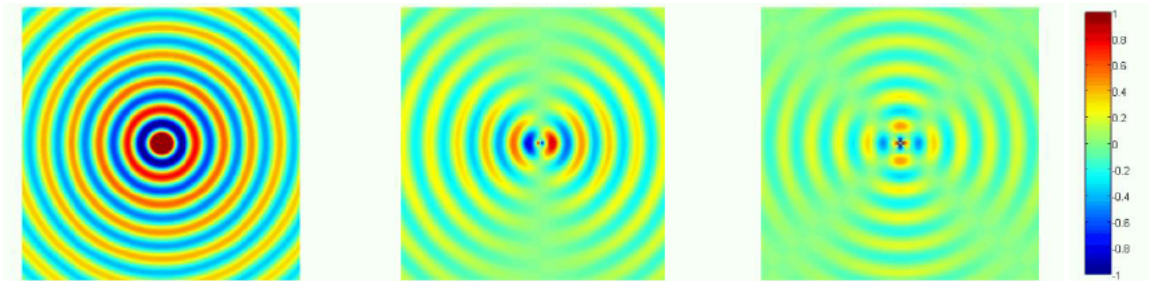


Figure 2.5: Normalised sound field produced by a monopole (left), a dipole (center) and a quadrupole (right) [47]

2.2.4. Ffowcs Williams - Hawkings (FW-H) analogy

An important limitation present in the Lighthill's equation is that it can be applied only on static closed surfaces. Ffowcs Williams and Hawkings derived the FW-H equation, named after their initials, starting from the work of Lighthill, arriving to a formulation that is valid for moving bodies as well [31].

Since there is not a unique way to describe a source starting from the flow field, Ffowcs Williams and Hawkings decided to define the effect of a closed surface $\Sigma(t)$ by choosing to exclude any flow variable inside the volume $\Psi(t)$ enclosed by $\Sigma(t)$. The volume $\Psi(t)$ is then replaced by a quiescent fluid, with the sources distributed on the surface $\Sigma(t)$ [10]. The volume and the surface can move in time.

Defining a function $f(x, t)$ which is positive outside the volume $\Psi(t)$ and negative inside it, the Heaviside function (also known as step function) can be used so that $H(f) = 0$ inside the volume and $H(f) = 1$ outside the volume. By multiplying all the terms of Eq. 2.7 per the Heaviside function $H(f)$, the FW-H equation can be obtained.

$$H(f) \frac{1}{c_0^2} \frac{\partial^2 \rho}{\partial t^2} - H(f) \frac{\partial^2 \rho}{\partial x_i^2} = H(f) \frac{\partial^2 T_{i,j}}{\partial x_i \partial x_j} + H(f) \frac{\partial m}{\partial t} - H(f) \frac{\partial \mathbf{f}}{\partial x_i} \quad (2.9)$$

The original equation was valid only inside the flow, but by using the Heaviside function is trivially satisfied also inside the volume, when all the terms of the equation are null.

The practical implementation of the FW-H equation will be discussed in Section 4.2.

2.2.5. Effect of surfaces

In order to understand the importance of surfaces in the generation of sound in a flow, the Lighthill equation 2.7 can be used again. If the Reynolds stresses are assumed to be dominant in the Lighthill tensor, then $T_{i,j} = \rho u_i u_j$. The assumption is valid for high Reynolds number and for small non-homentropic behaviour.

Then, considering also that no unsteady mass injection nor non-uniform external forces are present, through dimensional analysis it can be obtained that

$$p'^2 \sim M^8 \quad (2.10)$$

So the noise due to free turbulence, where no surface is present, is proportional to the 8th power of the Mach number, defined as $M = \frac{U_\infty}{c}$. When the Mach number is low, the noise produced by free turbulence is then clearly not relevant.

However, the presence of surfaces increases the acoustic efficiency. Two main phenomena can be detected: compact body in a flow and edge scattering.

- *Compact body*

It is characterised by a scale L of the surface lower than the wavelength λ of acoustic waves, $L < \lambda$. The dimensional analysis shows that $p'^2 \sim M^6$, making it a more efficient noise source than free turbulence. A typical example is the noise produced by vortex shedding from a cylinder.

- *Edge scattering*

Conversely to the compact body, the edge scattering has the scale of the surface larger than the sound wavelength, $L > \lambda$. With the usual procedure, it can be shown that $p'^2 \sim M^5$. Trailing edge noise (see Paragraph 2.3.1) is a typical edge scattering noise.

2.2.6. Doppler effect and convective amplification

When a source is moving in a stationary medium, there are two effects which is still useful to mention.

The first is the well-known *Doppler effect*. The Doppler effect causes the approaching noise sources to be heard with higher frequencies from the observer, while sources moving away are heard with lower frequencies.

Physically, this is due to the fact that when a source is moving towards the observer each wave takes slightly less time than the previous one to reach him, 'bunching together' the waves and so increasing the frequency of the sound heard by the observer. The opposite happens when the source is getting further from the observer.

The frequency heard by the observer can be expressed as $f_{obs} = \frac{f_{source}}{1 - M \cos(\theta)}$. The denominator of the fraction is defined as the Doppler factor $D = 1 - M \cos(\theta)$, while θ is the angle between the velocity vector of the source and the observer-source line (see Figure 2.6).

The second is the *convective amplification*. While the Doppler effect influence the frequency of the sound, the convective amplification affects the sound level. When a sound source is approaching, the sound level is increased by a factor equal to the square of the Doppler factor, decreased if the source is moving away.

$$p' \sim \frac{1}{(1 - M \cos(\theta))^2} \quad (2.11)$$

Convective amplification and effect of surfaces can explain the typical patterns of sound in a wind turbine, shown in 2.6. Since the Mach number is low, the predominant noise is the edge noise at the tip of the blade. The convective amplification, together with the trailing edge noise directivity explained in 2.3.1, causes the noise to be heard as higher in the downwards movement of the blade, where it is approaching the microphones.

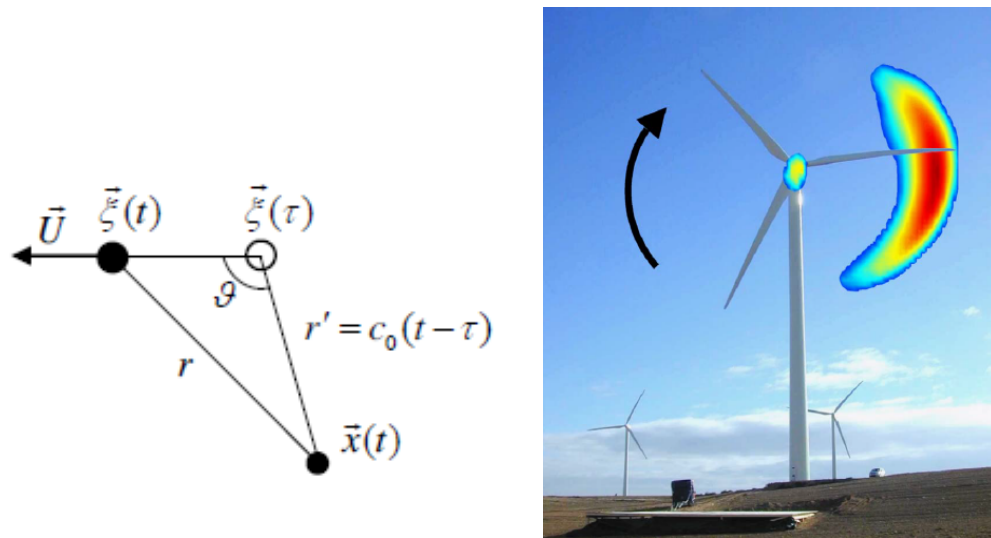


Figure 2.6: Convective amplification sketch (left) [47] and effect on noise patterns of a turbine (right) [48]

2.3. Wind turbine noise

The noise produced by a turbine comes from several different sources. The most common division to cluster them is using two groups: mechanical noise and aerodynamic noise. The mechanical equipment of the turbine, as gearbox, generator, yaw drives, pump, compressor cooling fans and other auxiliary equipment is the responsible for mechanical noise.

In modern wind turbines, mechanical noise is usually negligible compared to the aerodynamic part: therefore, most of the studies, including the present work, focus their analysis only on the aerodynamic group of sound sources. The aerodynamic mechanisms which produce such noise pattern are described in the following paragraph.

2.3.1. Aerodynamic noise sources

Aerodynamic noise can be divided in three groups, according to the sound source type: turbulent inflow noise, low frequency noise and airfoil self-noise [36].

Turbulent inflow noise is related to the turbulent nature of the wind flow. Atmospheric turbulence is mainly due to the flow-surface interaction; the buoyancy generated by the temperature gradient has a minor factor. The interaction between the turbulent inflow and the blades generates a broadband noise [36].

Low frequency noise includes the sounds generated by the periodic change in the wind-speed,

namely caused by the blades passing in front of the tower (in the upwind configuration) and by the wind shear. Low frequency noise is usually not relevant for human's auditory system [36].

Airfoil self-noise consists of several mechanisms.

- Turbulent-Boundary-Layer - Trailing-Edge noise (TBL-TE): at high Reynolds numbers (approximately higher than 10^6), turbulent boundary layer is formed over the blades. The transition to a turbulent boundary layer may be either natural or forced, e.g. with zigzag trips as in the current work (see Paragraph 5.1). The eddies in the boundary layer scatter as they pass the trailing edge, generating noise. Since the structures which are generated are random and chaotic, TBL-TE noise is mainly of broadband nature [8] [48].

TBL-TE noise shows the characteristics of a dipole: a slow-noise zone is therefore created in the chordwise direction. It can be derived, using a semi-infinite flat-plate approximation, that the maximum radiation takes place towards the airfoil leading edge [23]. Furthermore, with the same approximation the TBL-TE noise is proportional to the fifth scale of the local flow velocity and to the boundary layer displacement thickness δ^* [8].

TBL-TE noise is usually the most relevant noise mechanism in modern wind turbines, and explains the often named 'swishing noise' which observers perceive in the proximity of wind blades. The blades produce an approximately constant broadband noise during the revolution. The observers perceive such noise as varying in time with a frequency correspondent to the Blade Passing Frequency (BPF), which is due to convective amplification and trailing edge noise directivity.

- Laminar-Boundary-Layer and Vortex-Shedding noise (LBL-VS): at lower Reynolds ($10^5 - 10^6$), when the flow is still laminar, shedding of vortices from the trailing edge is a common noise source. LBL-VS noise is relevant especially for small wind turbines and the inboard section of large and slow-rotating turbines [36].
- Separation and stall noise: when the angle of attack is not nil, separation of the flow may occur near the trailing edge, leading to turbulent vorticity and consequently noise. For high angles of attack, stall may take place as well [8].
- Tip vortex formation noise: the presence of a rotational turbulent region at the tip is a source of noise as well. Usually, with a proper design of the tip, this noise source is not relevant. However, the accelerated flow in the tip region in DAWT makes the tip vortex noise important for this particular design [36].
- Trailing-Edge-Bluntness Vortex-Shedding (TEB-VS) noise: blunt trailing edge may be a relevant source of noise as well. It is a tonal noise caused by the well-known Karman vortex shedding street. It can be prevented with a proper design and manufacturing of the trailing edge [36].

2.4. Duct modes

In duct acoustics, it is common to use *modes* in order to understand specific characteristics of the power spectrum, as tones of unknown origin. This kind of analysis is generally employed when dealing with turbofans, where the number of vanes in the rotor and in the stator can be regulated in order to limit the noise emission of the device. Since this study deals with a ducted turbine, performing an analysis of duct modes is interesting to get further insights into phenomena that might happen inside the duct.

Duct modes are a group of solutions that can solve the reduced wave equation through a series expansions. These solutions are valid for a duct of constant cross-section: any deviation from this

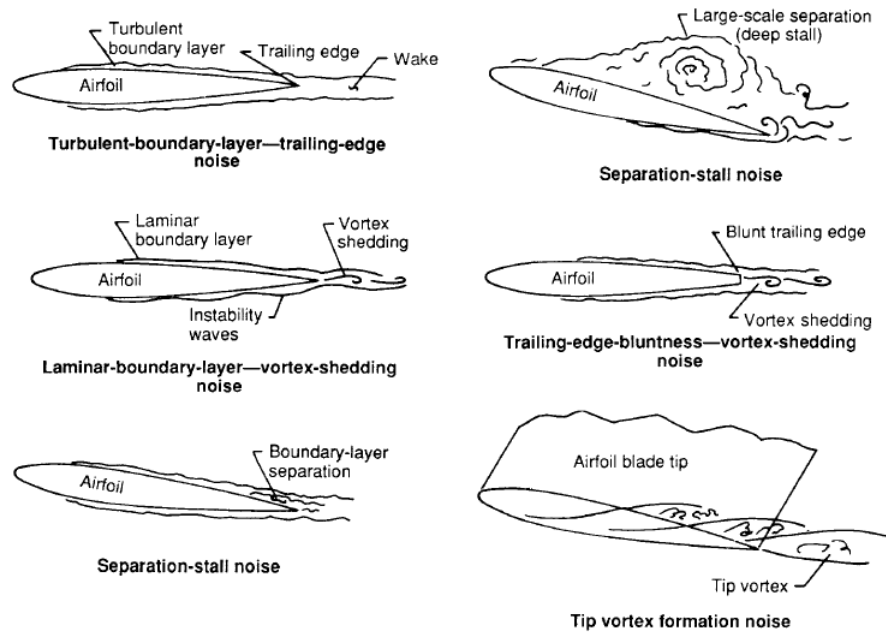


Figure 2.7: Airfoil self-noise mechanisms [8]

condition, as in the current study, may result in a variation from the ideal case. The interest in modes because they feature a simple structure which makes easier to understand the complex behaviour of the field, despite being mathematically correct. The modes are linked to the eigensolutions of the two-dimensional Laplace operator which acts on a cross-section.

In a cylindrical duct, three sets of eigenvalues (or modal wave numbers) can be distinguished: the radial eigenvalue α , the circumferential eigenvalue m and the axial eigenvalue k . A complete set of them determines an associated solution of the reduced wave equation, i.e. a duct mode. There are always just a finite number of modes with real axial eigenvalue k : these modes are named *cut-on* and actually propagate, while the modes with imaginary k are named *cut-off* and are evanescent.

In the case of a rotating fan with B blades and rotating frequency Ω , each harmonic frequency $\omega_h = nB\Omega$, with $n \in \mathbb{N}$, is connected to a circumferential eigenvalue $m = nB$. The *plane wave*, i.e. the wave with $m = 0$, is generated with frequency $\omega_h = 0$ and therefore not of interest in an ideal case. An important finding about rotating fans is that in an ideal duct for producing sound the frequency $f_m = \frac{m\Omega}{2\pi}$ has to be higher than the correspondent cut-off frequency, which happens only when the tip is rotating supersonically. In reality, the ingested turbulence and the wake shed by the blades are characterised by different frequencies and do not follow this mechanism, but the result is of great importance for noise due to blade thickness and lift forces.

It is not in the purpose of this research to go in depth in the duct modes mathematical formulation, which for the interested reader can be found in the book by Rienstra [53], so just the most important principles were mentioned here.

3

Diffuser Augmented Wind Turbines

In this Chapter, an overview of the literature on Diffuser Augmented Wind Turbine is given. The first section presents a short history of the research on ducted turbines, from the 1950s to current days, including analytic models, computations and experimental results. Such suction does not intend to constitute a complete review of the DAWT concept, but it should instead be considered as a simple description of the most important results with respect to the current study. The second section deals with the working principles of power augmentation in a DAWT and with the definitions of few important properties.

3.1. History and literature

3.1.1. History

The first one that speculated the potential of a using a diffuser to enhance the power of a wind turbine was Betz [62] in 1929.

The experiments and the theories by Sanuki [55] in 1950 and by Iwasaki [34] in 1953 showed clearly that an increase of the power coefficient compared to a bare turbine was achievable.

In the 1950's, many researchers tried to evaluate the potential of a diffuser augmented wind turbine. In Europe, a paper published by Lilley and Rainbird [51] in 1956 explained that a power augmentation would be due to an increase of the axial velocity and to a reduction of blade tip losses. They also suggested the use of a flap at the end of the diffuser to decrease the exit pressure to produce a suction effect across the rotor. One of the designs proposed by Lilley and Rainbird can be seen in Figure 3.1.

After these early researchers, no relevant activities are traced until the 1970s, when the Gruman became interested in DAWTs the US after the oil crisis. Foreman and al. [27] performed an extensive research, testing more than 100 designs in the wind tunnel and including economic analysis to their work. They concluded that, even if some uncertainties were present, many designs could increase the power extraction by a factor of around 2, and that at least two models should have been economically effective. Some of the designs presented a slot to re-energise the boundary layer of the diffuser, as shown in Fig. 3.1. They however later found out that the vortexes shed from the rotor have already a similar energising effect [25].

Since 1979, several analytic models started were developed and several experiments were performed. Computational analyses were also carried out from the early 2000s. The most important analytic, computational and experimental results are presented in paragraphs 3.1.3, 3.1.4 and 3.1.5.

The first company to put the DAWT concept in a commercial product was Vortec in New Zealand in 1997. The project showed much lower power output than expected and Vortec quitted its activity [58]. Other small companies in Europe, as CITA, KBE, Enflo, CATT [58] and DonQi (see Paragraph

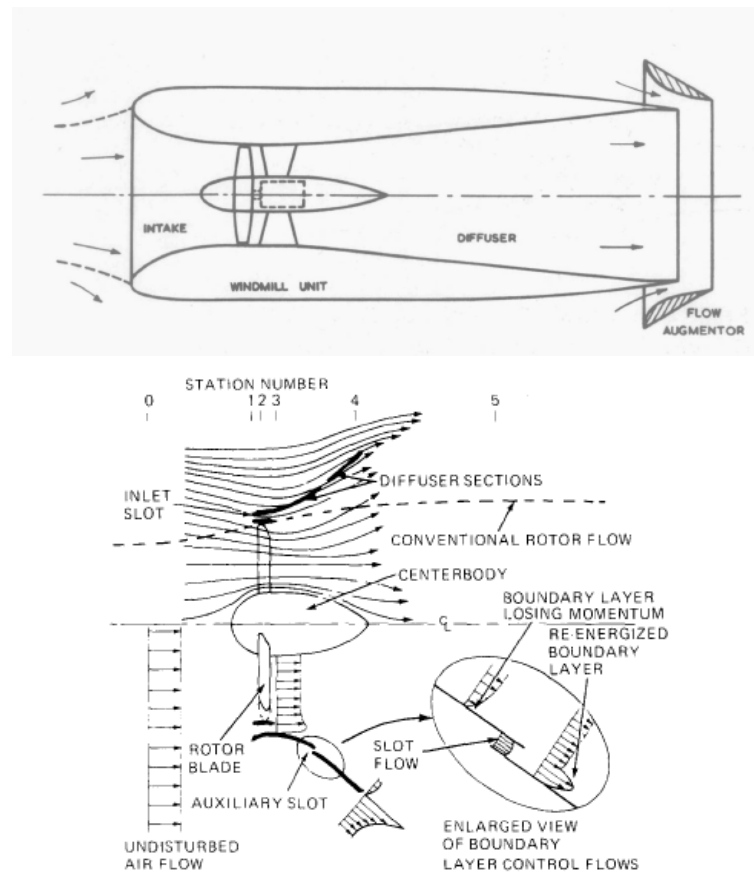


Figure 3.1: Layouts of DAWT designs by Lilley and Rainbird [51] (top) and Foremann [25] (bottom)

3.1.2), tried to produce ducted turbine but without encountering any significant commercial success. At the moment, to the knowledge's author, no relevant commercial success has been achieved so far.

In the last 15 years, a particular concept of diffuser augmented wind turbine has been developed in Japan, the so-called 'Wind Lens' [1] [49] [56]. The Wind Lens has the peculiarity of having a thin and curved shroud, with no airfoil-shaped annular section, with a large flange at its end to exploit the pressure reduction effect and with downwind configuration. Intensive research has been carried out in the last years, primarily through the means of experiments and computations. The design is considered apt for the urban environment but also for offshore application, which brought to realise tests in the bay of Hakata. The research has brought useful insights on fluid-dynamic phenomena, as the effect of the shroud on tip vortexes as explained in Section 3.2. Some points remain however not cleared, as the effect of the shroud on the noise produced by the device.

3.1.2. DonQi Urban Windmill

DonQi Quandary Innovations, later named DonQi Independent Energy (and sometimes referred in this text simply as DonQi), was a small company active in the Netherlands from 2007 until 2012. The goal of DonQi was to become a player in the production of sustainable and decentralised energy. Its product DonQi Urban Windmill consists in a Diffuser Augmented Wind Turbine particularly apt for the built environment, with small size (the rotor diameter is 1.5 m) and small power output (the nominal power is 1.75 kW). Its original design has been first optimised in collaboration with the Netherlands Aerospace Center (NLR) [44] [45], by means of numerical analyses, and with Delft University of Technology [58] [61].

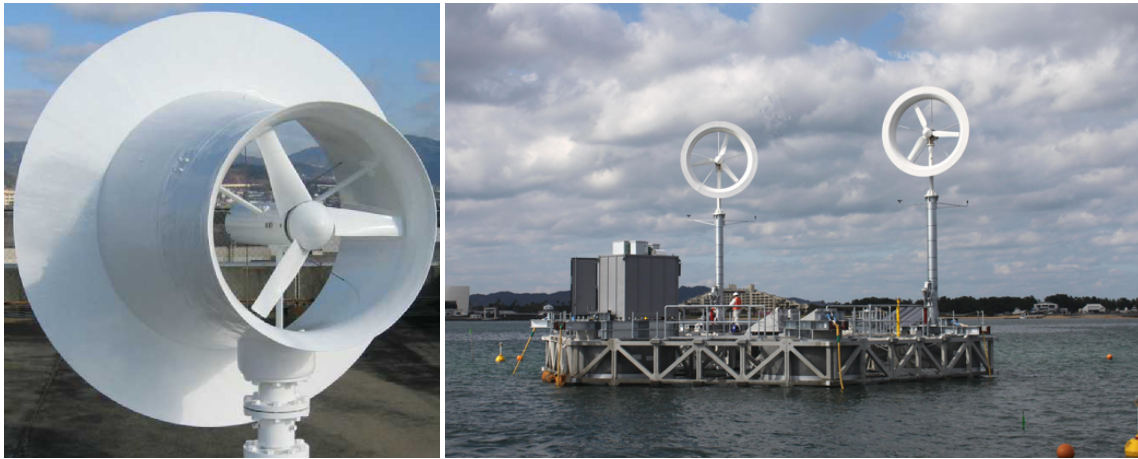


Figure 3.2: Pictures of operating Wind-Lenses [52]

The TU Delft MSc student Van Dorst [61] proposed two improved designs of the blades. Despite the 'optimal blade' has the highest power output, the 'linearised blade' was indicated as the best possible improvement. Indeed, the latter better suited production and market needs and it yielded significantly higher power output than the correspondent bare wind turbine.

The properties of the optimised blades were obtained by finding the best chord and thickness distribution through a Blade Element Momentum (BEM) model with wake rotation. The BEM model on its turn takes as basis the velocity distribution, which is calculated with an axisymmetric surface vorticity model where the rotor is simplified as a vortex cylinder and a root vortex.

However, Van Dorst did not optimise many crucial parameters of the turbine, as the rotor length, the airfoil, the tip clearance and the shape of the diffuser. To the author's knowledge, no further improvements to the DonQi Urban Windmill have been proposed in the following years.

Pictures of the DonQi Urban Windmill and of the design with 'linearised blades' can be found in Figure 3.3.



Figure 3.3: DonQi Windmill operating on a rooftop (left) and DonQi with linearised blades in TU Delft Open Jet Facilities (right)

3.1.3. Analytic approaches

De Vries [17] was one of the first to develop a consistent analytic approach, separating the effect of a simple straight diffuser, with flat plate as annular section, and of a 'shroud', with an airfoil as annular section of the duct. The approach is based on a one-dimensional analysis (as in derivation of Betz) with the pressure recovery as key parameter. He found out an optimum power coefficient of 0.7698 for the simple diffuser, whereas he did not have a final statement on the shrouded case due to the many interconnected parameters involved in the theory.

Hansen [30] derived a simple momentum theory, assuming no wake mixing process, and showed that the Betz limit can be exceeded up to a value of approximately 0.94.

Van Bussel [59] also developed a momentum theory for an empty diffuser and a DAWT, showing that the results are valid for any location of the rotor inside the diffuser. The main conclusions obtained are: the optimal pressure drop over the rotor is always equal to $\frac{8}{9}$ as in bare turbines; the maximum amount of energy which can be extracted per unit of volume is the same for the ducted and unducted case; power augmentation factors of 2.5 might be achievable with significant backpressure.

Other significant models were developed by Jamieson [35] and Werle and Pretz [63]. Jamieson extends the actuator disc model and the BEM theory to systems with additional solid tools as ducts or diffusers. Werle and Pretz proposed a momentum theory that models the effect of the diffuser as an axial force on the fluid through a duct thrust coefficient that determines the maximum power achievable in the device. Both the papers agreed on the optimal thrust coefficient (i.e. the relative pressure drop) of $\frac{8}{9}$ as found by Van Bussel.

Different optimal thrust coefficient values were later found [38] [6] [16]. Khamlaj and Rumpfkeil [37] evaluate that false assumptions presents in the models by Van Bussel, Jamieson and Werle and Pretz make the models valid only for short diffusers or entirely invalid. They showed that the theory by Van Bussel [59] is only valid for short diffusers, since it assumes the same conditions, in terms of induction factor, at the end of the diffuser than on the rotor disk in a bare turbine.

Finally, two recent models are worth mentioning. The model of Oliveira et al. [16] solves without assumptions the flow field to describe the interactions between axi-symmetric bodies and actuators in inviscid flow. They describe the flow through two coefficients, relative to the forces exerted on the flow by the rotor and to the resultant of the pressure forces on the flow crossing the rotor: these two coefficients are not linearly related. One of the main findings is that the optimum power coefficient, around 0.8, is found for thrust coefficients higher than $\frac{8}{9}$. The second model is the semi-analytical model by Bontempo and Manna [6]. It uses the non-linear actuator disk theory extended to ducted rotors, finding the exact solution of the inviscid axisymmetric flow by a heavily loaded rotor. Even though the approach starts from a different background compared to the previous ones, it agrees on the power augmentation achievable by DAWTs and it shows that the power output increased with the diffuser thrust.

Finally, it should be pointed out that the power augmentation factors and the power coefficient reported here as found in the literature refer to the rotor area rather than to the diffuser area. The effects of such a choice are later discussed in 3.2.2.

3.1.4. Computational results

Hansen [30] used a CFD approach to verify his momentum theory, modelling the rotor as volume forces on the grid. The approach confirmed the results obtained in the theory.

Takahashi et al. [56] performed unsteady 3D Large Eddy Simulation (LES) on the Wind-Lens to explain the aerodynamic vortices behaviour in the turbine, comparing it with an unaugmented turbine. They show that strong tip vortices are generated, but they do not preserve their magnitude after the end of the diffuser. Counter-rotating vortexes are created by the rotation of the blade next to the diffuser and these two groups of vortices weaken each other while going downstream in the

diffuser, as shown in Fig. 3.4. In the Figure, vortices are computed through the lambda-2 method and coloured according to the tangential vorticity.

Compared to the bare turbine, the ducted model presented stronger tip vortices at the rotor plane, but weaker vortices at the location correspondent to the diffuser exit. They claim that this effect would cause lower noise emissions for the ducted case: however, no noise computations is done to support this hypothesis.

They also perform the same analysis on an another Wind-Lens design, characterised by a shorter diffuser. In such case, the diffuser is not long enough to make the vortices disappear at the exit section.

Dighe et al. [19] used a computational approach by solving Reynolds-Averaged-Navier-Stokes (RANS) equations within and around the DonQi Windmill. The rotor was modelled as an actuator disk, with two body forces to simulate the pressure jump. The methodology showed a good agreement with the experimental data from Tang et al. [57], with some limitations in the area just downstream of the actuator disk location.

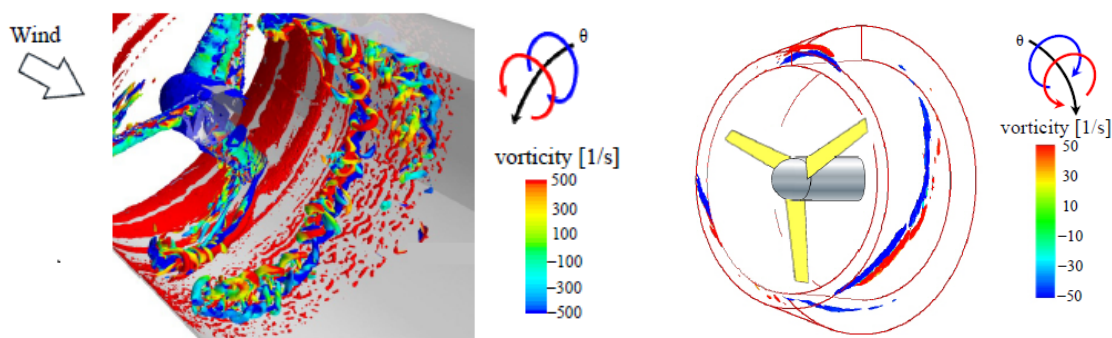


Figure 3.4: Vortices behaviour in LES simulation (left) and in a wind tunnel experiment (right) on a Wind-Lens turbine [56]

Hashem et al. [31] performed an acoustic study on Wind-Lens by using Unsteady RANS (URANS) equations and FW-H analogy for far-field noise. Contrary to what found from Takahashi et al., they found the ducted Wind-Lens to be noisier than its unducted counterpart for a variety of diffuser lengths and tip-speed-ratios (TSR). Unfortunately, they do not attempt to describe neither the noise directivity nor to describe the noise sources in the turbine.

3.1.5. Experimental results

Few experiments were carried out to test the performance of DAWTs in yawed conditions. Igra [33] employed two DAWT designs, named Model B and Model C, shown in Fig. 3.5. These models featured a ring-shaped flap at the end of a diffuser and a screen to simulate the rotor disk. What was found was that the power output of the turbine remained constant for yaw angles up to 25° for the model B and 30° for the model C. Igra ascribed this behaviour to the lift produced by the diffuser, which would increase with the yaw angle decreasing the pressure inside the device.

Phillips [50] performed similar experiments with a multi-slotted turbine, finding that the performance of the device was constant for yaw angles until 15° . The reason behind this response was described as the effect of the slot, which would add momentum to the boundary layer and thus preventing the stall inside the diffuser.

Experiments were performed on the DonQi Windmill by ten Hoopen [58] to check whether vortex generators could improve the power output of the turbine. Their application was found to be less effective in power output than by adding a Gurney flap.

Tang et al. [57] used the DonQi diffuser, with a porous disk to simulate the rotor. By regulating the disk porosity, a different axial force is exerted on the flow. Such axial force on the disk is found

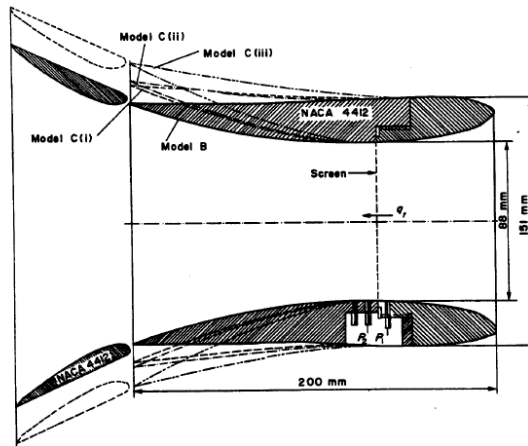


Figure 3.5: Schematic of the DAWT design by Igra [33]

to influence largely the axial loading on the diffuser, bringing to flow separation on the diffuser outer face with the highest axial force simulated, equal to a thrust coefficient of 0.89. Furthermore, contrary to the 1-D theory from Van Bussel [59], the thrust of the rotor was found to be higher when the disk was surrounded with the diffuser than when no diffuser was present.

3.2. DAWT theory

3.2.1. Working principles

In order to explain the power augmentation which can be realised with the diffuser, from 1-D momentum theory the power extracted by a turbine can be expressed as $P = T \frac{m}{A_r \rho}$. T represents the rotor thrust, m the mass flow across the rotor, A_r the rotor swept area and ρ the air density. In order to increase the power output, the pressure jump across the rotor $\Delta p = \frac{T}{A_r}$ should be enhanced, but this in turn lowers the mass flow. Betz [62] derived that the condition for optimal power recovery is a mass flow across the rotor which is 2/3 of the undisturbed mass flow.

Adding a diffuser around the turbine allows increasing the mass flow without lowering the pressure jump. A common diffuser employed in a DAWT is an annular device whose cross-section is an airfoil with suction side pointing towards the center, as can be seen in Fig. 3.6. As known from basic aerodynamic theory, such a profile generates a circulation Γ which results in an axial force directed towards the center of the device. Such force accelerates the flow inside the diffuser, increasing the mass flow. Also, an higher mass flow increases the thrust produced by the rotor, hence the diffuser increases both the T and the m terms in $P = T \frac{m}{A_r \rho}$.

A flat plate can be used as diffuser cross-section to generate such axial force as well, as shown in Fig. 3.7. However, its shape makes the diffuser subject to the phenomenon of stall, it does not permit design variations and it presents structural issues compared to an airfoil shape.

Another way to increase the mass flow is to place a small Gurney-flap at the end of the duct. This increases the pressure on the diffuser pressure side and decreases the pressure on the suction side. This results in an increased axial force exerted towards the device center, which in turn increases the mass flow inside the diffuser [49]. This is widely used in the Wind-Lens, a particular DAWT concept (described in next paragraph), where a long flange is adopted, as shown in Figure 3.8.

3.2.2. Useful properties

The rotor thrust T is defined as the force in the direction of the rotor axis.

The rotor torque Q is described as the moment around the rotor axis, i.e. the tangential force multiplied by the distance from the axis, with the positive value given by the right-hand rule.

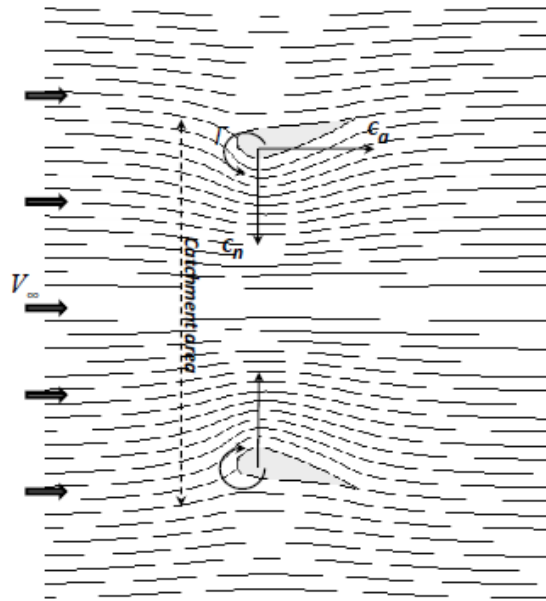


Figure 3.6: Ideal flow pattern in the cross-section of a diffuser [58]

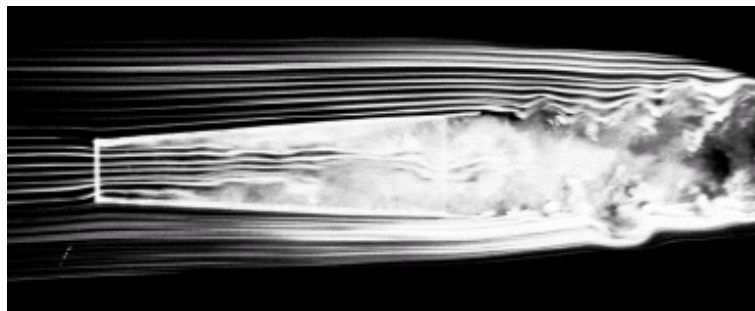


Figure 3.7: Flow around a diffuser visualised with smoke streamlines [49]

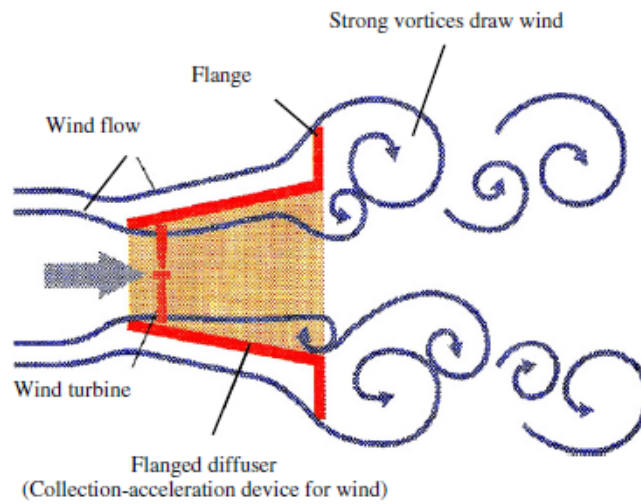


Figure 3.8: Effect of flange on the fluid-dynamic behaviour of a DAWT [49]

The power is computed by multiplying the torque per the rotational speed of the turbine, $P = Q\Omega$. This is an alternative definition to the one presented in Paragraph 3.2.1, derived from the Blade Element theory.

The thrust coefficient is a dimensionless measure of the thrust, which can be written as

$$C_T = \frac{T}{0.5\rho U_\infty^2 A_r} \quad (3.1)$$

with T thrust produced by rotor, ρ is the standard air density, U_∞ the free stream wind speed and A_r the rotor swept area.

A local thrust coefficient is employed to describe the axial load along the span of a blade.

It is expressed as

$$C_t = \frac{T}{0.5\rho U_\infty^2 \pi(\Delta r)^2}, \quad (3.2)$$

with Δr length of a blade element in the radial direction.

For what concerns the power coefficient, the analogous measure for the power, the two formulas

$$C_{Pr} = \frac{P}{0.5\rho U_\infty^3 A_r} \quad (3.3)$$

and

$$C_{P,diff} = \frac{P}{0.5\rho U_\infty^3 A_{diff}} \quad (3.4)$$

can be used, referring to the rotor swept area or to the diffuser exit area A_{diff} .

In the literature, many researchers have shown how the diffuser augmented wind turbine can exceed the Betz limit of $C_p = 16/27 = 0.593$. This argument was always sustained by referring to the power coefficient as $C_p = \frac{P}{0.5\rho U_\infty^3 A_r}$, using the rotor area make the power non-dimensional. By using this definition of C_p , the power output of a diffuser augmented turbine compared to an analogous bare one can be of several units.

However, since the diffuser is an active component in the turbine, it seems more appropriate to use the diffuser area A_{diff} for the definition of power coefficient. Indeed, Van Bussel [59] concluded with a simple momentum theory that the amount of power output per volume, so using the respective area, which can be achieved with a DAWT is the same than a bare turbine. Lubitz and Shomer [39] have shown that, even though DAWTs have never been really optimised, in the literature there is no proof of a device exceeding the Betz limit of $C_p = 16/27$ when referring to the diffuser area.

The pressure coefficient is a significant parameter to define the flow field around an airfoil. It is defined as

$$C_p = \frac{p - p_\infty}{0.5\rho U_\infty^2} = \frac{p - p_\infty}{p_0 - p_\infty} \quad (3.5)$$

with p static pressure in the specific point and p_0 stagnation pressure in the freestream. A C_p of one indicates a stagnation point, while a C_p of zero indicates a point with same static pressure than the undisturbed flow.

3.2.3. Performance of yawed turbine

Cresswell et al. [15] summarised the performance of DAWTs in the yaw. As could be grasped from the experiments described in Paragraph 3.1.5, there is agreement that the machine can preserve its working conditions (including the power output) with low yaw angle. However, the exact range of angles and the producing mechanisms are not clear. They also observed that the maximum angle at which the turbine can output the same power (maximum unaffected angle) depends on the

ratio between the length and the outlet diameter of the diffuser, $\frac{L}{2R_{out}}$. With increasing $\frac{L}{2R_{out}}$, the maximum unaffected yaw angle increases.

An overview of the performance of existing DAWTs in yaw can be seen in Figure 3.9, where a linear relationship between $\frac{L}{2R_{out}}$ and the maximum unaffected yaw angle is suggested.

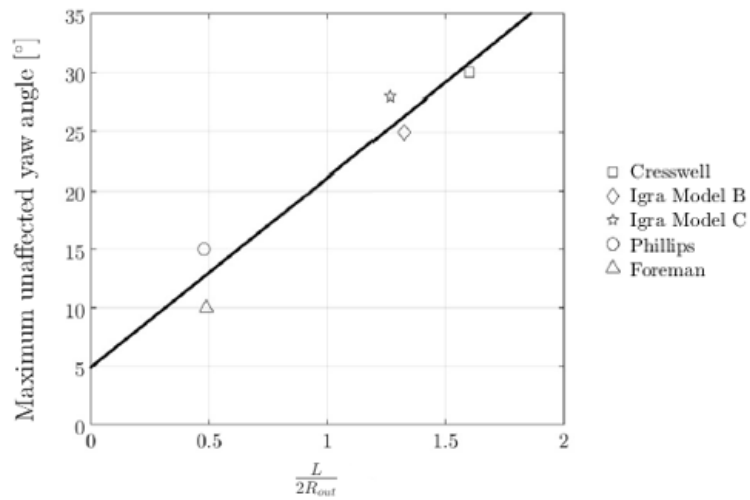


Figure 3.9: Maximum unaffected yaw angle for different DAWT designs, including the devices by Igra [33], Foreman and Gilbert [26] and Phillips [50]. Adapted from Cresswell [15].

4

Methodology

In this Chapter, the methodology employed in the current study is presented. In the first part, the flow solver Exa PowerFLOW is introduced. Since the flow field is obtained through Lattice-Boltzmann Methods, the fundamental principles of such methods are described, including computational algorithm, boundary conditions implementations and turbulence modelling. In the second part, the acoustic solver is presented, including the implementation of the FW-H analogy and the sampling criteria.

4.1. Flow solver

The computations presented in this paper have been carried out with the CFD software Exa PowerFLOW 5.4a, which employs the Lattice-Boltzmann-Methods (LBM) to compute the unsteady flow field. This method emerged in the last two decades as an alternative to the Navier-Stokes equations solvers. The LBM is particularly suitable for the current study, especially for its effectiveness in tackling unsteady problems thanks to the intrinsic low dissipation and dispersion properties.

The first part of the Chapter deals with the basic concepts behind LBM, including physical background, computational loop and modelling of boundary conditions and turbulence. In the second part, a short comparison with Navier-Stokes methods is carried out to highlight the advantages and the disadvantages of LBM.

4.1.1. Basics of Lattice-Boltzmann Methods

Basic principles

The Lattice-Boltzmann-Method developed starting from the Lattice Gas Automata, a discrete particle kinetics solver. However, it can also be seen as a finite difference solver of the Boltzmann equation [13], which makes easier to understand its physical background.

The kinetic theory of Boltzmann describes a fluid as a composition of particles moving with random motions and exchanging momentum and energy through the processes of streaming and collision of the particles [5]. The LBM can indeed be considered a discretised approach to Boltzmann theory, restricting the particles as nodes of a lattice. With quadratic mesh, each particle has only 9 possible directions, including resting, in 2 dimensions: this is defined as D2Q9 model. In the three-dimensional case, the most popular analogous model is the D3Q19 model, with 19 possible directions. Figure 4.1 shows the two cases.

Boltzmann transport equation can be written as

$$\frac{\partial f}{\partial t} + \mathbf{u} * \nabla f = \Omega \quad (4.1)$$

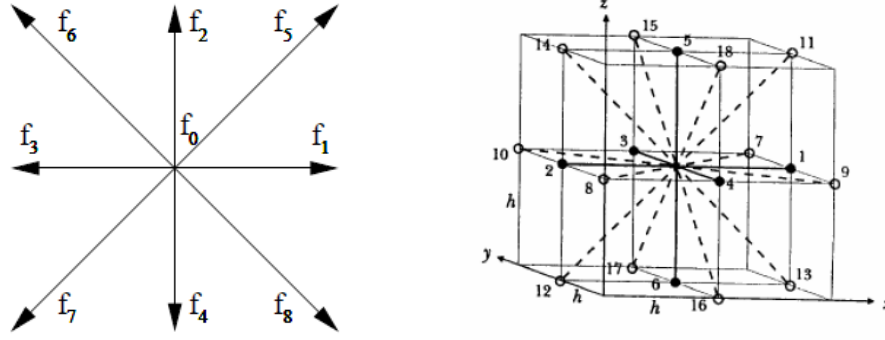


Figure 4.1: Lattice node in D2Q9 model (left) and in D3Q19 model (right) [32]

where $f = f(\mathbf{x}, t)$ is the particle distribution function, with \mathbf{x} the position of the particle, \mathbf{u} the flow velocity and Ω the collision operator.

The equation can be written after the LBM discretisation as

$$f_i(\mathbf{x} + c\mathbf{e}_i\Delta t, t + \Delta t) - f_i(\mathbf{x}, t) = \frac{f_i(\mathbf{x}, t) - f_i^{eq}(\mathbf{x}, t)}{\tau} \quad (4.2)$$

where the left-hand side represents the process of streaming, the right-hand side the process of collision [5]. τ is the relaxation time before reaching the equilibrium, \mathbf{e}_i the discrete microscopic velocity and c the lattice speed. i denotes each possible direction of the particle, ranging from 1 to 19 for the three-dimensional case. $c\mathbf{e}_i\Delta t$ is the space increment, whereas Δt the time increment. Finally, f_i^{eq} is the equilibrium distribution.

For single phase flows, f_i^{eq} can be described through the Bhatnagar-Gross-Krook (BGK) collision model as

$$f_i^{eq}(\mathbf{x}, t) = w_i\rho\left[1 + 3\frac{\mathbf{e}_i * \mathbf{u}}{c} + \frac{9}{2}\frac{(\mathbf{e}_i * \mathbf{u})^2}{c^2} - \frac{3}{2}\frac{\mathbf{u} * \mathbf{u}}{c^2}\right] \quad (4.3)$$

where w_i are the weights: in the 2D case, they are $\frac{4}{9}$ for $i=0$ (rest particles), $\frac{1}{9}$ for $i=1,2,3,4$, $\frac{1}{36}$ for $i=5,6,7,8$ [3], where the indexes represent the direction as shown in Figure 4.1.

Through the microscopic quantities, it is possible to retrieve macroscopic properties [5]. The macroscopic fluid density can be defined in the 2D case as

$$\rho(\mathbf{x}, t) = \sum_{i=0}^8 f_i(\mathbf{x}, t) \quad (4.4)$$

and the macroscopic velocity as

$$\mathbf{u}(\mathbf{x}, t) = \frac{1}{\rho} \sum_{i=0}^8 c f_i \mathbf{e}_i \quad (4.5)$$

Computational algorithm

The computational algorithm used to compute fluid characteristics can be summarized as follows [29] [32] [5].

- Step a in Figure 4.2 is the initial condition. In case the time step is the first one, ρ , \mathbf{u} , f_i and f_i^{eq} need to be initialised. Otherwise, the values from the previous time step are used. The length of the arrow represents the distribution function, i.e. the probability for a particle to move in the direction of the arrow.

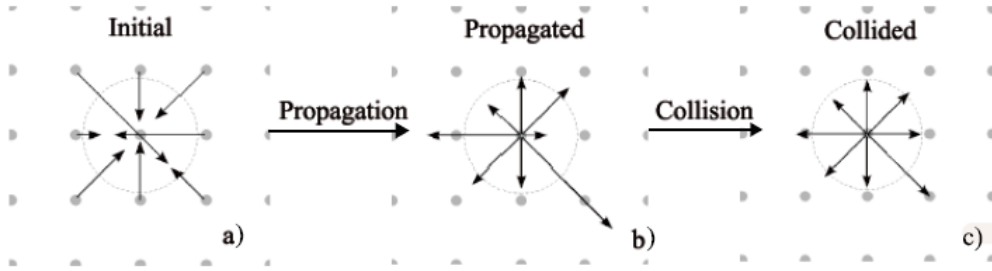


Figure 4.2: Steps in the computational loop of LBM [32]

- In step b in Figure 4.2, the propagation step has happened. Eq. 4.2, can be re-written as

$$f'_i(\mathbf{x} + c\mathbf{e}_i\Delta t, t + \Delta t) = f_i(\mathbf{x}, t) \quad (4.6)$$

with the new value of f'_i at the left-hand side to be calculated using all the term $f_i(\mathbf{x}, t)$ in the right-hand side that contains all the values from the previous time-step. Using the new value of f'_i , the macroscopic velocity and density can be obtained with Eq. 4.4 and Eq.4.5.

- Step c represents the system after the collision process. Eq. 4.3 allows calculating the new equilibrium distribution. Referring again to Eq. 4.2, the new distribution function can be obtained with

$$f_i = f'_i - \frac{1}{\tau}(f'_i - f_i^{eq}) \quad (4.7)$$

where all the variables are function of $(\mathbf{x} + c\mathbf{e}_i\Delta t, t + \Delta t)$. The new f_i can then be used starting again from step 1.

Boundary conditions

The implementation of Boundary Conditions (BCs) is crucial in any numerical analysis. They have to ensure stability and accuracy of the computations and to reflect the property of the fluid. In Lattice-Boltzmann Methods, the two most widely used boundary conditions are the *Bounce-Back BC* and the *Zou-He velocity and pressure BC* [5].

The Bounce-Back condition is commonly used to obtain no-slip conditions on the walls. The basic principle of Bounce-Back BC is that when the particle distribution propagates to a wall node, it bounces back to the node where it came from, as it is shown in Figure 4.3 [13]. In this way, the velocity is set to zero at the wall, ensuring the no-slip condition. The main advantage of this method is the smooth implementation: the BC does not depend on the geometry of the boundary (which is assumed to have the same direction of the lattice). This allows analysing quickly complex geometries. On the other hand, it was shown [28] that this method has only first-order of accuracy, degrading LBM numerical precision. A possible improvement is the *mid-grid Bounce-Back BC*, which uses fictitious nodes and places the boundary between them and the real nodes of the fluid, ensuring a second order accuracy [5].

The Zou-He BC starts from a different point, imposing a velocity or pressure value on the boundary. Some of the particle distributions are then known after streaming, while the others are computed through a linear system. This BC depends on the geometry of the boundary but allows modelling flows with prescribed velocity, pressure and density at the boundaries [64].

In Exa PowerFLOW, in high Reynolds simulations a turbulent wall model, built starting from the well-known law of the wall, is used to model the surface boundary condition. Such model employs

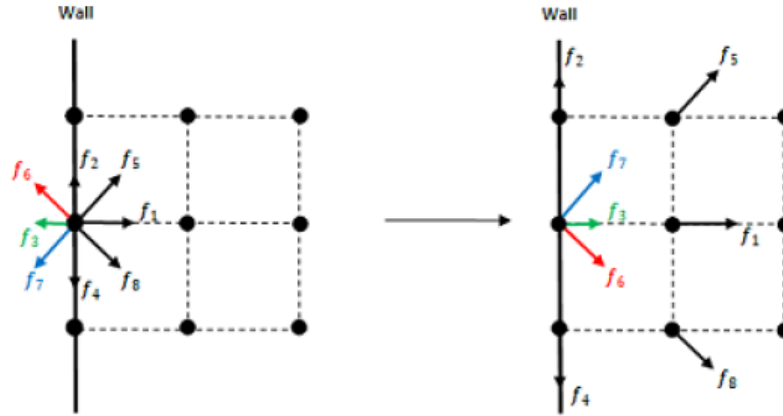


Figure 4.3: Bounce-back boundary condition, adapted from [5]

$$u^+ = \frac{1}{k} \ln\left(\frac{y^+}{A}\right) + B \quad (4.8)$$

with

$$y^+ = \frac{yu^*}{\nu} \quad (4.9)$$

and

$$A = 1 + f\left(\frac{\partial p}{\partial x}\right) \quad (4.10)$$

u^+ is defined as the dimensionless velocity, $k = 0.4$ the Von Karman constant, y^+ the dimensionless wall distance, y the vertical distance from the wall and u^* is the friction velocity. By solving these equations iteratively, the wall-shear stress $t_w = \rho(u^*)^2$ is obtained and used as wall boundary condition.

Turbulence model

The turbulence model is another critical point for numerical simulations.

If the lattice length is small enough to capture the smallest scale of turbulence, then the Lattice-Boltzmann-Method is equivalent to a Direct Numerical Simulation (DNS) of Navier-Stokes equation, until the dynamic range can be accurately covered [12]. However, especially for high Reynolds, this can become impractical for the computational effort required.

A sub-grid scale can then be used for modelling the turbulent effects, with different implementations [13].

Another approach, used by Exa PowerFLOW, is commonly defined as Very Large Eddy Simulation (VLES). The turbulent kinetic energy and dissipation are solved with a variant of RNG $k - \epsilon$ model for the unresolved scales of turbulence [12].

LBM and Navier-Stokes equations solvers

Even though the Lattice-Boltzmann-Method has been introduced as an alternative approach compared to solving the Navier-Stokes equations, it is possible to recover the NS equations starting from LBM. The whole derivation can be found in [13].

The main advantages of LBM compared to NS solvers are [12] [32] [5]:

- simulations are inherently accurate, stable and unsteady at a unitary Courant-Friedrich-Lewy condition;
- grid generation is semi-automatic, with no concern for cell quality;
- it is easier to deal with complex boundaries and geometries;
- LBM solver can easily be parallelised and so applied to large simulations;
- LBM has intrinsically low dissipative properties, which makes it suitable for aeroacoustics simulations;
- LBM is very suitable for multi-phase flows.

On the other hand, the main disadvantages are:

- for years, LBM has been applied only in flows with small Mach numbers (<0.4): even though recent implementations permit to solve also fields with higher Mach, these applications are relatively new;
- LBM is a less effective solver for steady-state flows.

These characteristics make LBM particularly suitable for flows in complex geometries, multi-component flows, aeroacoustics, turbulent flows and many others.

It can be noticed that the main disadvantages of LBM are not relevant for the current study, which deals with very low Mach numbers (always smaller than 0.1), is not subject to compressible effects and presents a fully unsteady setup.

4.1.2. Lattice creation in PowerFLOW

In EXA PowerFLOW 5.4a and in LBM in general, the concept of meshing is different from software that employ Navier-Stokes solvers. The lattice is indeed generated in a semi-automatic manner, unlike the mesh in most of the solvers.

During the discretisation phase, the simulation volume is divided into lattice elements, which are cubes (since the simulation is 3D) named *voxels*. When a voxel intersects the surface of a body, a *surfel* is defined. The surfel is a planar structure. At each time step, the particles move from voxel to voxel; if they encounter a surfel, the boundary condition is applied. Figure 4.4 shows the different lattice elements.

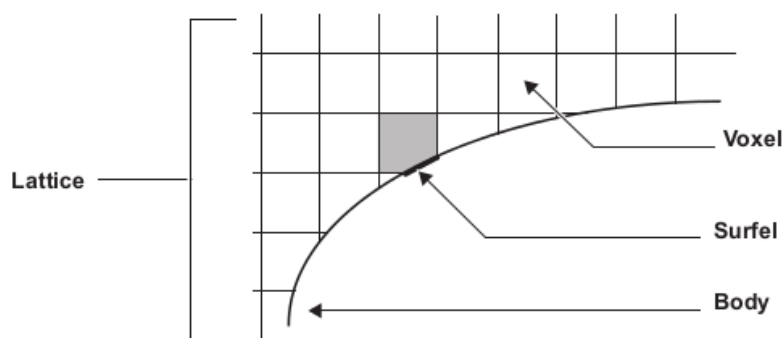


Figure 4.4: Geometry elements in PowerFLOW [14]

In order to be able to focus on the most important phenomena and to save computational time, it is possible to define Variable Resolution (VR) regions. The resolution between VR regions changes

with a factor of two. This means that each VR region will have double voxel length (so eight times bigger voxel volume) than the finer VR region and half of the voxel length of the coarser VR region, as can be seen in Figure 4.5. Consequently, the timestep used for updating the flow field is scaled with a correspondent factor of two between VR regions.

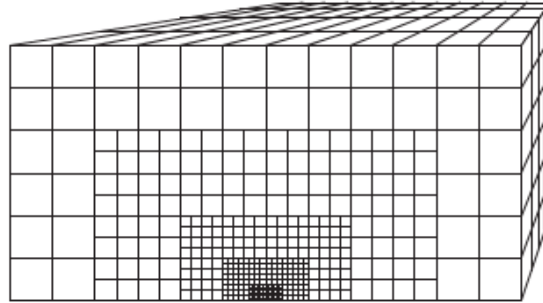


Figure 4.5: Voxel size in different VR regions [14]

It is then easy to notice how the right number and position of VR regions is essential to realise a smart lattice, compromising between accuracy and computational effort. The length of the voxel in the finest VR region is defined as the *resolution* of the case and it is one of the key parameters in PowerFLOW simulations.

A *local rotating reference frame* (LRF) can be defined for rotating parts, resulting in a different reference frame and allowing to prescribe the rotational speed. The LRF can be defined as *stationary*, suitable if the flow is axisymmetric and transient effects are negligible, or as *sliding-mesh*, suitable for more complex geometries and significant transient effects. The LRF with sliding-mesh has the significant limitation of not being able to cross in the rotation more than 2 VR regions for any 'radial ring' in which the LRF is divided, as shown in Figure 4.6.

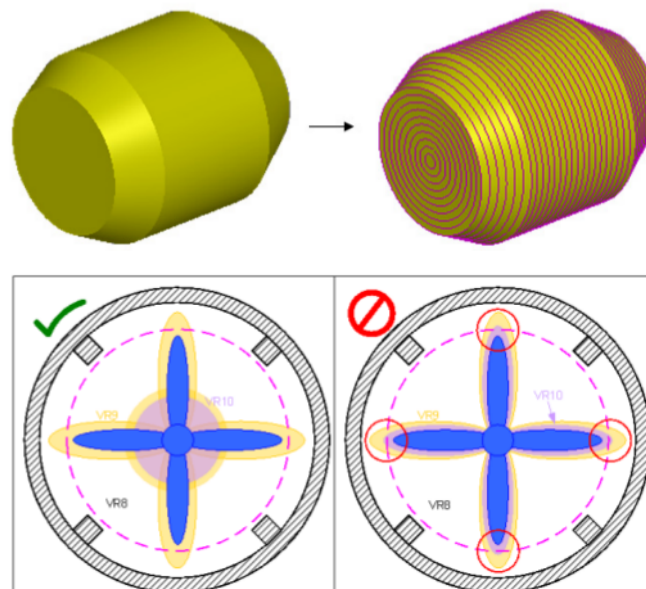


Figure 4.6: Subdivision of a body of revolution into rings (top) and interference between such rings and multiple VR regions (bottom) [14]

4.2. Acoustic solver

4.2.1. FW-H analogy implementation

The FW-H equation has been introduced in Paragraph 2.2.4. Practically, it can be chosen to integrate the pressure field on a solid or permeable surface.

- *FW-H solid integration surface*

The solid integration surface usually coincides with the surface of the body that needs to be analysed. The main drawback of this technique is that the quadrupole noise sources, i.e. the non-linearities of the flow, are not included in the calculation. On the other hand, it requires a low computation effort. Indeed, for years the low computational power of commercial machines caused only solid surface to be used, so that only the linear effects related to body thickness and aerodynamic loading were computed [10].

- *FW-H permeable integration surface*

Di Francescantonio [18] developed an extension to the FW-H analogy to a penetrable control surface. The surface is then chosen in order to include all the relevant non-linearities of the flow. However, the larger the surface, the higher will be the computational effort needed to resolve the flow, since the wave need enough resolution to propagate up to the surface, as explained in Paragraph 4.2.2. Another drawback is that spurious noise sources may be included in the calculation. These spurious sources can be due to hydrodynamic pressure fluctuations induced by eddy structures over the faces of the FW-H surface and to poorly resolved structures inside the surface [42].

Finally, since for low Mach numbers the quadrupole sources have negligible magnitude (see next paragraph), in this specific case integrating on a solid or permeable surface is expected to give small differences.

In Exa PowerFLOW, a solution of the FW-H analogy with forward-time (or advanced-time) formulation is employed [10], based in the formulation 1A by Farassat and Succi [22].

The *forward-time approach* is derived from the *retarded-time* approach. The latter evaluates the signal received by the observer in an instant of time by summing all the disturbances. These are emitted at different times and cover different distances before reaching the observer.

The forward-time approach adopts the point of view of the source, calculating the noise contributions on the current situation of the integration domain. These contributions will reach the observer at different advanced times. The signal is then calculated in observer domain by summing all the contributions.

The forward-time approach is more simple and efficient than the retard-time approach, since it does not require iterations and since it allows running aeroacoustic prediction in parallel with the aerodynamic computations [10].

4.2.2. Sampling criteria

Resolution and range of frequencies captured

In the simulations, it would be desirable to capture the largest range of frequencies possible. There are two main criteria which define what frequencies can be sampled: a spatial and a temporal criterion.

- *Spatial criterion*

The resolution of the surface where the pressure variations are collected, i.e. the FW-H integrations surface, determines what range of frequencies can be captured. A number of 10

voxels (so 10 numerical values) per wavelength is considered the minimum to detect the behaviour of a wave [54], even though a minimum of 15 is advisable [60].

In the case when not enough values are collected, the phenomenon of *aliasing* may occur. A straightforward example of aliasing for a sinusoidal wave is shown in Figure 4.7: the continuous line represents the original signal, while the dots the sampled values. Less than two values per wavelength are collected: the Fourier analysis will detect the dashed line, which is a wave with different phase and frequency from the original.

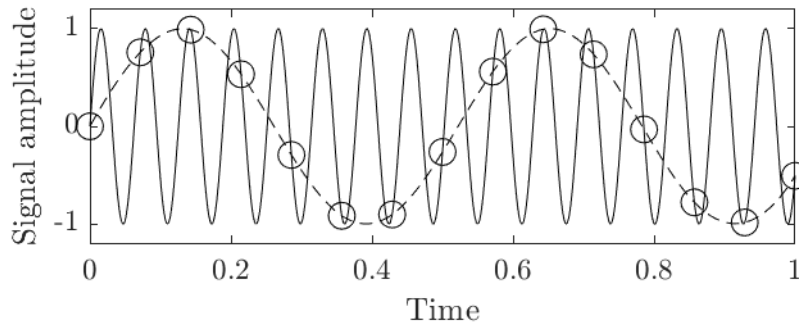


Figure 4.7: Aliasing phenomenon

The frequency of a wave is inversely proportional to its wavelength $\lambda = \frac{c_0}{f}$. The voxel size dx on the FW-H integration surface then determines the highest frequency which can be captured, according to

$$f_{max} = \frac{c_0}{10dx} \quad (4.11)$$

- *Time criterion*

Similar considerations apply for the time criterion as well: the number of values sampled should be high enough to avoid phenomena of aliasing. The sampling frequency is related to the frequency of the sound waves through the *Nyquist criterion*. The criterion states the sampling frequency should be at least double the frequency of the waves: $f_s \geq 2f$.

It is fundamental to start sampling the data only after the initial transient phase has finished. For each case, the correspondent coarser simulation was used as seeding file, initializing the flow field and thus reducing the transient time. The following criteria were employed for deciding the start time of the first measurement t_{start} . Since all these criteria have to be fulfilled, the highest t_{start} is chosen.

- The flow should have past over the object of interest at least 10 times [60], i.e.

$$t_{start} = \frac{10L}{U_\infty} \quad (4.12)$$

- One flow pass should take place throughout the whole simulation domain [60].
- A significant parameter for the current simulation needs to have reached convergence.

5

Setup

In this chapter, the details on how the turbine was modelled and on how the simulations were carried out are presented. In the first part, the turbine geometry used for the simulations is described. In the second part, firstly the characteristics of the lattice are discussed, including the coordinate systems, the computational domain size, the variable resolution regions and the FW-H surface. Afterwards, the acoustic settings, the simulation parameters and the measurements to be obtained are described.

5.1. Geometry

The geometry used for the simulations of this paper has been created from scratch on SolidWorks 2016 based on the design with 'linearised blades' by Van Dorst [61]. Figure 5.1 shows two views of the whole turbine.

Two main criteria were used to build the geometry. The first was to recreate the original geometry of the turbine accurately, especially in the most crucial parameters as the tip clearance or the blade shape. The second was to try to make the geometry as smooth as possible, in order to facilitate the discretisation process of PowerFLOW. Indeed, a sharp and complex geometry resulted often in a failure of the computation.

The geometry built can be divided into five parts, which will be described in the following paragraphs. These parts as shown in Figure 5.1 and are the zigzag trips, the diffuser, the blades, the hub, the nacelle. In the current text, the name rotor designs the group formed by the blades and the hub.

Zigzag trips

Zigzag trips have been added to the suction sides of the blades and of the diffuser. In several applications, these trips are added on blades in order to force the transition from laminar to turbulent flow regime, which helps to prevent flow separation.

In recent computations and experiment, zigzag trips are commonly used also to force the transition in a specific location. This is useful to have comparable boundary layer characteristics in different research: in aeroacoustics, defining the boundary layer development correctly is crucial to understand noise generation, especially by the trailing edge. Furthermore, forcing the transition with a zigzag trip allows avoiding phenomena of artificial laminar regime that might take place in Large Eddy Simulations. LES describe directly the major turbulent eddies: if the correct definition would fail, an artificial separation might take place on the blade [7].

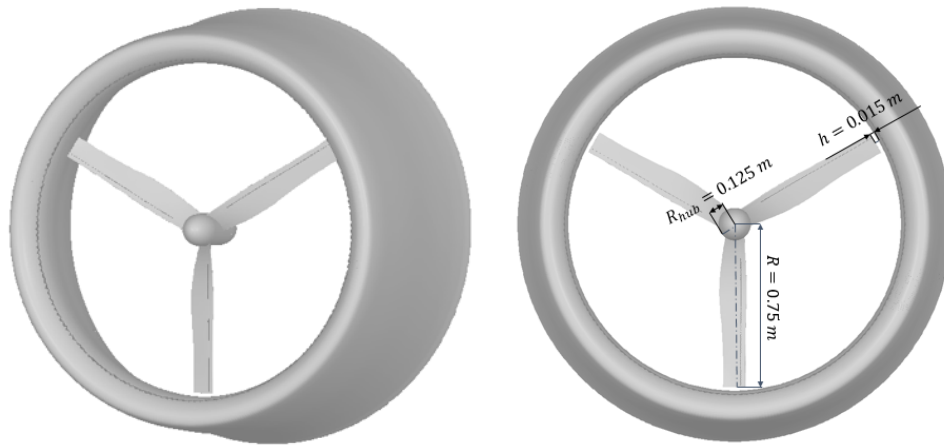


Figure 5.1: Geometry of turbine for simulations: 3-D view (left) and front view (right)

The zigzag trip on the blades is shown in Figure 5.3; its essential characteristics are displayed in Table 5.1. It is worth explaining the value of 2.7 mm for the height: this is the minimum value in order to have three local voxels along the trip height in the coarse grid refinement (see Paragraph 5.3). With less than three voxels, the step might not be solved. Moreover, such a height is large enough to cover the whole boundary layer local thickness.

The annular trip placed on the inner side of the diffuser can be seen in Figure 5.2, its geometry features are reported in Table 5.1. The trip could not be placed parallel to the flow due to a technical issue in the tool generating the trip. However, this is not affecting the ability of the trip to force the turbulent transition. In a similar manner as the previous case, the height of the trip is based on the criteria of being able to cover three local voxel lengths in the coarse refinement mesh.

In order to avoid excessive computational burden during the discretisation phase, the zigzag trip have been placed only on the suction side of the blades, i.e. the part facing upwind. The choice is due to the fact that on the suction side there are higher flow velocities, which means that flow separation is more likely to happen than on the pressure side. However, for further studies, it is recommended to place the trips on both sides. For similar reasons, no trip has been used on the pressure side of the diffuser.

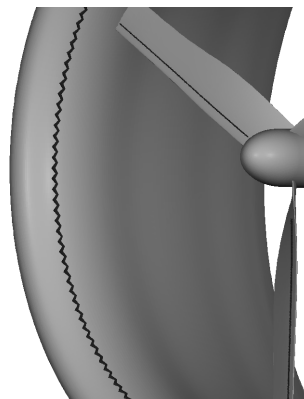


Figure 5.2: Zig-zag trip in the diffuser

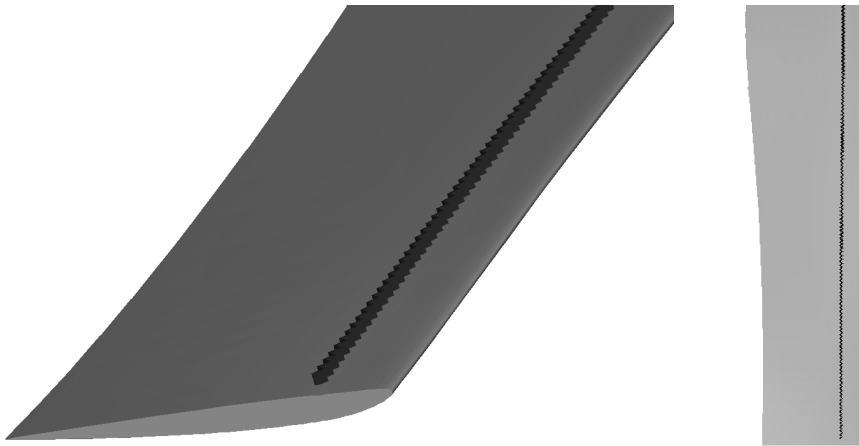


Figure 5.3: Zig-zag trip on a blade

Characteristic	Blade trip	Diffuser annular trip
Relative chordwise location	0.15	0.1
Minimum relative spanwise location	0.15	-
Maximum relative spanwise location	0.99	-
Amplitude (half chordwise length)	1 mm	1.5 mm
Height	2.7 mm	5.5 mm

Table 5.1: Characteristics of zigzag trips

Diffuser

The diffuser, also named shroud, has been created as a revolution of the annular section, as designed by NLR [44]. Figure 5.4 displays the most important characteristics of the diffuser.

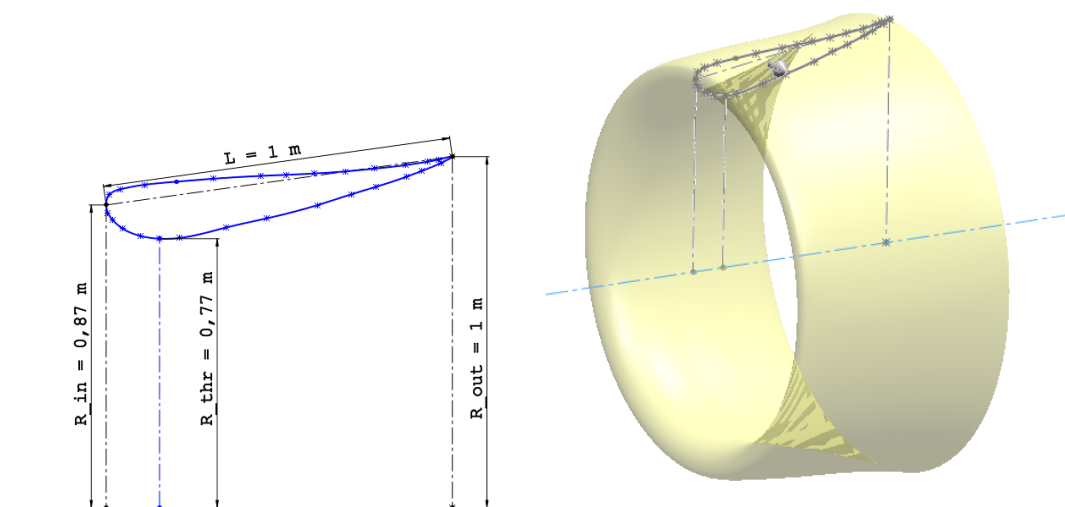


Figure 5.4: Diffuser geometrical properties (left) and creation step in SolidWorks (right)

Blades

The blades of the DonQi turbine employ NACA2207 airfoil over the whole radial span. The chord and twist distributions are shown in Figure 5.5: the distributions have been taken from the linearised model of Van Dorst [61]. The chord varies from 130mm at the root to 105mm at the tip, while the twist ranges from 40.5° at the root to 0.3° at the tip.

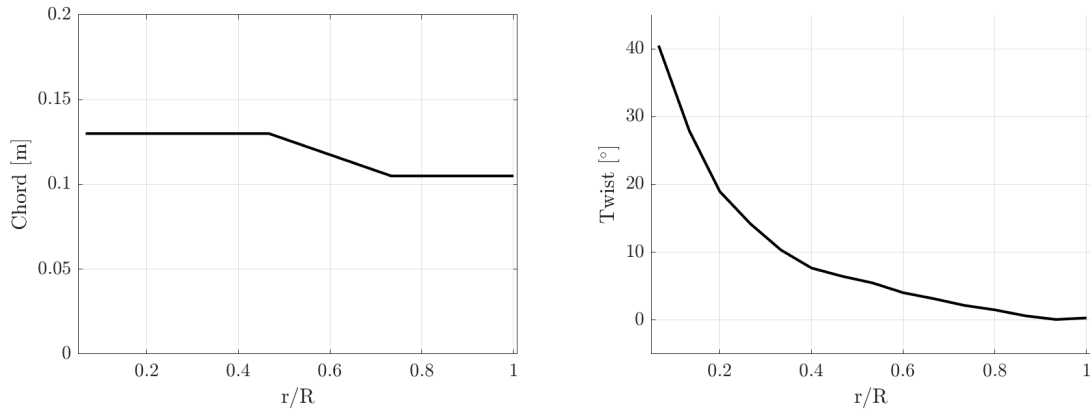


Figure 5.5: Chord and twist along the relative radial location of the blade

The three blades have been drawn with SolidWorks by creating airfoils with a constant distance of $0.05R$ between them and by using a spline interpolation between them. Since the airfoils have different chord and twist according to the radial distribution, the location at the quarter chord has been the parameter kept constant. The quarter chord location is commonly used in aerodynamics as the aerodynamic centre of the airfoil, i.e. the point where the pitching moment does not change with the angle of attack.

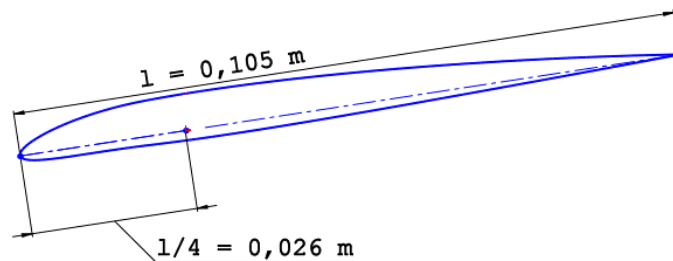


Figure 5.6: Blade airfoil geometrical properties

Hub

Detailed information were not available about the hub and the nacelle. Therefore, a simple shape resembling the original model was adopted. The hub is composed of a cylinder with a diameter of 125mm and a length of 100mm , where the three blades are attached, and by an upwind part. This part is obtained through the rotation of half an ellipsis, with one of the axis that corresponds to the diameter of the cylinder and the other with semi-length of 125mm . Such a volume is half of an ellipsoid of revolution. The hub is shown in Figure 5.7.

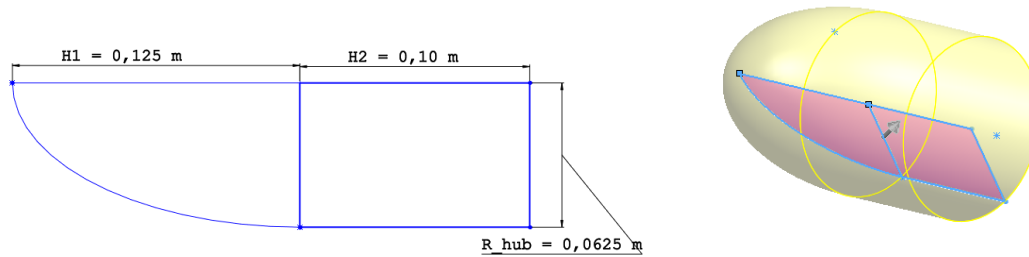


Figure 5.7: Hub geometrical properties (left) and creation step in SolidWorks (right)

Nacelle

The nacelle has been drawn in an analogous way as the hub, but with cylinder length of 75 mm and the length of the ellipsoid of revolution of 100 mm . The reason to distinguish between nacelle and hub is that, even though the geometries are similar, the former is not rotating in the simulations, while the latter is.

Matching parts and simplifications

In the rotor-nacelle complex, the blades have been inserted in the cylindrical part of the hub, while the cylindrical basis of the nacelle and the hub have been simply matched. The rotor was positioned so that the blades are located in the throat of the diffuser. The clearance between the blade tip and the inner wall of the diffuser is set to 15 mm as in the original geometry.

It is worth noting that the Gurney flap was not added in this analysis, in order to isolate the effect of the diffuser and of the tip clearance on the acoustic properties. Also, the pierced plates for noise reduction, the tower and the nacelle support structure which are present in the real model have not been included in the current study.

5.2. Coordinate system

In the definition of the lattice, two cartesian coordinates systems are used: a global and a local coordinate system. The coordinate systems are showed in Figure 5.8.

The global coordinate system $\{X_g, Y_g, Z_g\}$ is in-built with the computational domain. The X axis is positioned in the wind direction, pointing downstream. The Y and Z axis are then subsequently defined as a cartesian tern. In the non-yawed case, the geometry is axisymmetric, hence the direction of Y and Z does not need to be described. In the yawed case, the turbine is tilted of 7.5° in the positive direction around the Z axis. The yaw angle is then defined in the plane X-Y. The origin is placed in the 'tip' of the hub: such a location is useful to define the planes perpendicular to the rotor axis (with constant X) where some results are collected.

The local coordinate system $\{X_l, Y_l, Z_l\}$ is in-built with the turbine in the inertial reference system, hence not rotating. In the case without yaw, the orientation of the three axes coincides with the axis of the global coordinate system. In the yawed case, the definition of the local coordinate system is analogous, but being the DAWT tilted compared to the computational domain (the reason for this choice is explained in 5.3) the local system is tilted as well.

In the current work, the local coordinate system is made non-dimensional by using the diffuser chord L . Hence, it is obtained $\{\hat{x}_l, \hat{y}_l, \hat{z}_l\} = \{X_l/L, Y_l/L, Z_l/L\}$.

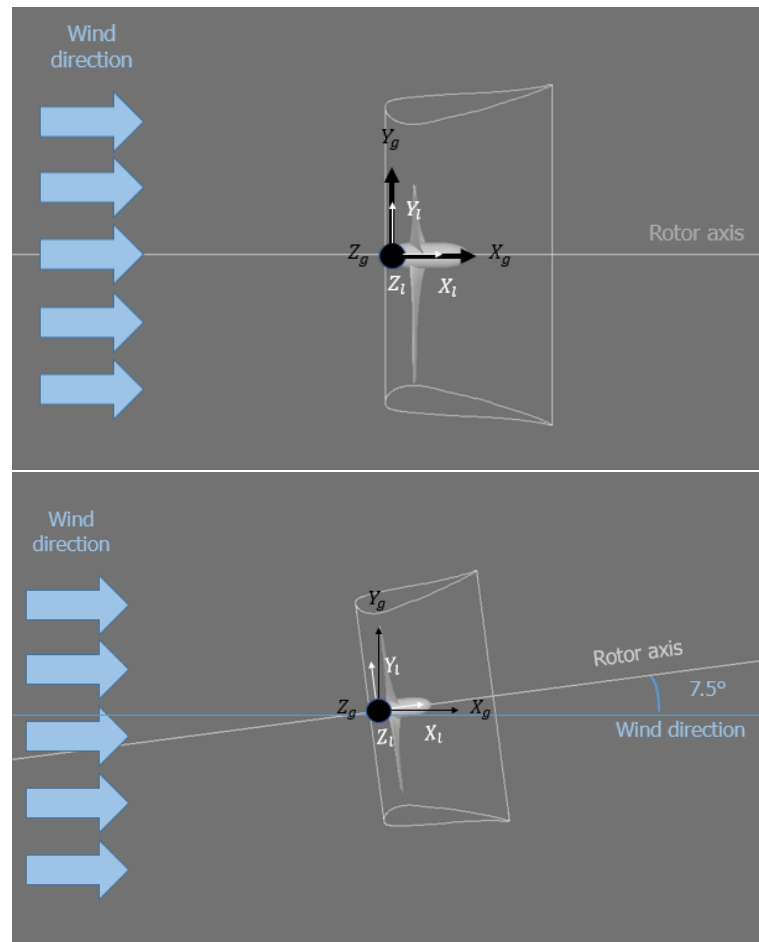


Figure 5.8: Global and local coordinate systems in the geometry, in the non-yawed (top) and in the yawed case (bottom)

Finally, an azimuthal angle ϕ is defined in order to characterise the flow on the blades when rotating in yawed inflow conditions. The angle is defined as rotating clockwise when looking downwind, with the 0° position defined as towards the negative Z direction in the local coordinate system. Figure 5.11 shows the definition of such angle.

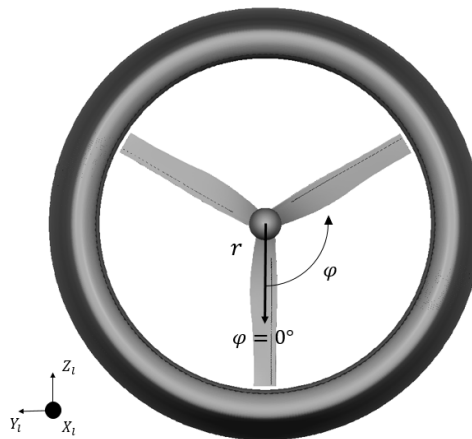


Figure 5.9: Azimuth angle ϕ definition, with local coordinate system as reference.

5.3. Lattice

Nine different VR regions are used in the simulations: VR9 is the most detailed one, where the voxels have the smallest size, while VR1 represents the coarsest level.

Four different mesh refinements have been realised for the computations of the case, resulting in very coarse, coarse, medium and fine resolution. The different voxel length used in each refinement and in each region is summarised in Table 5.2. Hereafter, Table 5.3 shows a summary of the VR regions, including the voxel size and the number of voxels contained in each VR for the finest resolution scale. Such VR regions are hereafter described.

	dx_9	dx_8	dx_7	dx_6	dx_5	dx_4	dx_3	dx_2	dx_1
Very coarse	-	2.50	5	10	20	40	80	160	320
Coarse	0.88	1.77	3.54	7.07	14.14	28.28	56.57	113.14	226.27
Medium	0.63	1.25	2.50	5	10	20	40	80	160
Fine	0.42	0.83	1.67	3.33	6.67	13.33	26.67	53.33	106.67

Table 5.2: Voxel size, in millimeters, in the four mesh refinements employed for the simulations

	Position	Voxel size [mm]	Number of millions of voxels
VR9	Offset around blade trip	0.42	1.72
VR8	Offset around rotor and diffuser trip	0.83	12.49
VR7	Offset around rotor and diffuser	1.67	103.81
VR6	Box around DAWT	3.33	164.11
VR5	1st box around DAWT and wake	6.67	80.22
VR4	2nd box around DAWT and wake	13.33	24.12
VR3	3rd box around DAWT and wake	26.67	13.62
VR2	4th box around DAWT and wake	53.33	10.1
VR1	5th box around DAWT and wake	106.67	7.07

Table 5.3: Summary of the VR regions, with position, voxel length and voxels number referred to the fine mesh resolution

VR inside and around the DonQi turbine

The region inside and around the DAWT is the most difficult to model, since it is the area where the most delicate phenomena take place and since the appropriate choice of VR has to deal with the presence of the local rotating frame. It should be noted that all the regions are identified by a precise number of local voxels: since the size of the voxel decreases with mesh refinement, this means that the region becomes correspondently smaller. This choice allows a more straightforward creation of setups with different mesh resolution and makes sure that a proper number of voxels is always present. This is a crucial issue especially in some delicate

parts, as the zigzag trips or the gap between tip and diffuser. The three finest VR regions and the LRF are located here: each of them is now shortly described.

- *VR9* (red in Figure 5.10)

VR1 is the finest scale of resolution: it is used to resolve the region around the zigzag trips of the blade. The shape used is an offset of $6dx_9$, i.e. six local voxel lengths, surrounding the trips.

- *VR8* (orange in Figure 5.10)

VR8 is employed in the region surrounding the blades and the hub and around the zigzag trip of the diffuser. The part around the rotor is an offset of $7dx_8$.

The number is a trade-off between: 1) having a vast region with high resolution around the rotor, necessary to describe with precision the critical phenomena as the forces acting on the blades or vortex shedding; 2) let *VR8* lie entirely inside the local rotating frame: an intersection of *VR8* with the LRF may result in numerical artefacts since small *VR8* would remain non-rotating.

Around the diffuser zigzag trip, *VR8* is delimited by an offset of $6dx_8$. Since the trip has a height of $3dx_8$, there are three voxel length for the region above the trip, which are sufficient for resolving the flow correctly.

- *Local Rotating Frame* (light orange in Figure 5.10)

The LRF is not a variable resolution region; thus the size of its voxels is defined by *VR7* region that entirely contains the LRF. However, it is described here since its definition affects the distribution of adjacent VR regions. As *VR8*, it is also delimited by a volume created by the revolution of an offset around the rotor, spaced $5dx_8$ from the rotor itself. This value comes from conciliating the requirements that 1) LRF should contain *VR8*, as described above; 2) *VR7* should surround the LRF acting as a 'protection', so that the LRF rings do not intersect more than two VR regions causing a fatal error as described in 4.1.2.

- *VR7* (yellow in Figure 5.10)

Two parts compose *VR7*: an offset around the rotor disk, more extensive than *VR8* and containing the LRF, and an offset around the diffuser. The former offset amounts to $12dx_7$, while the latter to $5dx_7$. It is worth pointing out that, while *VR8* is a rotating offset around the blades and the hub, *VR7* surrounds the whole LRF, not rotating with the blades. In the case of *VR7*, the trade-off is between merely having detailed flow information around the rotor and not imposing a too high computational cost. The two parts overlap in the region around the tip clearance in order to ensure continuity in the region and avoid artefacts.

VR outside the DonQi turbine

The region outside the DAWT includes six boxes which delimit increasingly coarser VR regions. The largest box also defines the limits of the computational domain.

The box shape has been preferred in order to be able to define precisely the location of all the voxels, obtaining regular VR regions shapes. Cylinders and truncated cones, which would have also been legit choices and would have allowed saving the axisymmetry or following the wake expansion, would have resulted in sharp-steps border between VR regions, more difficult to predict. All the boxes are built with dimensions which are multiples of the local voxel size.

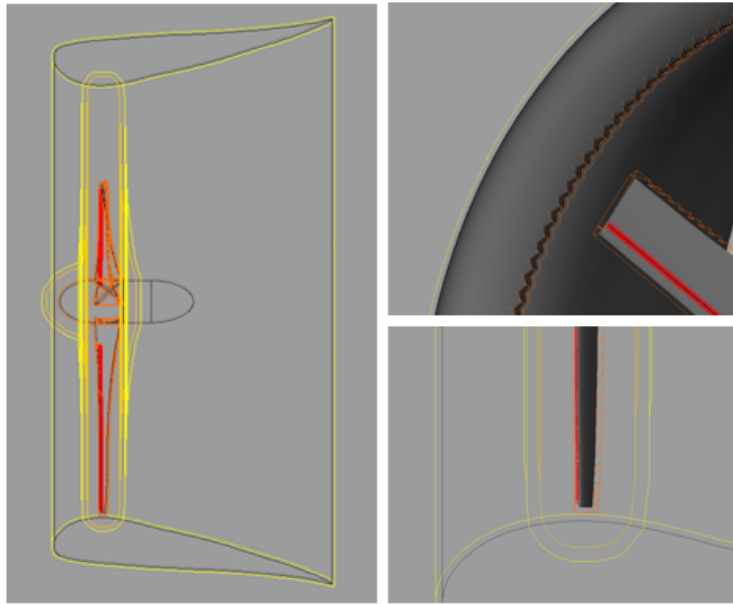


Figure 5.10: VR inside the turbine and around the diffuser (left), zoom on the diffuser trip (top right), zoom on blade tip (bottom right)

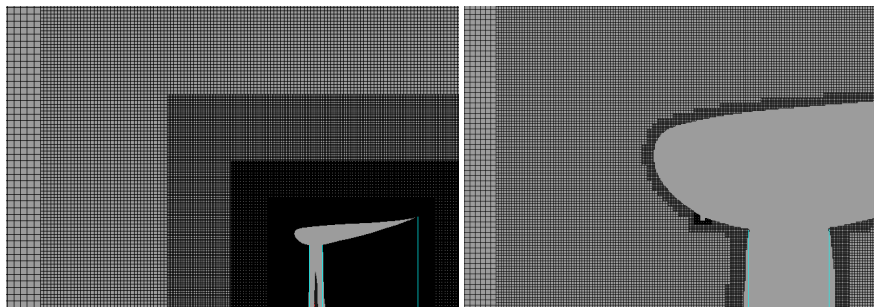


Figure 5.11: Examples of grid refinement according to VR regions

For what concerns the very coarse, coarse and medium mesh refinements, the size of each region decreases with the local voxels as described in 5.3. Between the medium and fine setup, the dimensions of the regions are kept constant. This is done in order to prevent the boxes to get too much close to the turbine and to keep the FW-H permeable surface in the same position, which is favourable for a better comparison between acoustic results.

The VR regions outside the DAWT can be seen in Figure 5.12.

- *VR6* (green in Figure 5.12)
 VR6 is employed in the region immediately around the DAWT. Geometrically, it is a box with $265dx_6$ of length (in the wind direction) and $460dx_6$ of width and height.
- *VR5* (white in Figure 5.12)
 VR5 outlines the region around VR6 including the first development of the wake. Its shape is then a box with $365dx_5$ of length and $290dx_5$ of width and length. VR5 also defines the shape of the FW-H surface, as will be described in 5.4.
- *VR4, VR3, VR2 and VR1* (increasingly dark shades of blue in Figure 5.12)
 The following four VR regions with increasing coarseness. The dimensions of the boxes are such that they increase proportionally: each one is 25 local voxels larger in the up-

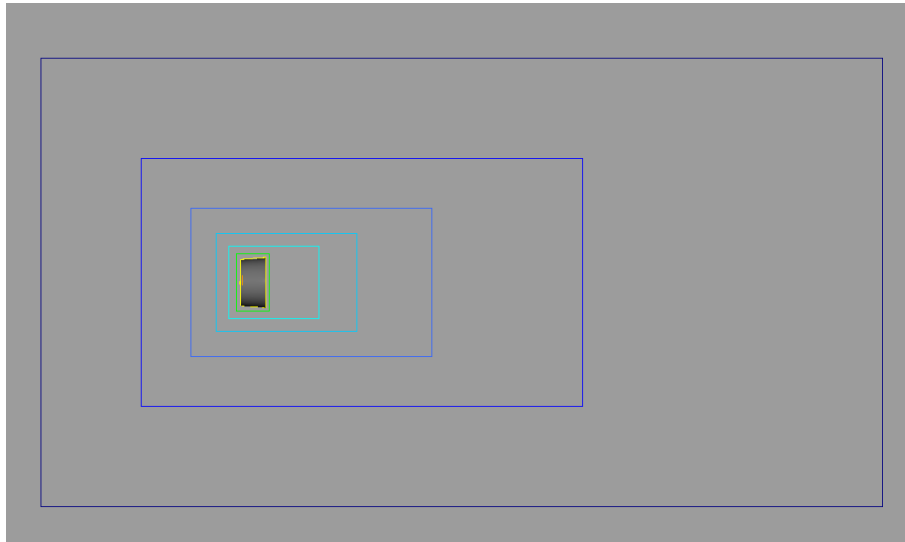


Figure 5.12: VR regions around the DonQi Turbine

wind direction and in the four side directions and 75 in the downwind direction, to describe the effect of the wake. On the other five directions, the flow velocity is expected to be sooner close to the values of the undisturbed flow.

– *Simulation volume boundaries*

As mentioned before, the largest box defines VR1 and represents the boundary of the simulation domain. Since the inlet, the outlet and the four sides are designated as solid walls, in order to avoid artefacts at the corners of the domain, these boundaries are placed inside the computational domain as boxes with thickness of $1dx_1$.

The inlet is then placed at $9.11m$ upwind from the origin, the outlet at $29.31m$ and the lateral walls at $10.23m$, referring to the local coordinate system in the medium and fine mesh resolution.

Setup modification for yawed case

The present setup needs to be slightly modified to be adapted for the case with 7.5° yawed inflow.

Firstly, the turbine is tilted around the Z-axis, with the wind direction kept constant. The option of keeping the turbine in the same position and tilting the setup has been discarded because of possible artefacts in the interaction between the boundaries and a skewed flow.

Since the turbine is tilted, the second modification is a slight expansion of VR5 and VR6, in order to contain the turbine thoroughly. VR4, VR3, VR2 and VR1 are adapted consequently according to the voxel offset described in the previous paragraphs. In order to minimise the impact of this adjustment on the acoustic results, the position of the FW-H permeable surface is kept the same as in the non-yawed case. The VR regions around the diffuser and the rotor do not need any correction, since they are all defined as offset from solid bodies.

The case setup is shown in Figure 5.13.

5.4. Acoustic settings

In the current analysis, the acoustic data are obtained with FW-H analogy by integrating the pressure variations both on a solid surface and on a permeable surface. The solid surface is

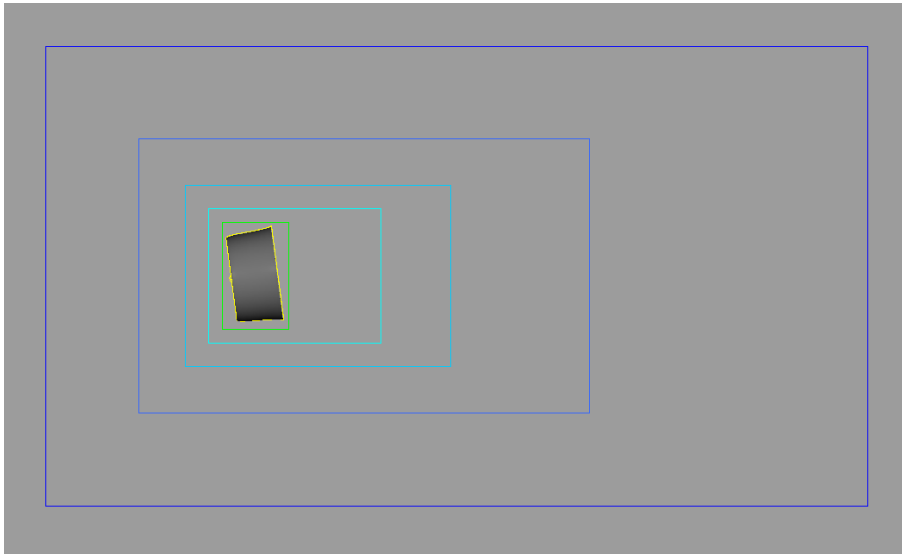


Figure 5.13: VR regions around the DonQi Turbine in the yawed case.

easily defined as the wall of the solid elements of the DonQi Turbine, i.e. diffuser, rotor, nacelle and zigzag trips. Conversely, the choice of a permeable surface needs to be done carefully.

FW-H permeable surface

The FW-H permeable surface where the pressure variations will be collected needs to be placed so that it complies two different requirements.

- The first requirement is that the FW-H should be large enough to include all the relevant noise sources. These are not known a priori before the acoustic analysis. However, it can be assumed that the most relevant noise sources will be next to the surfaces of the DonQi Turbine and in the immediately downwind region, where the magnitude of the vortex scattered will be higher.
- The second requirement is that the FW-H surface should lie in a region with enough resolution to capture high frequencies, as imposed by the spatial criteria exposed in 4.2.2. In a typical spectrum of the noise produced by a wind turbine, for frequencies higher than 500 - 1000 Hz the sound power level starts to decrease, and becomes negligible at very high frequencies [48]. The target for the maximum frequency to be sampled is set in this case to 5kHz for the finest resolution region in the medium resolution case. Such a frequency corresponds to a wavelength of 113.3mm : according to the criteria explained in Paragraph 4.2.2, the voxel length in the region of acoustic sampling should then be at maximum 11.33mm .

The trade-off reached in this study is to place the FW-H surface inside the VR5 region, as shown in Figure 5.14.

The VR5 region has voxels with length of 10mm in the medium resolution case and of 6.6mm in the fine case, which allow collecting frequencies respectively up to 3.44kHz and 5.22kHz . However, since some authors [60] recommend 16 voxels per wavelength rather than 10, care should be taken for frequencies higher than respectively 2.15kHz and 3.26kHz . The surface geometry mimics the resolution boxes: upwind and on the sides so that it lies in regions with almost undisturbed flow; downwind, it includes the first part of the wake.

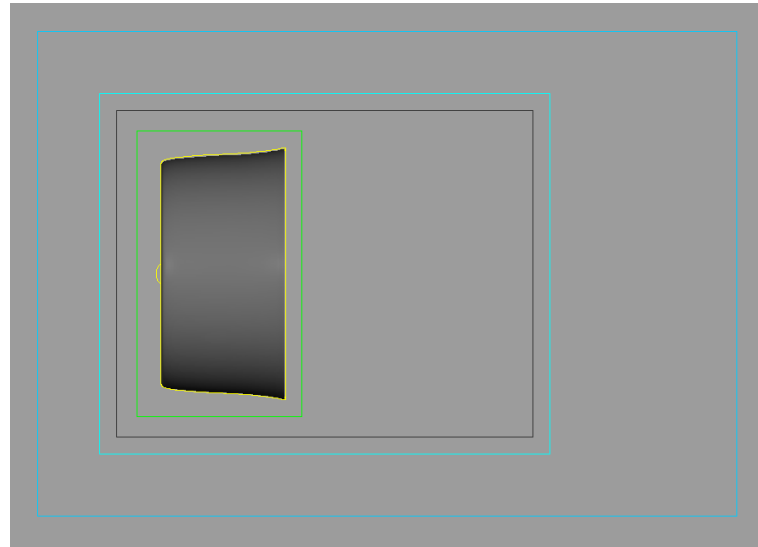


Figure 5.14: FW-H permeable surface, in black

Capturing a bigger part of the wake would have resulted in high computational cost, without a significant benefit for the noise analysis. Indeed, it should be remembered that for low Mach number the free turbulence is not a relevant noise source, as explained in 2.2.5.

Acoustic sponge

One of the problems of having a computational domain which is limited in the space is that acoustic waves may reflect and affect the sound measurements artificially. Treatments can then be used at the simulation volume boundaries to prevent these effects [40].

This may happen as well with acoustic waves, which can be 'reflected' by the boundaries of the domain. In order to prevent the phenomenon, an *acoustic sponge* is used in the simulation.

The parameter $\Gamma = \frac{Nu}{T}$ can be modified in PowerFLOW in order to damp the acoustic waves at the extremes of the computational domain. Three regions are outlined, correspondent to different values of Γ . The three regions are displayed in Figure 5.15.

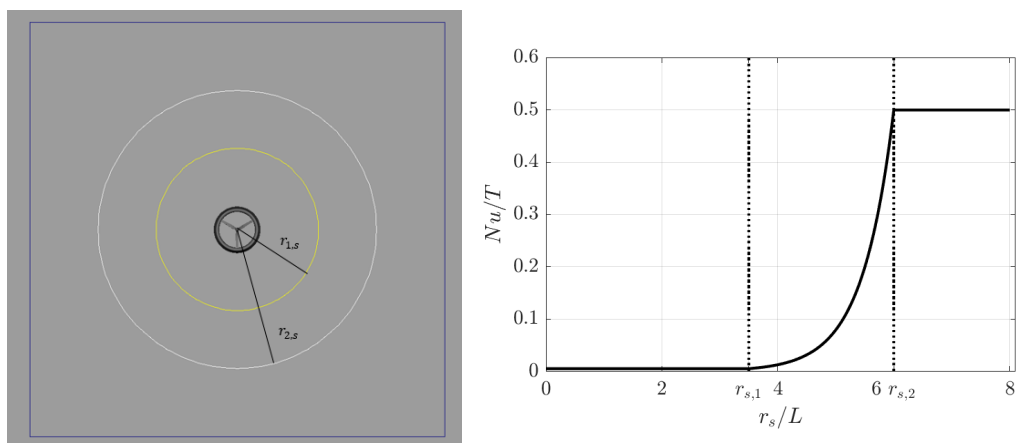


Figure 5.15: Spheres delimit the three sponge regions (left) and Γ function (right)

- Inner region. The region is contained inside a sphere with radius $r_{s,1} = 3.5m$ centred in the origin. It is the part of the domain where the most important noise sources and the

most interesting acoustic phenomena are located. There, the damping has a minimum value of $\Gamma_{min} = 0.005$.

- Outer region. The region is defined outside of a sphere with radius $r_{s,2} = 6m$, which is approximately at half the distance between the first sphere and the extremes of the computational domain. In this zone, the damping is maximum to avoid the acoustic waves to reflect back in the domain, with $\Gamma_{max} = 0.5$.
- Transition region. The region is between the two spheres, where the values of the damping increase from Γ_{min} to Γ_{max} , according to

$$\Gamma = K_B \exp^{K_A * r_s} \quad (5.1)$$

where r_s is the distance from the origin and K_A and K_B are defined as

$$K_A = \frac{\ln(\frac{\Gamma_{min}}{\Gamma_{max}})}{r_{s,1} - r_{s,2}} \quad (5.2)$$

$$K_B = \Gamma_{min} = \frac{\Gamma_{min}}{\exp^{K_A r_{s,1}}} \quad (5.3)$$

Microphones position

The results for Section 8.1 and Section 8.2 have been processed using Exa PowerACOUSTICS and a tool named *OptydB*, developed by D. Casalino. The former software is used for Far-Field Analysis (FFA) using an advanced time approach (see 4.2) from the FW-H integration surface. The latter was employed to compute the Sound Pressure Level in these points with the Fast Fourier Transform and to combine all the spectra in order to describe the Sound Power Level of the system.

The points where the noise pattern is computed, named 'microphones' in analogy with the experimental tools, are placed in four archs around the DonQi Windmill, distanced by 90° by each other. Each arch covers a sideline angle from 30° to 150° in the wind direction. The microphones are spaced 3° along the arch, which leads to 40 microphones per arch and 160 in total. The radial distance is set to $8L$ from the center of the turbine. The position of the microphones is shown in Figure 5.16.

The number of microphones and the length of the arches are chosen as a trade-off between the accuracy in representing the noise characteristics and the computational time, since a FFA employs more than one day with the current setup. The radial distance was chosen to be far from the turbine, making the FFA meaningful, but inside the computational domain.

5.5. Simulation settings

5.5.1. Global characteristics

Exa PowerFLOW requires the definition of few characteristic parameters with the function of reporting measurement in dimensionless form and to establish a dynamic range for the case [14]. These characteristics, as well as what they represent, are shown in Table 5.4.

A key parameter is the *simulated Mach number*. Since for Mach number lower than 0.4 flow results tend to be independent of the specific Mach number, PowerFLOW as default setting runs the simulation at the higher Mach number possible [14]. This allows reducing the simulation time without compromising the results quality. However, this feature is deactivated for the current simulations, because an artificial increase of the Mach number would cause

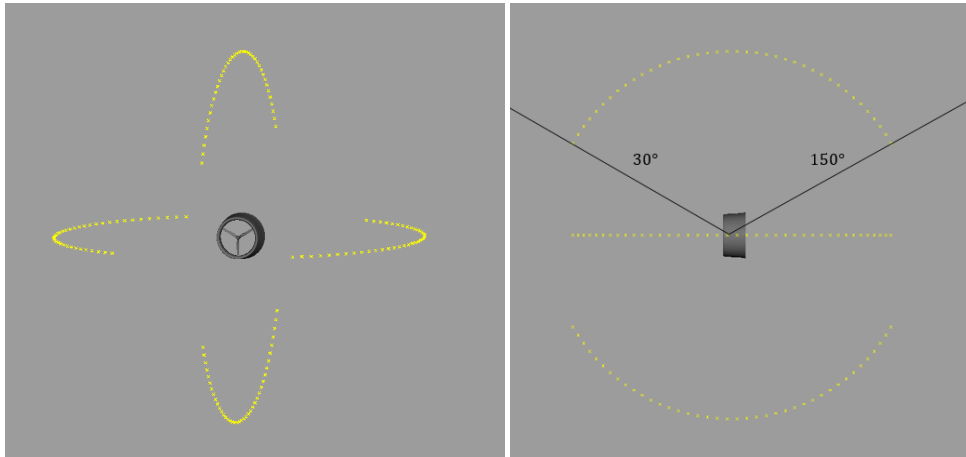


Figure 5.16: Microphones position around the turbine

Characteristic measure	Value	Details
Pressure	101325 Pa	Standard pressure
Velocity	30 m/s	Rotor tip speed
Temperature	288.15 K	Standard temperature
Viscosity	$1.51 * 10^{-5} m^2/s$	Standard air viscosity
Area	$1.78 m^2$	Rotor swept area

Table 5.4: Characteristic measures of the simulation

the acoustic waves to propagate with a non-correct velocity, jeopardising the veracity of the results.

As turbulence parameters, the *turbulence intensity* is set as 1% of the local velocity and the *turbulent length scale* with the default value of 5mm.

5.5.2. Boundary conditions

Boundary condition measure	Value
Free-stream wind speed	5 m/s
Free-stream Mach number	0.015
Rotor rotational speed	39.84 rad/s
Turbulence intensity	1%
Turbulent length scale	5 mm

Table 5.5: Global characteristics of the simulation

The simulation uses the following boundary conditions, whose values are summarised in Table 5.5:

- The inlet is set as pressure and velocity inlet, with atmospheric pressure and free stream wind speed of $5 \frac{m}{s}$. This value is likely in urban environment where the DonQi Urban Windmill should most commonly be used.
- The outlet is a pressure outlet with free flow direction, with the atmospheric pressure as specific value.
- The side boundaries are frictionless walls. The lack of friction eases the calculations and avoid artefacts.
- The solid surfaces are set as standard walls, which means that the viscous effects are considered and therefore the boundary layer is developed.
- The rotational speed of the LRF has been prescribed to $\Omega = 39.84 \text{ rad/s}$, which corresponds to a tip speed ratio of 6 for the turbine, found by Van Dorst [61] to be ideal for these wind conditions.

5.5.3. Time-convergence of simulations

Referring to the criteria listed in Paragraph 4.2.2, the diffuser chord L was taken as length of interest for measuring the 10 times flow passing.

The thrust coefficient on the rotor was used as a measure for convergence, i.e. t_{start} if $\Delta C_T < \epsilon$. It was employed for two main reasons: the first is that, since this was often the criteria with the highest t_{start} , a parameter which was fast and easy to check was required in order to optimise the time resource; the second is represented by the usage of the C_T for the first part of the grid independence analysis, performed in Paragraph 6.1.

The C_T value never remains exactly constant, given the turbulent unsteady inflow. A variation of less than $\epsilon = 2\%$ of the mean value over one revolution was used to consider the parameter stable and the measurements unaffected by transient phenomena. Figure 5.17 shows as example the convergence of C_T for the yawed case with medium resolution.

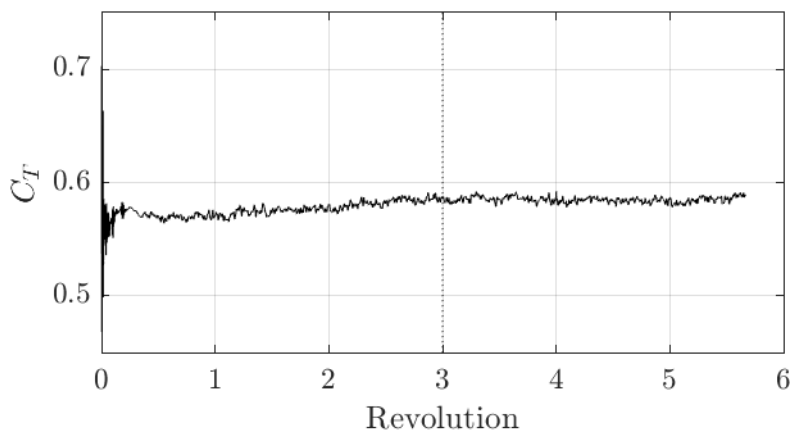


Figure 5.17: C_T convergence for yawed case with medium grid refinement, with dotted line to indicate the start of sample time

5.5.4. Measurements

The choice of which data to collect during the simulations is a trade-off between having exhaustive measurements and memory requirements. The size of measurement files is often in the order of dozens of Gigabytes, which means that a whole set of measurements can occupy more than a

Measurement	Position	Sampled measures	Sampling frequency	Time averaging	Spatial averaging
Average flow field [◊]	Simulation domain	Pressure, velocity	Ω	Ω^{-1}	1 dx
Instantaneous flow field [◊]	Simulation domain	Pressure, velocity	f_{fl}	1 ts	1 dx
Flow field on planes	Planes $\hat{z}_l = 0, \hat{y}_l = 0^*$ $\hat{x}_l = 0.1, 0.35, 1.1$	Pressure, velocity	f_{ac}	f_{ac}^{-1}	1 dx
FW-H solid	Solid surfaces	Pressure	f_{ac}	f_{ac}^{-1}	4 dx
FW-H permeable	FW-H permeable surface	Pressure, velocity	f_{ac}	f_{ac}^{-1}	1 dx
Forces	Solid surfaces	Forces, moments	f_{fl}	f_{fl}^{-1}	1 surfel

Table 5.6: Summary of the collected measurements. * denotes a measurement collected only in yawed case, [◊] a measurement not collected for fine mesh resolution.

Terabyte, making the storage of files a significant constraint. Besides files storage, excessive measurement set size in a single simulation was found to cause fatal errors in the initialisation phase of the simulations.

The period of collection of data in n VR region is always set as multiple of $2^{(n-1)}$ timesteps. This ensures that the data of the n VR regions are synchronised, since the update time of each VR region is double of the coarser VR region.

The measurements are summarised in Table 5.6. In the simulations with very coarse, coarse and medium grid refinement it was possible to collect all the measurements in Table 5.6, whereas with the fine grid it was chosen not to capture the average flow field and the instantaneous flow field.

A fluid frequency of $f_{fl} = 100\text{Hz}$ was used to capture the instantaneous flow field and the forces, which did not require higher frequency to depict their behaviour in time. The measurements on the surface and solid surface for FW-H analogy were captured with an acoustic frequency of $f_{ac} = 10\text{kHz}$, chosen as described in Paragraph 5.4. The same frequency was used to collect the flow data on the planes, in order to be able to perform the azimuthal and duct modes analysis. These planes, shown in Figure 5.18 were chosen as representative of the flow respectively just before the rotor plane, after the rotor plane and after the diffuser exit.

For what concerns the time averaging, usually the signal is averaged over a period equal to the opposite of sampling frequency, which means that each timestep contributes equally to the measurement. The only exception is the instantaneous flow field, which is sampled with the purpose of depicting the flow pattern in a single timestep and therefore not averaged.

In the space averaging, all the measurements do not average the data except the solid FW-H surface. This is due to the requirement of reducing the high amount of data generated by the measurement. Furthermore, it allows a better comparability with the data FW-H permeable surface.

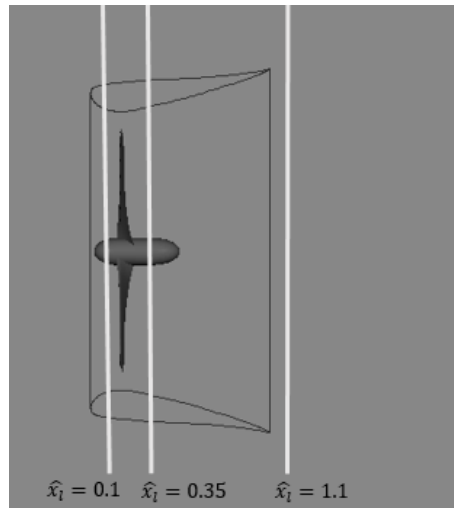


Figure 5.18: Axial planes where data are sampled.

Since the solid measurements are collected in VR7 and the permeable in VR5, a spatial averaging of four voxels ensures that the two measurements have the same spatial resolution.

6

Validation

In this Chapter, the validation of the current methods is carried out. The mesh convergence represents an essential part of the validation: since both fluid-dynamic and acoustic results will be shown, both the aspects are checked. The first section shows the sensitivity of the thrust coefficient to the mesh resolution. The second section presents the acoustic convergence study, focusing on PWL and directivity as the key parameters.

Finally, a comparison of the pressure coefficient on the diffuser is carried out, in order to validate the model against other analytical and experimental results on the DonQi Windmill.

6.1. Forces convergence

In order to check the fluid-dynamic convergence, the thrust coefficient of the rotor C_T is chosen as significant parameter. It is considered one of the most important physical quantities in a wind turbine: it gives an indication of its performance, of its operating condition and of the aerodynamic response of the blades. Indeed, it is often used in literature and allows drawing comparisons with similar cases.

The resolution of the grid is expressed through the non-dimensional wall distance y^+ , employed in the wall model as described in Paragraph 4.1.1. The smaller the y^+ value, the higher the grid refinement.

	Smallest voxel size [mm]	y^+	Number of voxels per blade chord
Very coarse	2.5	100	42
Coarse	0.88	70.7	59
Medium	0.62	50	84
Fine	0.41	33.3	126

Table 6.1: Resolution details in current simulations

Table 6.1 shows the different grid resolutions simulated in the three cases in order to test the independence of the results from the grid dimensions. The y^+ shown is the average value at an arbitrary location at the blade trailing edge at the radial location of $r/R = 0.9$. As a reference, in the ducted case in nominal conditions with medium grid resolution, the y^+ value varies from 20 to 50 on the blade surface. The only exception is the area around the trips, which because of the higher refinement and the lower flow speed presents y^+ in the range of 4 to 5.

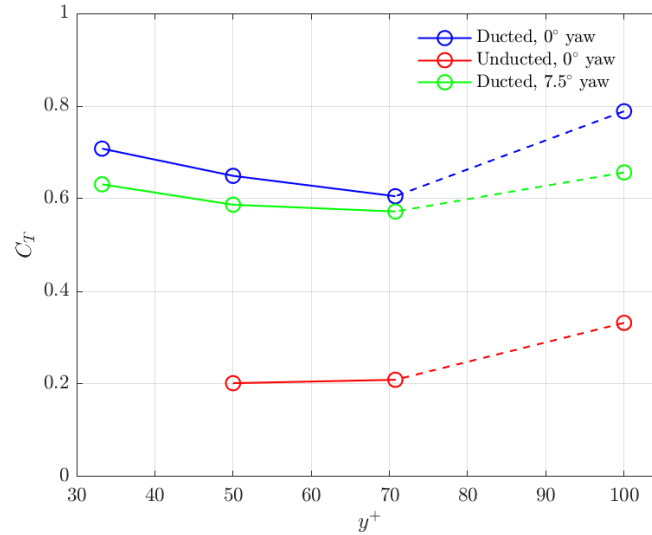


Figure 6.1: Values of thrust coefficient according to mesh resolution, expressed through the y^+ at the blade trailing edge at $r/R = 0.9$. The line between coarse and very coarse simulations is dashed since the latter lack zigzag trips.

Figure 6.1 displays the value of C_T reached after convergence in each simulation according to their resolution, expressed through their y^+ value. The first value obtained in each case is distinctly not in line with the prevailing trend. This can be explained by considering that the very coarse simulation is performed without the zig-zag trip on the blades and on the diffuser (when present). Therefore, the condition the boundary layer of the blades and of the diffuser is not comparable in the very coarse and in the other simulations.

For what concerns the unducted case, the trend is clearly decreasing with the increase of the resolution, with a difference between the coarse and the medium grid of 3.5% of the total value. In the ducted case without yaw, excluding the very coarse simulation, the trend is increasing with the resolution, with 9% higher C_T in the fine refinement compared to the medium. Similar considerations apply for the yawed case as well, with C_T increasing by 7% between medium and fine resolutions.

The differences in terms of vortices resolution between medium and fine simulation are shown through the vorticity magnitude ω , for the ducted case without yaw in Figure 6.2. The values are normalised with the arbitrary reference value $\omega_{ref} = 150s^{-1}$.

Even though these differences are not negligible, a too high amount of computational time would have been needed to run more simulations with higher refinement. A comparison with values of thrust and power found in the literature for the DonQi Windmill is then necessary to understand whether the current mesh is accurate enough to considerate the results valuable. The ducted case without yaw is used for the comparison.

	Current value	Experiments - ten Hoopen	Experiments - Dighe
C_T	0.708	0.679	0.818

Table 6.2: Thrust coefficient in current and past research on DonQi Windmill

Table 6.2 shows the C_T values obtained in similar research: the experimental campaigns on the DonQi Windmill by Ten Hoopen [58], who employed the real DonQi rotor, and by Dighe [19], who used a porous disk to simulate the turbine. It can be seen that there is a good agreement between the three cases and that the current setup results in an acceptable value. The current setup is then

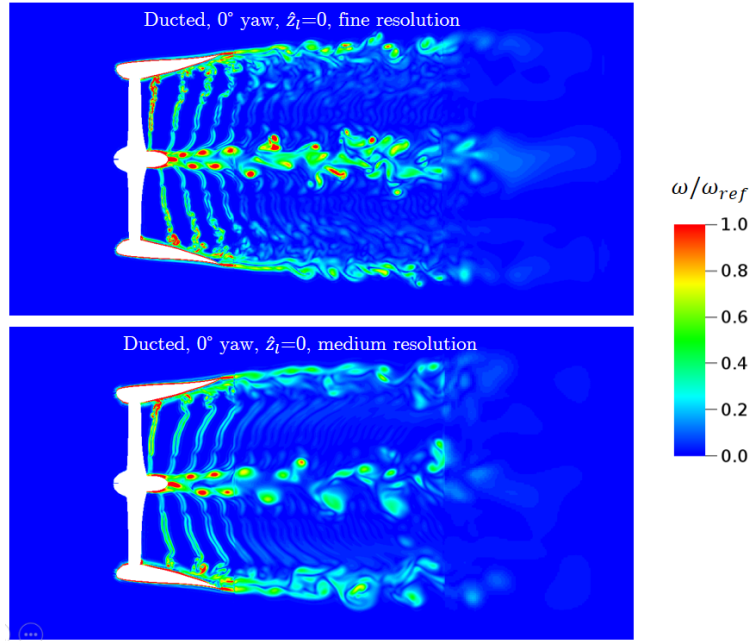


Figure 6.2: Vorticity magnitude snapshots on symmetry plane $\hat{z}_l = 0$ with fine (top) and medium grid resolution (bottom)

considered valid for meaningful results.

6.2. Acoustic convergence

The significant parameters to check the acoustic difference between various mesh resolution are chosen to be the Sound Power Level and the directivity, which are central in the results analysis. In fact, the PWL spectrum and the OASPL in different spatial locations permit to picture all the most important features of the flow, from the contribution of different sources at various frequencies to the noise pattern in space. Understand how these two characteristics change with the mesh refinement is therefore essential for the completeness of this study.

The ducted case without yaw is used as reference case. Only the last two grid refinement levels, i.e. the medium and fine resolutions, are shown in this analysis, in order to compare also the impact of fluid-dynamic differences, shown in the last paragraph. The solid FW-H formulation is preferred to the permeable counterpart to avoid the effect of different fluid-dynamic pattern on spurious noise sources which may appear in the permeable FW-H analogy. In Paragraph 8.1 this choice will be further discussed.

Figure 6.3 shows the PWL spectra obtained over six revolutions in the microphone locations described in Paragraph 5.4. The spectrum shows the power level density, expressed in dB/Hz , on a range from $4.755Hz$, which is the bandwidth and therefore the minimum frequency available, to approximately $5kHz$. After $5kHz$ which the noise becomes weaker and where the grid resolution and the time sampling rate do not allow capturing the waves. The pressure signal was then decomposed by using a bandwidth of $4.755Hz$, which corresponds to a quarter of the BPF. A Hamming window with automatically trimmed overlap was employed.

The Strouhal number based on the blade chord $St_l = \frac{fl}{U_\infty}$ is used to make the frequency axis non-dimensional. As a reference, values of St_l of 1, 10 and 50 correspond to frequencies of 47.6 Hz, 476 Hz, 2380 Hz, with the BPF located at $St_l = 0.4$.

It can be observed that quite some differences arise between the two, with the fine mesh resolution generally featuring a higher noise level. In the frequency range above $3kHz$, the higher PWL in the fine mesh resolution is likely to be caused by the inability of the medium mesh to capture

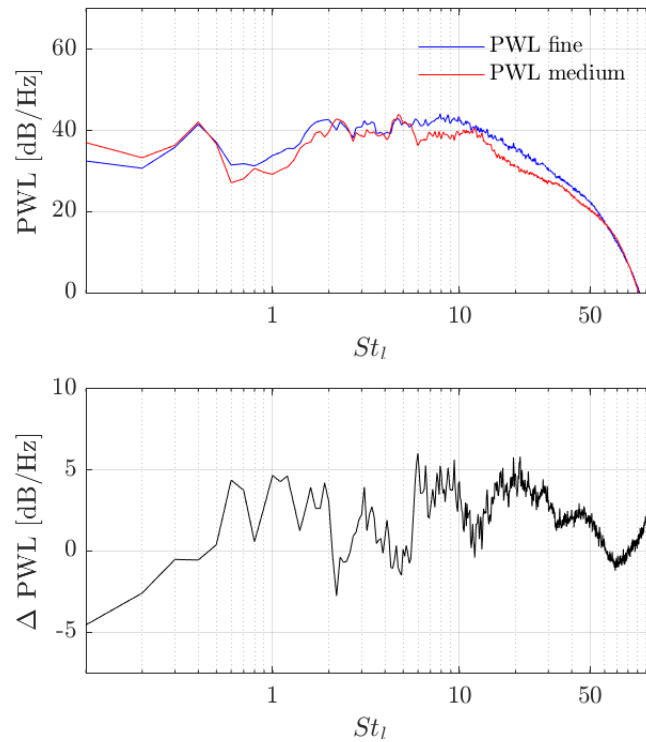


Figure 6.3: PWL for ducted turbine, 0° yaw, with medium (red) and fine (blue) grid resolution, in absolute value (top) and the difference fine - medium (bottom).

the specific frequency range, as discussed in 5.4. The remaining differences are probably due to the dissimilarities in the fluid behaviour rather than on direct effects on the sound waves. This hypothesis is reinforced by the fact that the observed increase in the rotor thrust would likely produce an enhancement in the power level. The presence of higher vorticity regions, both in the blade tip region and shed by the trailing edge of the diffuser, should be responsible for the high offset in the frequency range between 300Hz and 2kHz . The reason behind the 'difference peaks' in the low-frequency range is harder to understand and might be just due to the lack of data in the low frequencies part for the reduced amount of samples available.

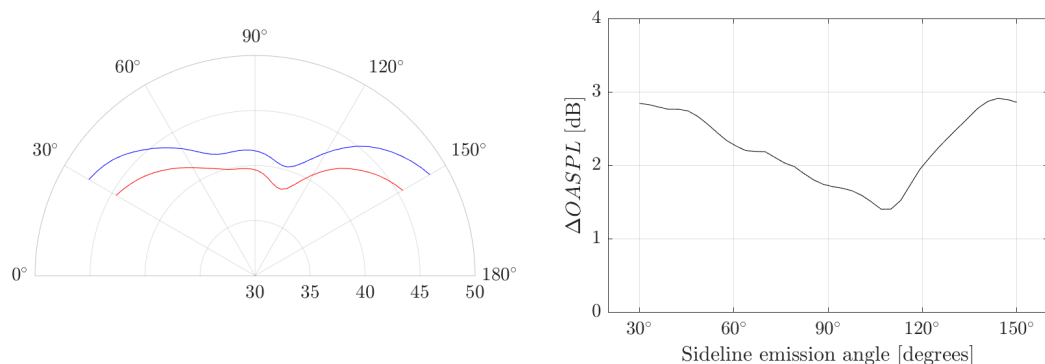


Figure 6.4: Directivity (wind coming from left side) for ducted turbine, 0° yaw, with medium (green) and fine (black) grid resolution, in absolute value (left) and the difference fine - medium (right)

In Figure 6.4 the same comparison for the directivity pattern is carried out. The noise pattern

is similar in the two cases, with an offset of $1.5 - 3\text{dB}$, with the fine resolution mesh case having a higher OASPL in all the microphones. The difference is higher at the two ends upwind and downwind. Since this is the region where the lobes are mainly connected to the blade trailing edge noise, this suggests a different boundary layer evolution in the two cases.

As mentioned in the previous paragraph, the available computational resources were not sufficient to perform finer simulations in due time. Therefore, except when stated otherwise, the fine grid refinement is used for obtaining the results in this manuscript in the ducted case and the medium refinement for the unducted case.

6.3. Diffuser pressure coefficient

This parameter has been used for model validation by the former two students working on the DonQi Windmill at TU Delft, ten Hoopen [58] and Van Dorst [61].

The comparison between the profile obtained from the current model in PowerFLOW and the results shown by the previous literature is shown in Figure 6.5. In order to allow a better comparability, the profile captured in PowerFLOW was acquired in a diffuser configuration without the zig-zag trip, with medium resolution scale. The data have been captured for the case without yaw on the pressure and suction side of a cross-section of the diffuser, as displayed in Figure 6.5. The rotor is located around the chordwise location of 0.2. The profile presented by ten Hoopen was obtained in an experimental session in the Open Jet Facilities of TU Delft. The sharper peak in his data just after the 0.2 location is due to a noise-dumper, not fully aligned with the diffuser surface, used during the experiments. The data by Van Dorst have been collected with a vorticity model adapted to the ducted turbine case. Given the uncertainties in the blade and diffuser geometries and the fact that the results by Van Dorst are obtained through a reduced order aerodynamic model, the comparison cannot be considered fully accurate.

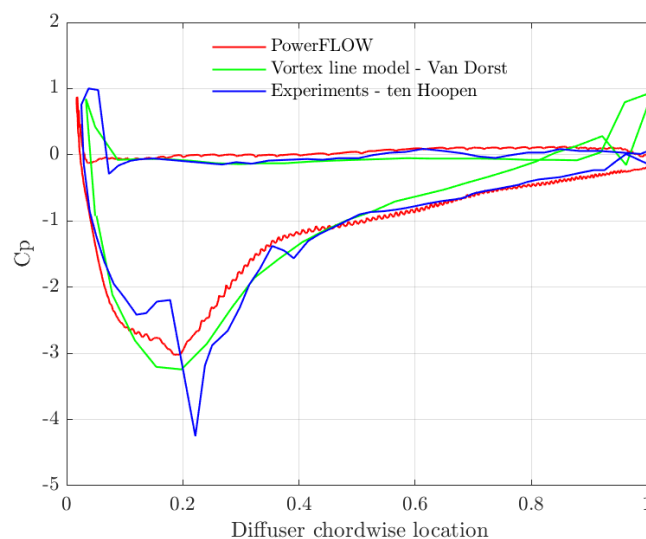


Figure 6.5: Pressure coefficient on diffuser in different research on DonQi Windmill. The data collected on PowerFLOW are shown in red, the experimental results from ten Hoopen in blue and the analytical model by Van Dorst in green.

However, from the figure, it can be noticed that the profile obtained with PowerFLOW generally resembles well the other two profiles. The main difference, besides the peak in ten Hoopen's results, is the values near the trailing edge, where the model by Van Dorst may suffer from numerical problems. It can also be seen that the values in the PowerFLOW case are slightly higher on the suction side and in the peak region, where the rotor is located, on the pressure side.

Results - Fluid-dynamics

The fluid-dynamics results are clustered into three parts, where the three study cases are compared according to different parameters. First, the forces and the power produced by the turbine are analysed. This includes both integral values and the thrust coefficient distribution along the blade. The second part regards the average field values, with the results collected in several significant planes. In particular, the axial velocity and the vorticity pattern are examined. In the third part, the snapshots of the field are examined, focusing on the vortices evolution in the domain.

7.1. Thrust and power

Results summary and data acquisition

Table 7.1 summarises the values obtained in the three different cases. These values were sampled after the time convergence was reached, as explained in 5.5.3.

	Ducted case, 0° yaw	Unducted case, 0° yaw	Ducted case, 7.5° yaw
T_r [N]	19.19	5.5	17.54
C_T [-]	0.704	0.202	0.644
Q [Nm]	2.49	0.46	2.22
P [W]	99.2	18.32	88.45
C_{Pr} [-]	0.728	0.134	0.649
$C_{P,diff}$ [-]	0.412	-	0.368

Table 7.1: Forces and power in the three cases

Power output

The theory on DAWT, explained in Paragraph 3.2.2, stated that C_p higher than the Betz limit of 0.59 can be exceeded only when referring to the diffuser area and not to the rotor area. By looking at the results of Table 7.1 relative to the ducted turbine, with no yaw angle, it can be noticed that this observation is also valid for the present case. The power coefficient relative to the rotor area amounts to 0.731 exceeds the Betz limit, while if it is referred to the diffuser area it is equal to 0.414, which is under the limit and it is a typical value for wind turbines.

Performance of ducted and unducted turbine

In Table 7.1 it can be noticed that there is a substantial difference in the power performance between the ducted and the unducted turbine. Looking at the cases without yaw, the power coefficient is 5.41 times higher in the diffuser augmented case when referring both to the rotor disk, and 3.07 times higher when referring the former to the diffuser area. These numbers represent a large difference, compared to common values in the literature.

The reason behind the issue can be discovered by comparing the values of the thrust coefficients along the blades in the two cases. Their plot can be observed in Figure 7.1.

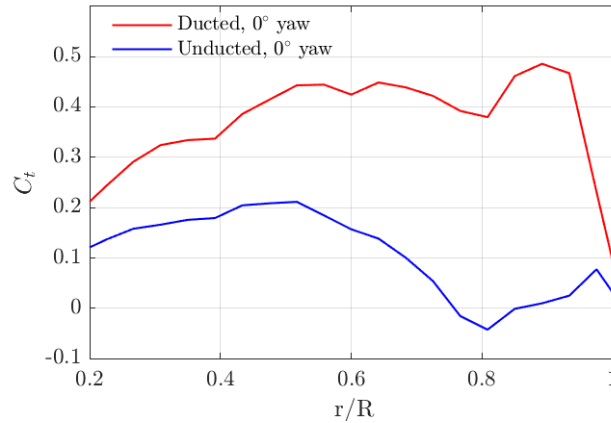


Figure 7.1: Thrust coefficient along the relative spanwise blade location for ducted turbine and unducted turbine

It is clear that that the rotor in the bare case produces almost no thrust in the outer part of the blade. Since both the thrust and the torque produced by the blade are directly related to the lift generated in that section, this means that a very low amount of power will be produced in that region. As mentioned before, the outer region of the blade is the most crucial for power harvesting, since the higher relative flow speeds are located there. Conversely, the thrust coefficient of the ducted turbine remains high over the whole blade span.

The reason why the unducted turbine behaves poorly in power harvesting is that is that the blade has been designed, in the work by Van Dorst [61], in order to maximise the performance when surrounded by a diffuser. Hence this specific design ends up not being effective in the unducted case, causing a significant difference between the two cases.

This also explains the difference between $C_{P, diff}$ in the ducted case and $C_{P, r}$ in the unducted case. According to the 1-D momentum theory by Van Bussel [59], the two values should correspond since they represent the energy extracted per unit volume. In practice, this does not happen since the 1-D theory does not account for the different designs of the blades.

Also, the thrust on the rotor is found to be higher in the ducted case, in agreement with the experimental results from Tang et al. [57] and in disagreement with the DAWT 1-D momentum theory.

In Paragraph 3.2.2 it was also stated that the power output of the turbine $P = T \frac{m}{A_r \rho}$ was augmented both by an increase of the mass flow across the rotor and of the rotor thrust. Indeed, referring to Table 7.1, the power has augmented by $\frac{P_{DAWT}}{P_{bare}} = 5.41$, the thrust by $\frac{T_{DAWT}}{T_{bare}} = 3.49$, which means that, being ρ and A_r constant, m has increased by 1.55.

Performance of yawed turbine

Referring to the theory on yaw on DAWTs shown in paragraph 3.2.3, the value of $\frac{L}{2R_{out}}$ for the DonQi Windmill is 0.5. With a yaw angle of 7.5° , the turbine should maintain its performance if a linear relationship between $\frac{L}{2R_{out}}$ and maximum unaffected angle is assumed. However, Table 7.1 shows

that this flow pattern leads to a lower thrust produced by the rotor (-8.5%) and to a lower power output (-10.8%). The local thrust coefficient is investigated in order to understand the reason for such a drop in the power production.

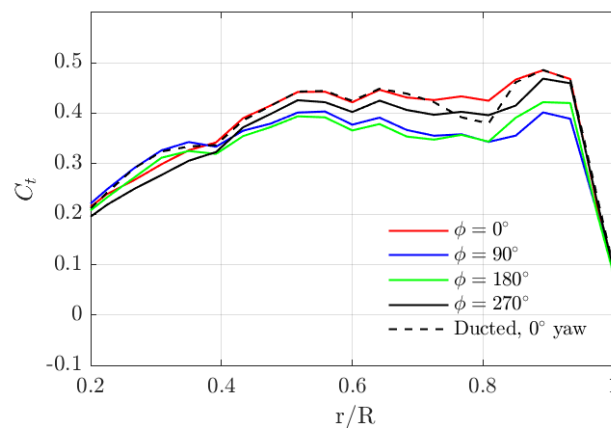


Figure 7.2: Thrust coefficient along the relative spanwise blade location for ducted turbine in yawed inflow for four azimuth angles, with non-yawed case dashed for comparison.

Figure 7.2 shows the local thrust coefficient along the blade span, measured on a single blade when it is located at four different azimuth angles as introduced in paragraph 5.2. Since the yawed inflow results in a non-axisymmetric flow at the rotor disk, the thrust on the blade varies during the revolution. The values of the local thrust coefficient are the lowest at $\phi = 90^\circ$. As the revolution continues, at $\phi = 180^\circ$ the values increase in the tip region, between r/R of 0.8 and 0.95. At the blade position of $\phi = 270^\circ$ C_t results higher for all the range above $r/R = 0.4$, and the same trend continues when the blade reaches $\phi = 360^\circ$. Interestingly, the trends are different near the hub, below $r/R = 0.4$.

The comparison with the turbine with non-yawed inflow reveals that the yawed case presents lower C_t for all the blade position except that for the $\phi = 360^\circ$ location, where it is actually higher for r/R between 0.7 and 0.82. It is therefore expected to find in the yawed case a region of velocity deficit around the location $\phi = 90^\circ$. This explains the lower thrust and power output observed in Table 7.1.

Another important finding is that at $r/R = 0.8$, near the blade tip, the difference between the higher and lower C_t amounts to 20%. However, the blades do not seem to stall, since C_t does not drop abruptly in any position. This means that no noise increase due to blade stall is forecasted in the yawed inflow case. This might change with higher inflow velocities and/or higher yaw angles.

7.2. Average field

The average flow field values allow having significant insights in the behaviour of diffuser augmented wind turbines. All the values have been obtained by averaging the field over three revolutions after the convergence has been reached. It is worth noting that, even though the first two cases are axisymmetric, the period of three revolutions is not sufficient to average out all the random transient fluctuations.

In the first paragraph, the flow values on the symmetry planes of the diffuser augmented turbine will be analysed; in the second, three planes perpendicular to the flow direction, placed at $\hat{x}_l = 0.1$, $\hat{x}_l = 0.35$ and $\hat{x}_l = 1.1$ (see paragraph 5.5.4) will be examined to understand more features of the flow field.

The axial velocity and the vorticity magnitude have been chosen to be shown as representative of the flow behaviour. The former clearly shows the fluid pattern and it is the most appropriate

property to explain the thrust and power generated by the blade, since it influences directly the angle of attack and therefore the lift coefficient on the blade airfoil sections. The latter allows depicting the vortical activity and it was found more suitable for 2-D figures than lambda-2 method.

The axial velocity is normalised with the free-stream value of $U_\infty = 5\text{ m/s}$, the vorticity with the reference value of $\omega_{ref} = 150\text{ s}^{-1}$.

7.2.1. Symmetry planes

Figure 7.3 shows the values of the axial velocity in the symmetry planes for the three cases. Since the first two cases have axisymmetric flow, only one plane is necessary to depict the flow pattern. In this case, the plane $\hat{z}_l = 0$ is chosen. In the yawed case, the two planes $\hat{y}_l = 0$ and $\hat{z}_l = 0$ are displayed.

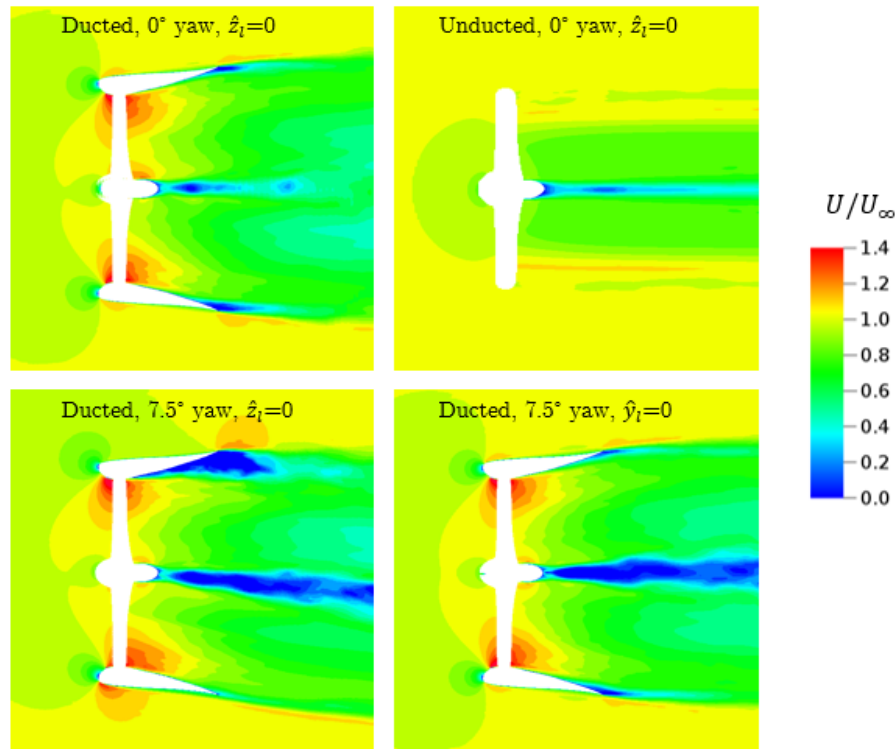


Figure 7.3: Axial velocity on symmetry planes. On the top, nominal conditions, ducted (A) and unducted (B). On the bottom, yawed conditions, planes $\hat{z}_l = 0$ (C) and $\hat{z}_l = 0$ (D)

Comparing Figures 7.3A and 7.3B a few significant elements can be noticed.

First, the presence of the diffuser clearly accelerates the flow at the tip region, up to $1.4U_\infty$. There, the local flow speed will be higher, leading to a higher angle of attack and therefore to higher lift produced by the blade. This in turn results in higher thrust and power produced from the rotor, as discussed in paragraph 7.1.

The second important difference is the radial size of the wake behind the diffuser, which is much larger in the ducted case. Since the wake is characterised by a velocity deficit compared to undisturbed flow, the green region after the turbine gives an immediate idea of the wake dimension. Characterising the wake as the region with a deficit of more than 10% of the undisturbed wind speed (approximately the green region), at $\hat{x}_l = 1.5$ it will show a diameter of with a 1.05 m in the unducted case and of 2.16 m in the ducted case. This agrees with the 1-D DAWT theory, that states that the wake diameter will be higher when the axial loading on the rotor disk is higher, as long as $C_T < 8/9$ as in this case.

The third important finding is the behaviour of the turbine in yawed condition compared to flow parallel to the turbine axis. As can be seen in Figure 7.3C a separation zone takes place from

a location of approximately 25% of the diffuser chord, due to the impact of the yaw angle, in disagreement with the results from Cresswell et al. [15]. On the other side of the diffuser, the small separation region that was present in the non-yawed case disappears, making the wake highly non-axisymmetric. Such separation region does not seem to affect the velocity pattern at the rotor plane, thus it is not expected to be responsible for the power drop in the yawed case.

Finally, comparing Figure 7.3A and 7.3C it is visible that yaw has the effect in the lower half to move the stagnation point towards the inner side of the diffuser, pushing the flow acceleration region to further in the diffuser. This results in a variation of the flow field at the rotor plane, which can explain the C_t behaviour shown in paragraph 7.1.

7.2.2. Axial planes

The flow patterns in three planes perpendicular to the rotor axis, so perpendicular to the free stream wind direction only in the non-yawed cases, are shown in this section for all the three cases. These planes are located at placed at $\hat{x}_l = 0.1$, $\hat{x}_l = 0.35$ and $\hat{x}_l = 1.1$, as explained in paragraph 5.5.4. The planes are shown as if looking downwind.

Figure 7.4 shows the axial velocity of the flow before encountering the rotor. Comparing Figure 7.4A and 7.4B, it is clear to see that the addition of a diffuser results in a pattern with local velocity that increases while from the centre to the diffuser wall from U_∞ to $1.4U_\infty$. The yaw brings to a non-symmetric velocity field on the left side of the diffuser, coherently to what observed in paragraph 7.1.

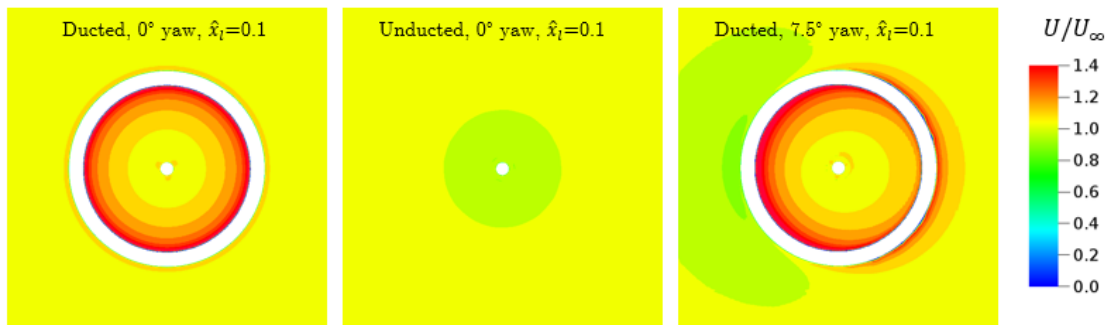


Figure 7.4: Axial velocity on plane $\hat{x}_l = 0.1$. Left (7.4A): ducted, 0° yaw. Center (7.4B): unducted, 0° yaw. Right (7.4C): ducted, 7.5° yaw

For what concerns the vortices, at $\hat{x}_l = 0.1$ the only visible vortical phenomena are at the solid boundaries of the diffuser, as can be observed in Figure 7.5.

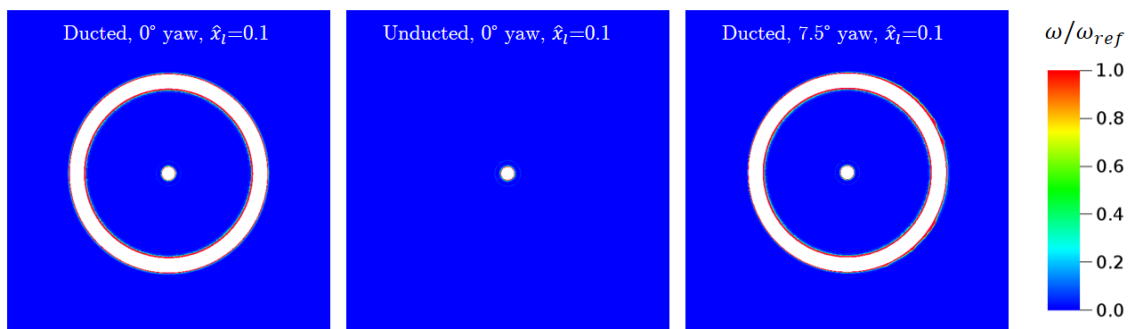


Figure 7.5: Vorticity magnitude on plane $\hat{x}_l = 0.1$. Left (7.5A): ducted, 0° yaw. Center (7.5B): unducted, 0° yaw. Right (7.5C): ducted, 7.5° yaw

In Figure 7.6, on plane $\hat{x}_l = 0.35$, the flow has passed the blades. In the ducted case with 0° yaw, Figure 7.6A, it can be seen that the flow has been slowed down by the rotor disk. In the case with yaw, the non-symmetric pattern of the flow has now shifted to the right side of the diffuser.

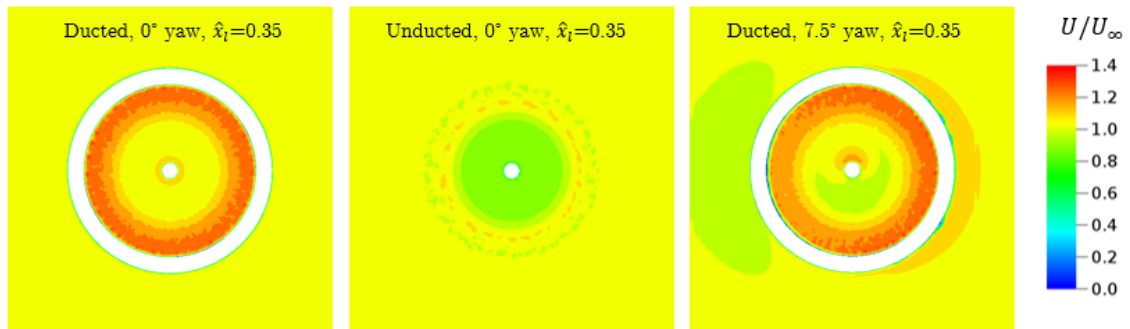


Figure 7.6: Axial velocity on plane $\hat{x}_l = 0.35$. Left (A): ducted, 0° yaw. Center (B): unducted, 0° yaw. Right (C): ducted, 7.5° yaw

In Figure 7.7 it can be seen that, downstream of the rotor, there is a high vortical activity in the tip region of the ducted cases. No significant difference can be spotted between 0° and 7.5° yaw angles. In the same location in the unducted counterpart, the flow has almost come back to undisturbed condition. The hypothesis according to which the installation of a diffuser would have reduced the vortical activity in the tip region seems confuted.

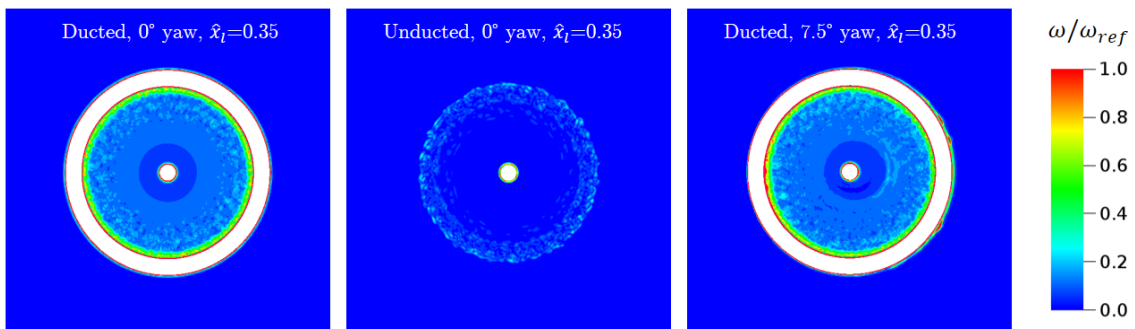


Figure 7.7: Vorticity magnitude on plane $\hat{x}_l = 0.35$. Left (A): ducted, 0° yaw. Center (B): unducted, 0° yaw. Right (C): ducted, 7.5° yaw

Figure 7.8 shows the axial velocity of the flow after the exit from the diffuser. As mentioned before, the wake is significantly larger in the ducted case. In Figure 7.8A, a 'ring' with almost still flow in the direction of the rotor axis is present. Correspondently, in Figure 7.9A, a region with high vorticity is present.

The separation region at the end of the diffuser in the yawed case is well visible in Figure 7.8C. On the other end, the still flow region is thinner, suggesting lower vortical activity.

The consideration still holds downstream of the diffuser, as can be noticed in Figure 7.9. In the ducted case, the vortices have conserved their magnitude, while they have weakened in the unducted case, in disagreement with the results from Takahashi et al. [56]. As could have been foreseen, the yawed case presents non-symmetric vorticity regions, correspondent to the strong velocity deficit shown in Figure 7.9C.

It emerges that an analysis of the structure of the vortices through instantaneous values is needed.

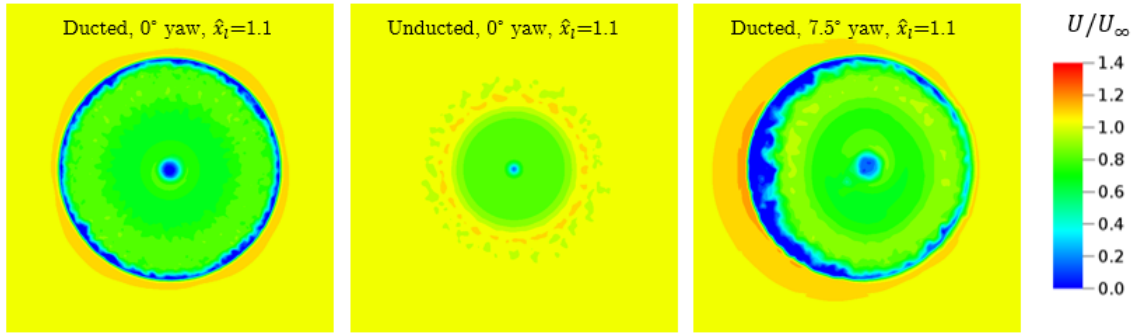


Figure 7.8: Axial velocity on plane $\hat{x}_l = 1.1$. Left (A): ducted, 0° yaw. Center (B): unducted, 0° yaw. Right (C): ducted, 7.5° yaw

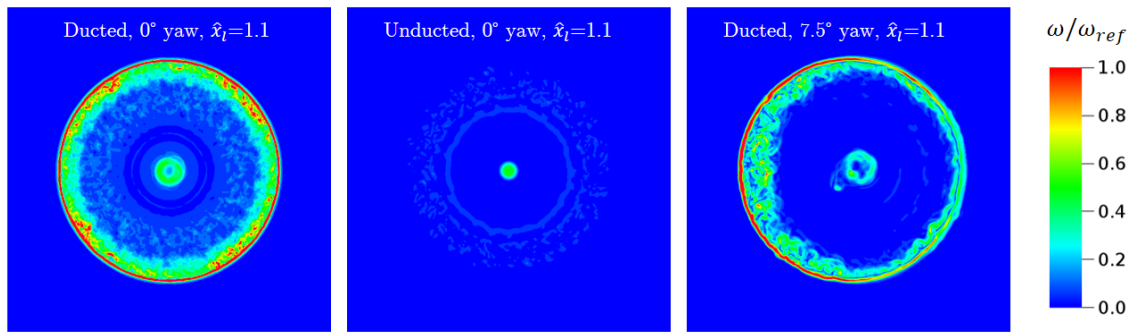


Figure 7.9: Vorticity magnitude on plane $\hat{x}_l = 1.1$. Left (A): ducted, 0° yaw. Center (B): unducted, 0° yaw. Right (C): ducted, 7.5° yaw

7.3. Instantaneous field

In order to gain more insights into the flow behaviour, some snapshots are hereafter analysed. First of all, the vorticity magnitude is presented for the same symmetry planes described in paragraph 7.2. Afterwards, the vortices detected with lambda-2 method are shown. Since it was not possible to perform a phase-locked analysis for the lambda-2 method, snapshots are employed for the sake of comparability.

Figure 7.10 and Figure 7.11 shows the vorticity magnitude for the three cases. A longer section than in the average field is shown in order to check the evolution of the vortices in the wake.

The first thing to be noticed is that, in all the cases, vortices are shed from the blades with a frequency correspondent to the BPF, equal to $BPF = B\Omega = 19.02 Hz$, with B number of blades of the turbine and Ω rotational speed of the rotor. These vortices decrease their magnitude while going downstream.

In the baseline ducted case, Figure 7.10A, the tip vortices move towards the inner part of the diffuser creating a unique vortical region with the boundary layer as they are convected downstream. A zone of intense vorticity is present for more than $2L$ downstream, which is not the case in the unducted case, Figure 7.10B. Such a vorticity area may prevent the flow in the wake from mixing with the undisturbed flow. This might constitute a drawback for possible application of more DAWT in series, since a longer distance between turbines would be required to let the velocity deficit be overcome. Unfortunately, the strong dependence of the vortices coherence from the resolution while moving downstream in the current case does not allow drawing definitive conclusions about the phenomenon.

The ensemble hub-nacelle seems to act as a blunt body, creating downstream a flow region that presents the typical pattern of a Von Karman street.

Finally, it has to be pointed out that the behaviour of the vortices is influenced by the mesh res-

olution. Especially in the ducted cases, it is well visible the step between different VR regions. After the second VR variations, the resolution is too low to capture the vortices, which quickly disappear going downstream. This is not expected to have a significant impact on the acoustic results, given the local low speed of the flow.

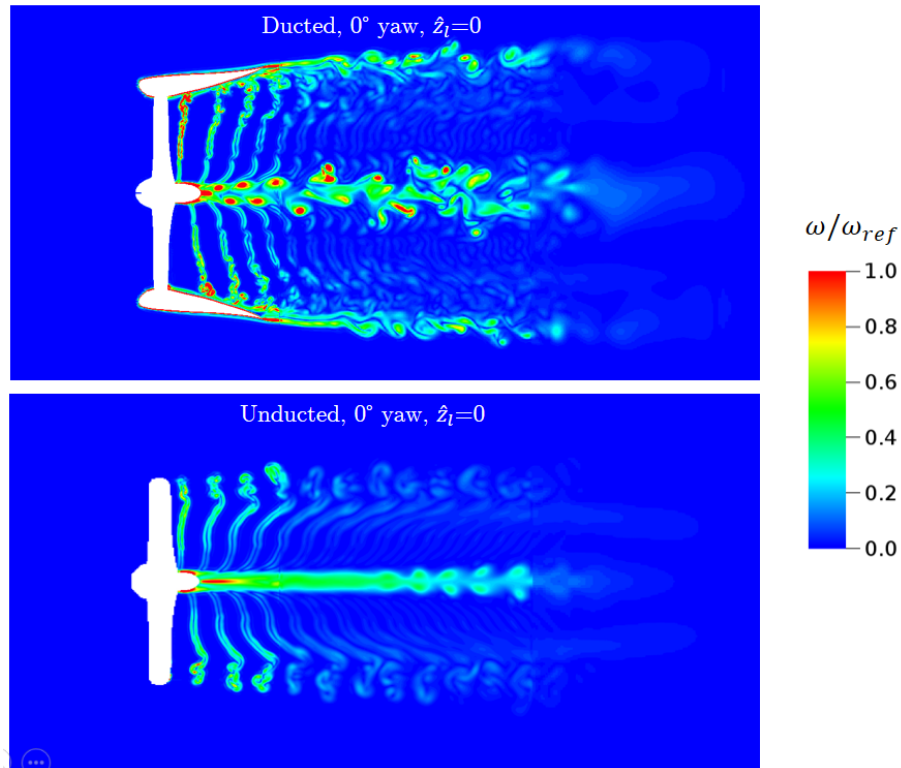


Figure 7.10: Vorticity snapshots on symmetry plane $\hat{z}_l = 0$ for baseline conditions, ducted (A) and unducted (B)

Figure 7.12 shows the vortices in the cases without yaw, detected with lambda-2 method. It is shown a box, ranging from $\hat{y}_l = -0.25$ to $\hat{y}_l = 0.25$, with the vortices coloured according to their velocity magnitude V . Such parameter is useful to understand the expected noise contribution of the vortical structures. All the following pictures have been obtained with the medium grid refinement, given the unavailability of instantaneous flow field data in the entire simulation volume the finer resolution scale.

From Figure 7.12A, it is possible to see that the vortices shed in the tip region are characterised by a small length scale and high velocity magnitude, equal up to $1.4U_\infty$. Therefore, they are expected to represent a relevant noise source, in the high frequency region.

While going downstream, the vortices shed by the rest of the blade quickly disappear. The vortices in the tip region become coherent and longer in the streamwise direction, but they do not seem to merge with the diffuser boundary layer. Indeed, the groups of structures create an almost continuous zone of vorticity that follows the shape of the diffuser suction side. After the outlet of the diffuser, the tip vortices encounter the structures shed by the diffuser trailing edge, resulting in long coherent structures which are convected in the wake.

The vortices scattered from the trailing edge of the diffuser are characterised by a low wind speed, around $0.6U_\infty$ on the suction side and $0.2U_\infty$ on the pressure side.

In Figure 7.12B it can be noticed that the vortices shed by the blade have a similar pattern, with only the tip vortices not disappearing after a short distance downstream. However, the velocity that characterises that vortices is not higher than U_∞ . A lower high frequency noise is therefore expected in the unducted case.

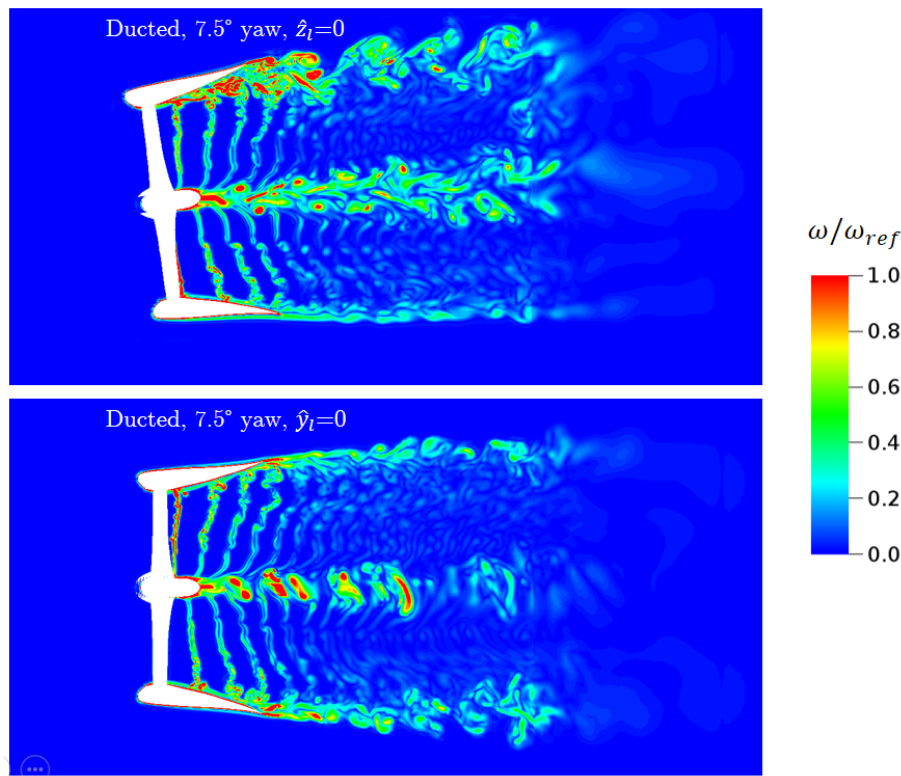


Figure 7.11: Vorticity snapshots on symmetry plane $\hat{z}_l = 0$ (C) and $\hat{y}_l = 0$ (D) for yawed conditions

It should be pointed out that, conversely to the ducted case, the tip vortices remain in clearly separated groups, which disappear after a length of around $1L$ downstream, where VR6 ends.

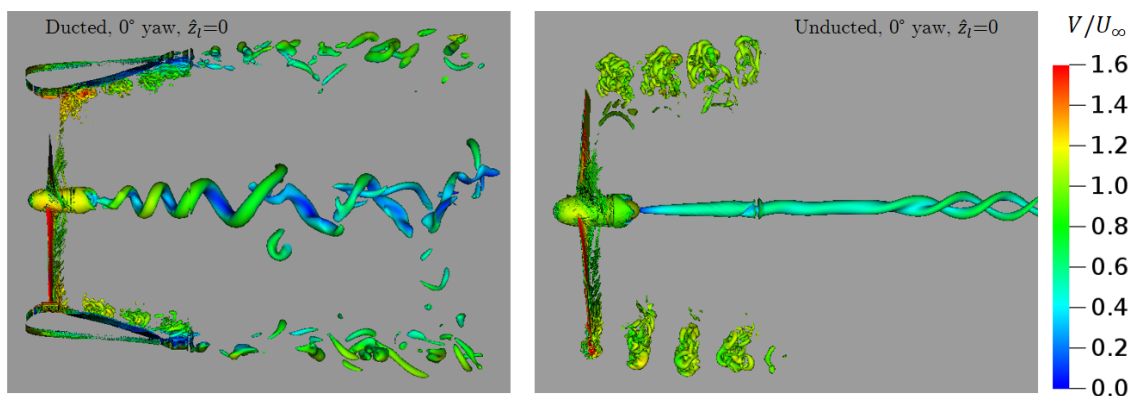


Figure 7.12: Lambda-2 vortices coloured with velocity magnitude for baseline conditions, ducted (A) and unducted (B).

Figure 7.13 shows the analogous results by comparing the ducted cases with and without yaw angle. The latter (B) shows several elements of interest. On the top half, the separation region results in high vortical activity with low flow speed, less than $0.2U_\infty$, which is therefore not expected to contribute significantly to the noise field. The tip vortices accumulate around the separation region, creating a continuous vortical zone which merges downstream with the vortices shed from the diffuser trailing edge. After the diffuser outlet, this region is much broader than in baseline conditions. The opposite behaviour appears in the lower half, where the diffuser cross-section is almost aligned with the flow. Downstream of the outlet, no vortices are detected.

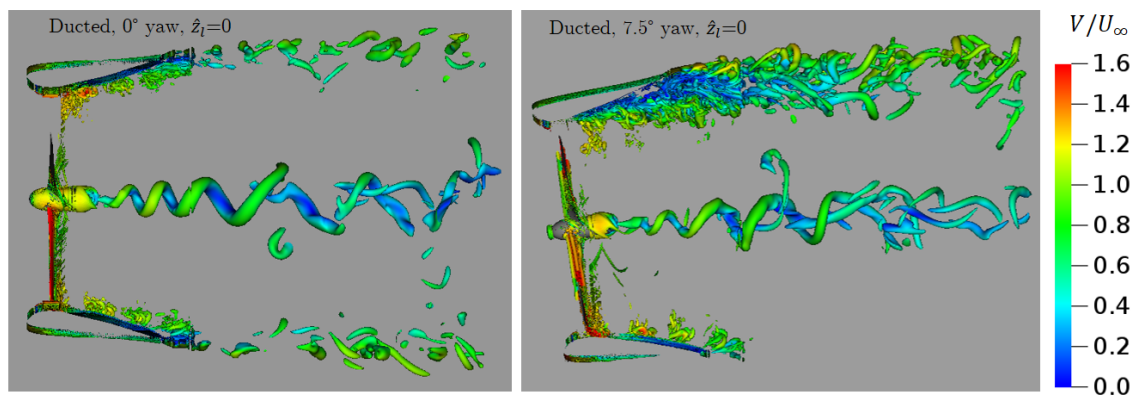
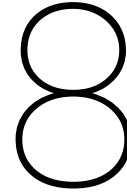


Figure 7.13: Lambda-2 vortices coloured with velocity magnitude on symmetry plane $\hat{z}_l = 0$ for baseline (A) and yawed (B) conditions



Results - Acoustics

This Chapter deals with the acoustic results obtained in three case studies.

In the first part, the Sound Power Level spectra are presented. This part includes the comparison between permeable and solid FW-H formulation and the reasons behind using the latter as a benchmark. The second part shows the results of the directivity analysis, with the OASPL values collected for different microphone locations. Finally, a circumferential and duct mode analysis is carried out in order to have an insight on further acoustic phenomena.

8.1. Sound Power Level Spectrum

8.1.1. Comparison between FW-H solid and FW-H permeable

As explained in the previous paragraphs, the acoustic results are computed both FW-H solid and FW-H permeable formulation.

In order to compare their performance, the case with ducted turbine and no yaw, at the higher resolution available, is used as a benchmark. The PWL spectrum can be seen in Figure 8.1. The spectrum shows the power level density, expressed in Db/Hz , on a range from $4.755Hz$, which is the bandwidth and therefore the minimum frequency available, to approximately $5kHz$, after which the noise becomes weaker and where the grid resolution and the time sampling rate do not allow capturing the waves. The data were collected during the same period, correspondent to six revolutions of the rotor. The pressure signal was then decomposed by using a bandwidth of $4.755Hz$, which corresponds to a quarter of the BPF. A Hamming window with automatically trimmed overlap was employed. The Strouhal number relative to the chord is employed for the graph, as explained in Section 6.2.

It can be noticed that the two curves generally agree well, which is an indicator of correct setup.

However, there are two regions where the noise pattern behaves differently. The first is the BPF at $St_l = 0.4$, where the permeable formulation underestimates the peak. The second is the region above $St_l = 50$, where unexpectedly the solid formulation presents lower PWL. Usually, differences between the two can arise due to the spurious noise sources described in Paragraph 4.2.1, i.e. vortical disturbances passing over the downwind face of the FW-H permeable surface and to lack of resolution to describe the vortical structures. While this might explain the difference at the BPF, the mechanism behind the second difference remain not clear.

Given these premises, it is chosen to use the solid FW-H formulation for comparing the next results: given the negligible contribution of quadrupoles in the current setup, avoiding spurious noise sources and vortical disturbances in the FW-H permeable surface is considered more important.

8.1.2. PWL spectrum in the three cases

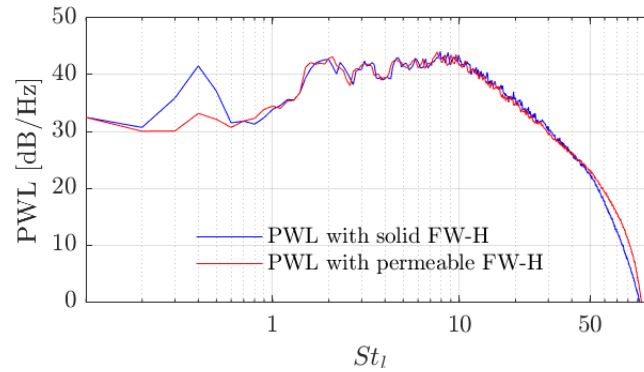


Figure 8.1: PWL for ducted turbine, 0° yaw, for permeable (blue) and solid (red) integration for FW-H analogy

Ducted case, no yaw

Before starting the comparison between the different cases, it is useful to take a closer look at the PWL spectrum for the ducted case without yaw. The spectrum is shown again in Figure 8.2, this time only for the solid FW-H methodology, in the whole frequency range and in the first harmonics of the Blade Passing Frequency.

It can be noticed that the noise has broadband characteristics for all the frequencies, with no tones emerging. The only exception is the peak at the BPF at $St_l = 0.4$. The peak, typical of all rotating structures, is due to the phenomenon of convective amplification which was discussed in 2.2.6: each microphone perceives a higher noise when the blade is approaching, which happens with a frequency correspondent to the BPF.

It should be pointed out that the characteristics of the spectrum around the BPF might be slightly inaccurate, since in this range the frequencies captured are very low and the sampling time was only of six revolutions. However, it should be reminded that the audible range of frequencies from human ear starts from approximately 20Hz , i.e. $St_l = 0.41$: the BPF is therefore not of great interest for what concerns the usage of the turbine. In Figure 8.2 it can also be noticed that only the BPF has a clear peak, while the next harmonics do not appear in the spectrum, probably covered by the broadband noise.

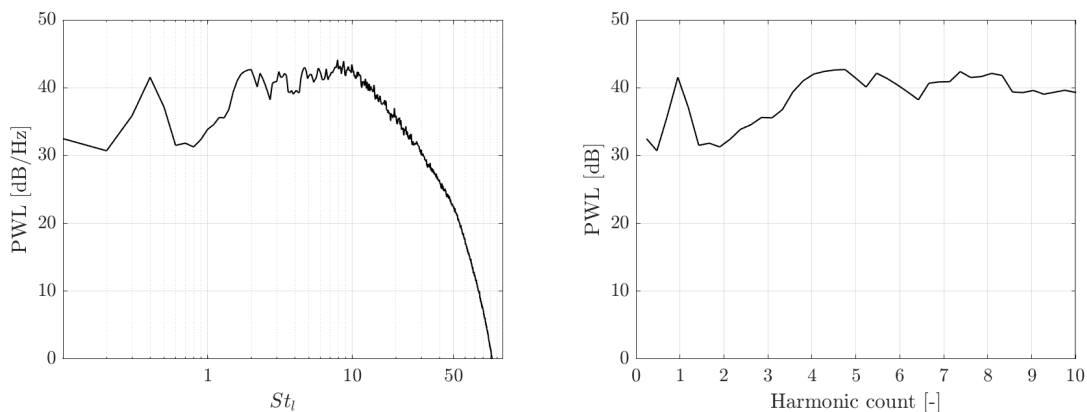


Figure 8.2: PWL for ducted turbine, 0° yaw, over the complete frequency range (left) and in the first ten harmonics of the BPF

Ducted vs unducted cases

The two cases without yaw, i.e. the ducted and unducted turbine, can then be compared by using the solid FW-H analogy. Figure 8.3 shows the PWL for the two cases, with the plot of the difference

between the two curves. As it was expected from the fluid-dynamic analysis, it is clear that the ducted turbine is significantly noisier than its unducted counterpart.

The low frequencies range, until $St_l = 1$ shows a similar fashion, but with an almost uniform difference of 6 dB, which is slightly higher at the BPF. Such difference is likely to be due to the higher wind speeds that the ducted turbine experience over its revolution, producing higher noise.

The larger discrepancy between the two turbines is in the highest frequency span, above $St_l = 20$. This is the frequency span which is proper of tip vortices, which as described earlier, in contrast with other authors, have a higher magnitude in the case with diffuser, even after the end of the diffuser.

The rest of the difference is probably caused by the higher trailing-edge noise in the ducted case, both the one in the blades which experience higher velocities and the one shed by the trailing edge of the diffuser.

The peaks that appear in the PWL spectrum of the unducted case are likely to be caused by the low sampling time, which might not be sufficient to obtain a complete statistic.

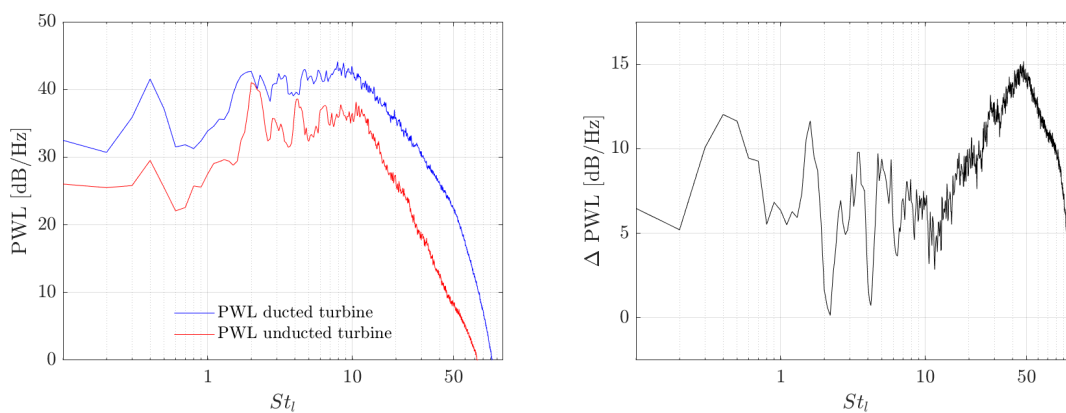


Figure 8.3: PWL for ducted turbine, 0° yaw (blue), and unducted turbine, 0° yaw (red), in absolute value (left) and their difference (right)

Nominal vs yawed conditions

The last comparison that should be examined is between the ducted cases with 0° and 7.5° yaw, shown in Figure 8.4.

It can be noticed that the two spectra show a similar behaviour for a large part of the spectrum. A significant difference is however found in the low frequency range, where the yawed turbine is more noisy. This can be explained with the fact that the main difference between the two fluid patterns is the separation region present in the yawed case. Such noise is typically associated with low frequency noise, given the large size of the turbulent eddies.

The differences in the rest of the spectrum, for frequencies higher than $St_l = 1$, are likely to be done to random effects not averaged by the small amount of revolutions used for collecting these data.

The fact that the presence of a separation region does not result in a larger noise enhancement might seem an odd results, since for blade stall and separation in a regular turbine overall noise increase of 10 dB and more have been registered [46]. However, it should be remembered that, since separation can be approximated as a compact dipole noise source, its power level scales with M^6 . As anticipated in Section 7.3, the separation region is located in an area with low flow velocities, less than $5m/s$, while the flow speed in the blade tip region, where separation usually has the possibility to take place, amounts in the present case to around $30m/s$. Together with the reduced area of

the separation region, this explains how its contribution to the overall sound spectrum is actually relevant only at low frequencies and basically negligible for human auditory system.

Furthermore, effects related to the unsteady loading on the blades connected to lack of symmetry on the rotor plane, as cyclic variation of trailing edge and tip noise, are not expected to be relevant as long as the blade does not stall [46].

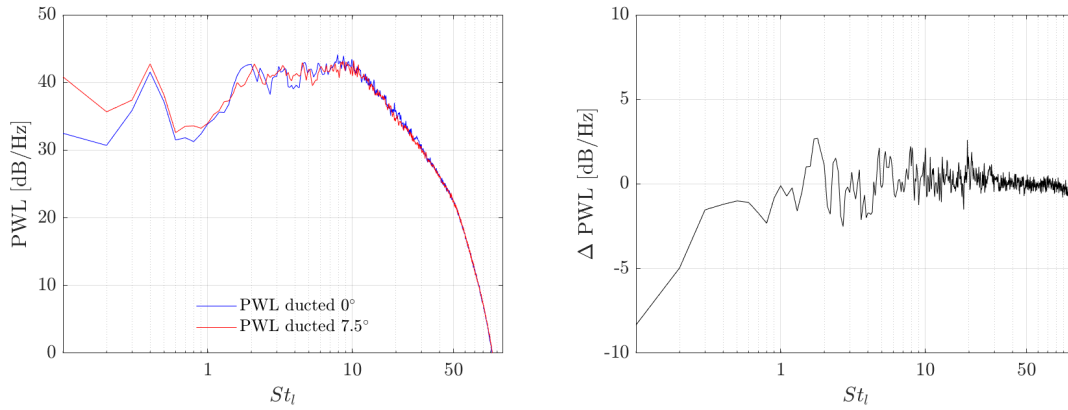


Figure 8.4: PWL for ducted turbine, 0° yaw (blue), and ducted turbine, 7.5° yaw (red), in absolute value (left) and their difference (right)

8.2. Overall sound pressure level and directivity

Unducted case

By analysing the overall sound pressure level in each microphone along the arch, it is possible to characterise the directivity of the noise in the area around the turbine. As in the PWL analysis, a glance at a specific case, this time the simple unducted turbine, is useful to understand some basic features of these plots.

By looking at Figure 8.5, the pattern shows a zone of silence, with a 'cone' shape, above the rotor between 70° and 115° , and two zones of noise upwind and downwind. This is a typical noise pattern for a wind turbine, which is indeed almost silent just below and above the blades and loud in the other regions. This results in lobes shape, here not completely shown because of the current microphones location.

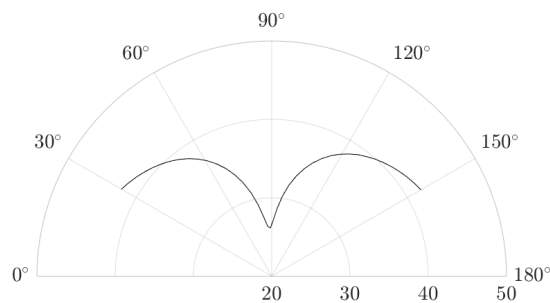


Figure 8.5: Directivity in the unducted case, with OASPL [dB] for different sideline emission angles [degrees]. Wind is coming from the left side.

The reason behind this pattern can be found by considering that the prevalent wind energy noise is the trailing edge noise, which exhibits characteristics of dipole source. Since the case is axisymmetric, it is not possible to spot the directivity towards the leading edge which is proper of trailing edge noise.

Ducted vs unducted case

The directivity in the ducted and unducted case can be found in Figure 8.6. It is immediate, as expected, to notice the higher OASPL over all the azimuthal locations.

The most significant result is that the zone of silence above the turbine has almost disappeared. The diffuser is indeed not acting as a 'shield', but contributes to the noise pattern.

At first, this might be ascribed to the diffuser trailing edge. However, as shown in Section 7.3, the low flow speed at the trailing edge location suggests that this is not the driving mechanism, even though the directivity has its peak towards the leading edge, as typical of trailing edge noise. Probably, the scattering of the acoustic waves on the diffuser walls is the responsible for the significant sound increase above the rotor. The location of the rotor and the different diameter between diffuser inlet and diffuser outlet would explain the non-symmetric noise pattern along the arch.

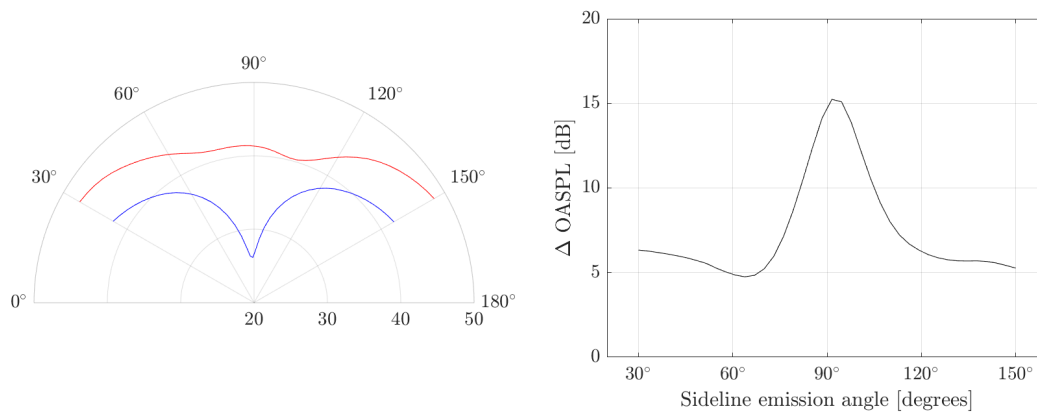


Figure 8.6: Directivity for ducted turbine, 0° yaw (blue), and unducted turbine, 0° yaw (red), in absolute OASPL [dB] (left) and the difference ducted - unducted (right)

Nominal vs yawed conditions

A comparison between the radiation of the yawed and non-yawed case is shown in Figure 8.7. Both the planes $\hat{y}_l = 0$ and $\hat{z}_l = 0$ are displayed for the lack of axisymmetry of the yawed model.

Looking at the X-Y plane, with the presence of a yaw angle there seems to be an increase of the SPL in the downstream part of the upper arch and in the upstream part of the lower arch, with opposite behaviour in the opposite regions. Such a difference cannot be explained with any noise generation mechanism and appears to be purely geometrical. With the yawed configuration, the directivity is actually tilted on the X-Y plane where the yaw angle is defined. This is easily explained, since all the surfaces responsible for noise generation are tilted as well.

In line with the results on the PWL spectrum, the tilt in the directivity does not seem to affect largely the overall difference in the sound level. Indeed, in the X-Z plane the patterns for the situations with and without yaw are almost identical.

This results would confirm, as stated in Paragraph 8.2, that the driver for the directivity pattern is the influence shape of the diffuser on the noise produced by the blades rather than the noise generated by the diffuser itself. Indeed, the non-axisymmetric pattern of the vortices shed by the diffuser shown in Section 7.3 does not seem to impact the OASPL distribution.

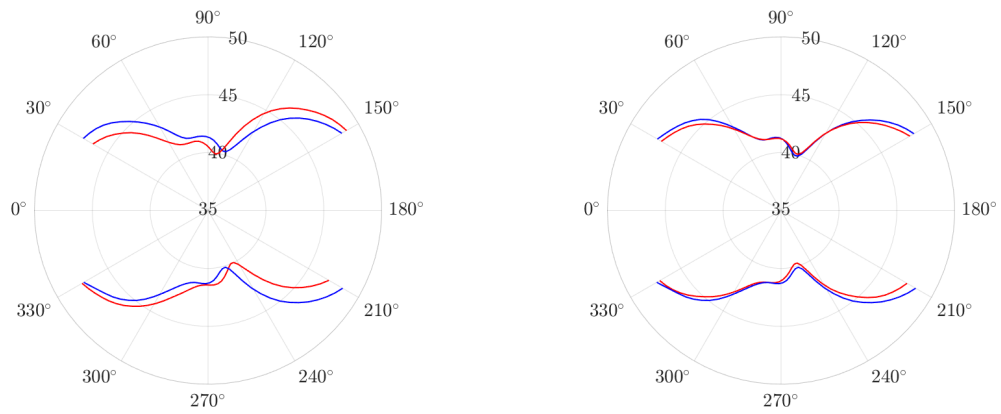


Figure 8.7: Directivity for ducted turbine, 0° yaw (dashed blue), and unducted turbine, 0° yaw (red), in absolute OASPL [dB] on $\hat{z}_l = 0$ (left) and $\hat{y}_l = 0$ (right)

8.3. Circumferential Fourier modes and duct modes analysis

The analysis is performed on the azimuthal modes m from -20 to 20. The solution is extracted on the plane $\hat{x}_l = 0.35$ (see Paragraph 5.5.4) just downstream of the rotor disk. The pressure variations have been collected on these planes for six revolutions, with a sampling frequency of approximately $10kHz$.

The circumferential Fourier modes have been calculated with a constant bandwidth of $4.755Hz$, equal to a quarter of the BPF, for a frequency range from $4.755Hz$ to $5002.26Hz$. Hamming window coefficient has been used, with automatic optimal refinement for the overlap coefficient. The numerical solution is projected on a uniform polar grid composed of 60 points in the azimuthal direction and 20 in the radial direction.

Duct modes are computed as well on the plane $\hat{x}_l = 0.35$, with only cut-on modes employed. Five radial modes are used in the basis. These modes are calculated using the integral average Mach number as axial Mach number. As mentioned before, the section is not ideal compared to the case of an infinite straight duct.

The circumferential Fourier modes decomposition for the ducted case without yaw at a frequency correspondent to the BPF is shown in Figure 8.8.

The graph for the 0° yaw case shows a peak in the mode $m = 1 * B = 3$, which is the rotor locked-in mode. The other peaks appear with jumps of $3 * m$ for both negative and positive values, with typical decreasing V-shape around the peak.

However, the duct mode analysis conducted in the section inside the duct reveals that around the BPF only the plane wave, i.e. the mode $m = 0$, is actually cut-on. Having a cut-on plane mode contrasts with the duct modes theory. The other modes are all cut-off, including the rotor locked-in mode $m = 3$.

This means that the peaks observed in the graph are not related to the rotation of the blades itself, but to the periodic phenomena related to turbulence and to vortices shed from the blade, as pointed out in Paragraph 2.4.

A modal scattering mechanism can be observed, with higher SPL levels than expected in modes as $m = -1$ or $m = 7$, probably related to reflection on the solid surfaces [11]. The modes with lower contributions to the SPL are likely connected to the short sampling time of the analysis, which means that the averaging cannot eliminate the contribution of random modes.

For what concerns the 7.5° yaw angle results, the only peak appearing is the mode $m = 3$, with modal scattering around it. The reason why the other $3m$ peaks do not appear is supposed to be connected to the interaction of the blade rotation with the non-axisymmetric flow at the rotor plane. The flow at the rotor plane is non-uniform with a periodicity of 2π , resulting in modes $m \pm n$, with

$n \in \mathbb{N}$.

It is also interesting to notice that the SPL is higher for positive modes, as a consequence of the swirl in the flow.

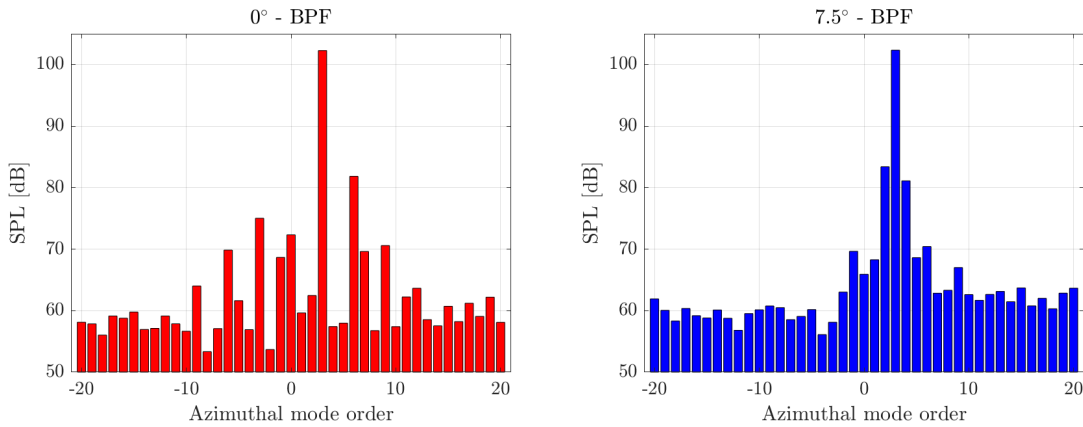


Figure 8.8: Circumferential Fourier modes around the BPF for the 0° (left) and 7.5° (right) yaw angle cases

Figure 8.9 shows the same graph, with the same normalisation, around the frequency of 38.02 Hz, the double of the BPF. Similar considerations apply, with the main difference that the peak is now located at $m = 2 * B = 6$. Also in this case, the only cut-on mode is the mode $m = 0$, which is not indeed not following the same trend of the other modes in the yawed case.

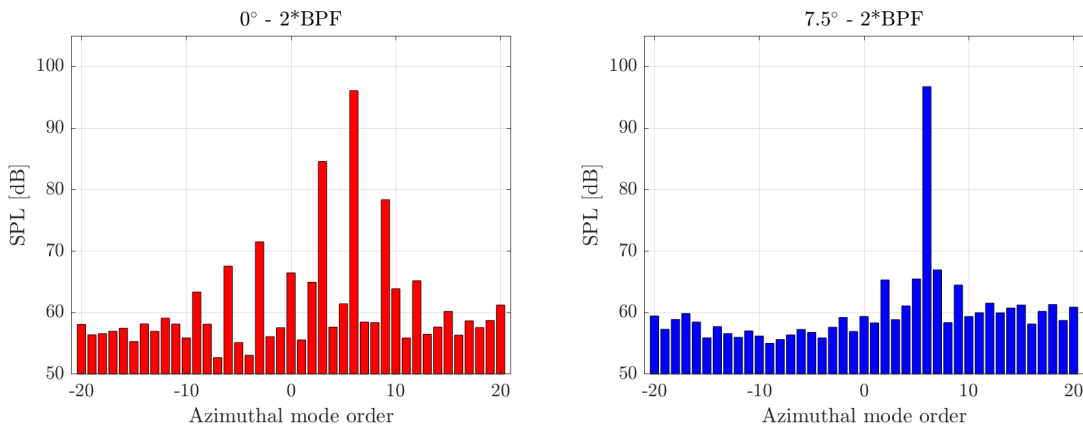


Figure 8.9: Circumferential Fourier modes around 2 BPF for the 0° (left) and 7.5° (right) yaw angle cases

9

Conclusions and recommendations

9.1. Conclusions

At the end of the work, several conclusions can be drawn from the computational analysis regarding the characteristics of the DonQi Windmill. The conclusions are grouped according to the research goals stated in the beginning: in this section, the reader will realise how these goals have been accomplished and what are the main findings about each topic.

- *Create a baseline setup*

As the first step, a geometry has been created as CAD model. All the main features of the real DonQi Windmill have been represented, with the addition of zigzag trips on blade and diffuser that are crucial to characterise the flow correctly. Furthermore, the geometry implementation in SolidWorks is flexible and easy to modify, which leaves space for changing any parameter for further study.

The rest of the setup is then created on Exa PowerCASE. The lattice is divided into nine Variable Resolution regions that tailor the mesh refinement according to the flow characterisation. These regions are related to the voxel size, which makes almost automatic to change the whole grid refinement.

All geometry, lattice definition, acoustic setup and simulations settings are then validated by a comparison with previous results on the DonQi turbine, both analytical and experimental.

The whole setup is therefore validated and flexible for further use in upcoming research.

- *Analyse the fluid-dynamic flow field in nominal conditions*

The power coefficient of the turbine is found to exceed the Betz limit when referring to the rotor area but not when referring to the diffuser area, in agreement with the research by Lubitz and Shomer [39]. The power augmentation of the diffuser augmented turbine compared to the bare counterpart is found to amount to several units, due to the blade design which is optimised for ducted conditions.

For what concerns the flow field, a significant finding regard the tip vortices, on which different researchers have stated opposite opinions. In agreement with the higher wind speeds in the tip region, they are found to have a larger magnitude in the ducted case. As they are convected downstream, they interact with the diffuser boundary layer and form long vortical structures beyond the diffuser trailing edge. The vortices still have a coherent structure after the diffuser outlet, in contrast with the results on the Wind Lens from Takahashi [56].

The wake of the ducted turbine is significantly larger than in the unducted case, due to higher rotor loading. Furthermore, the intense vortical activity downstream of the trailing edge of the diffuser is expected to hinder the wake mixing with the undisturbed flow, representing a problem for applications with DAWTs in series.

- *Analyse the performance of the DonQi turbine in yawed conditions*

The DonQi Windmill, about which no literature for yaw performance is present, is tested in yawed condition with an angle of 7.5° . The power produced by the blade decreases by 10.8% compared to nominal conditions. This is due to the non-axisymmetric flow at the rotor plane, that causes the thrust coefficient on the blade to vary during the revolution up to 20% in the chordwise location of maximum power. However, no stall on the blade is detected.

A separation region is formed in the diffuser suction side, in disagreement with the findings from Cresswell et al. [15]. This suggests that the relation between $\frac{L}{2R_{out}}$ and the maximum unaffected yaw angle, based on a limited number of turbines with different diffuser designs, should not be approximated merely as linear.

- *Analyse the noise characteristics*

A comparison between the results from FW-H solid and permeable formulations shows a good agreement; however, since the permeable formulation underestimates the peak at the BPF, the solid FW-H is considered a more reliable benchmark.

The analysis of the sound power density from 160 microphones around the turbine reveals that the ducted turbine produces more noise than its unducted counterpart, as a consequence of the higher flow speed. The diffraction from the diffuser walls results in a significant change of the noise directivity: the SPL increases by 10 to 15 dB in the region of low-noise above and below the rotor and by 5-6 dB upstream and downstream.

The yawed case does not show relevant noise increase, since blade stall does not occur and since the separation region on the diffuser presents low speed. The directivity in the yaw angle plane is tilted in correspondence with the turbine, while in the perpendicular plane no relevant difference with the nominal conditions is detected.

9.2. Recommendations

As final considerations, some possible improvements to the present work as well as suggestions for future developments are hereafter presented.

- In DAWT literature, it is common practice to compare the same rotor with and without a duct, often by means of the Betz limit referred to the rotor area. In this way, two devices with a different characteristic area and optimised for different situations are compared. A more fair comparison is considered to be established between a DAWT with rotor and diffuser optimised to work in such a device and an optimised bare rotor, whose rotor disk area is equal to the diffuser exit area.
- The convergence analysis showed that the results of the current study are not fully independent of the grid refinement. The comparison with similar models suggests that no relevant changes should take place. However, performing simulations with higher resolution would be helpful to have a final statement on the grid convergence, both for the fluid-dynamic and acoustic part.
- An experiment of the DonQi Windmill would be needed to validate the acoustic results. This kind of experiments have been done in the past, but without collecting data for the acoustic

part. Reproducing them would provide useful insights on the current results, especially for what concerns the grid behaviour and the directivity.

- All the phenomena related to the tip vortices formation, as well as the aerodynamic performance at the end of the blade, are strongly related to the tip clearance. The current value was selected as the best one for power production purposes. By varying the distance between blade tip and diffuser, it might be possible to obtain a configuration with a trade-off between noise generation and power production.
- The diffuser of the DonQi Windmill has not been optimised after the optimisation of the blade. Also keeping in mind the current results, a different shape might be more suitable both for power production and for acoustic emissions, with an optimum that could be reached. An improvement in the design of the diffuser should also take into account yawed inflow conditions, which cause a significant decrease in the DAWT performance with the current setup.
- The Gurney flap, often used in Diffuser Augmented Wind Turbines, has not been used in the current study. An investigation of its effects, commonly claimed to be beneficial for power production, on the noise emissions would be of interest and lead to new optimisation paths together with the diffuser.

Bibliography

- [1] K. Abe, M. Nishida, A. Sakurai, Y. Ohya, H. Kihara, E. Wada, and K. Sato. *Experimental and numerical investigations of flow fields behind a small wind turbine with a flanged diffuser*. Journal of Wind Engineering and Industrial Aerodynamics 93, 2005, 951–970.
- [2] GEA (Global Energy Assessment). *Towards a Sustainable Future*. Cambridge University Press, Cambridge, UK and New York, NY, USA and the International Institute for Applied Systems Analysis, Laxenburg, Austria, 2012.
- [3] R. Begum and M.A. Basit. *Lattice Boltzmann Method and its application to fluid flow problems*. European Journal of Scientific Research, ISSN 1450-216X Vol.22 No.2 (2008), pp.216-231.
- [4] R. D. Berendt, E.R.L. Corliss, and M.S. Ojalvo. *Quieting: a practical guide to noise control*. National Bureau of Standard Handbooks, 119.
- [5] Y. Bill Bao and J. Meskas. *Lattice Boltzmann Method for Fluid Simulations*. 2011.
- [6] R. Bontempo and M. Manna. *Solution of the flow over a non-uniform heavily loaded ducted actuator disk*. J. Fluid Mech. (2013), vol. 728, pp. 163 195.
- [7] J. Boudet, J.F. Monier, and F. Gao. *Implementation of a Roughness Element to Trip Transition in Large-eddy Simulation*. Journal of Thermal Science Vol.24, No.1 (2015) 30, 2015.
- [8] T.F. Brooks, D.S. Pope, and M.A. Marcolini. *Airfoil self-noise and predictions*. NASA reference publication 1218, 1989.
- [9] G. A. Brès, F. Pérot, and D. M. Freed. *Properties of the Lattice-Boltzmann Method for Acoustics*. 15th AIAA/CEAS Aeroacoustics Conference, AIAA Paper 2009-3395, May 2009.
- [10] D. Casalino. *An advanced time approach for acoustic analogy predictions*. Journal of Sound and Vibration 261, 2003, 583-612.
- [11] D. Casalino, A. Hazir, and A. Mann. *Turbofan broadband noise prediction using the lattice boltzmann method*. AIAA Journal, 2017, doc 10.2514/1.J055674, .
- [12] D. Casalino, A.F.P. Ribeiro, and E. Fares. *Facing rim cavities fluctuations modes*. Journal of Sound and Vibration 333, 2014, 2812-2830, .
- [13] S. Chen and G.D. Doolen. *Lattice Boltzmann method for fluid flows*. Annu. Rev. Fluid Mech. 1998, 30, 329-364.
- [14] Exa Corporation. *PowerCASE User's Guide*. 2017.
- [15] N.W. Cresswell, G.L. Ingram, and R.G. Dominy. *The impact of diffuser augmentation on a tidal stream turbine*. Ocean Engineering 108(2015)155–163, 2015.
- [16] G. de Oliveira, R.B. Pereira, D. Ragni, F. Avallone, and G.J.W. van Bussel. *How does the presence of a body affect the performance of an actuator disk ?* Journal of Physics: Conference Series 753 (2016) 022005.

- [17] O. de Vries. *Fluid Dynamic Aspects of Wind Energy Conversion*. AGARDograph No.243, 1979.
- [18] P. di Francescantonio. *A new boundary integral formulation for the prediction of sound radiation*. Journal of Sound and Vibration 202 (4), 1997, 491-509.
- [19] V.V. Dighe, F. Avallone, and G.J.W. Van Bussel. *Computational study of diffuser augmented turbine using actuator disc force method*. Int. J. Comp. Meth. and Exp. Meas., Vol. 4, No. 4 (2016) 522–531, 2016.
- [20] Wind Europe. Wind in power: 2016 european statistics, 2017. URL <https://windeurope.org/wp-content/uploads/files/about-wind/statistics/WindEurope-Annual-Statistics-2016.pdf>.
- [21] Wind Europe. Wind energy in europe: Scenarios for 2030, 2017. URL <https://windeurope.org/wp-content/uploads/files/about-wind/reports/Wind-energy-in-Europe-Scenarios-for-2030.pdf>.
- [22] F. Farassat and G.P. Succi. *The prediction of helicopter discrete frequency noise*. Vertica 7 (4), 1983, 309-320.
- [23] J.E. Ffowcs-Williams and L.H. Hall. *Aerodynamic sound generation by turbulent flow in the vicinity of a scattering half plane*. Journal of FluidMechanics, 40(4):657–670, 1970.
- [24] IPCC (Intergovernmental Panel for Climate Change). Climate change 2013: The physical science basis, 2013. URL <http://www.ipcc.ch/report/ar5/wg1/>.
- [25] K.M. Foreman and B.L. Gilbert. *Experimental Demonstration of the Diffuser-Augmented Wind Turbine Concept*. Journal of Energy, 3(4), 1979, 235 – 240, 1979.
- [26] K.M. Foreman and B.L. Gilbert. *Further investigations of diffuser augmented wind turbines, part I and II*. Grumman Research Department, New York, 1979.
- [27] K.M. Foreman, B.L. Gilbert, and R.A. Oman. *Diffuser Augmented Wind Turbines*. Fluid Dynamics Laboratory, Research Department, Grumman Aerospace Corporation, 1978.
- [28] I. Ginzbourg and P.M. Adler. *Boundary flow condition analysis for the three-dimensional lattice Boltzmann model*. Journal of Physics II, 1994, 4:191–214.
- [29] Z. Guo, C. Zheng, and T.S. Zhao. *A Lattice BGK Scheme with General Propagation*. Plenum Publishing Corporation, 2002, 0885-7474/01/1200-0569/0.
- [30] M.O.L. Hansen, N.N. Sørensen, and R.G.J. Flay. *Effect of placing a diffuser around a wind turbine*. Wind Energ. 2000; 3:207–213.
- [31] I. Hashem, M.H. Mohamed, and A.A. Hafiz. *Aero-acoustics noise assessment for Wind-Lens turbine*. Energy 118, 2017, 345-368.
- [32] D. Hermann. *A Study of the Suitability of PowerFLOW as an Educational Engineering Design tool for Undergraduate Students*. Institute for Aerodynamik und Gasdynamik University of Stuttgart at the University of Colorado / Center for Aerospace - Structures.
- [33] O. Igra. *Research and development for shrouded wind turbines*. Energy Cont. and Momt Vol. 21. pp. 13 to 48. 1981.
- [34] M. Iwasaki. *The experimental and theoretical investigation of windmills*. Reports of Research Institute for Applied Mechanics, 2(8), 1953, 181 – 229.

- [35] P. Jamieson. *Generalized limits for energy extraction in a linear constant velocity flow field*. Wind Energy 2008, 11, 445–457.
- [36] W. Jun Zhu. *Modelling Of Noise From Wind Turbines*. Mechanical Department, DTU, 2004.
- [37] T.A. Khamlaj and M.P. Rumpfkeil. *Theoretical Analysis of Shrouded Horizontal Axis Wind Turbines*. Energies 2017, 10, 38.
- [38] F.B.J. Konijn and H.W.M. Hoeijmakers. *One dimensional flow theory for diffuser augmented wind turbines*. University of Twente, 217, 2010, p.9.
- [39] W.D. Lubitz and A. Shomer. *Wind loads and efficiency of a diffuser augmented wind turbine (DAWT)*. Proceedings of The Canadian Society for Mechanical Engineering International Congress 2014, 2014.
- [40] A. Mani. *On the reflectivity of sponge zones in compressible flow*. Center for Turbulence Research, Annual Research Briefs 2010.
- [41] S. Marié, D. Ricot, and P. Sagaut. *Comparison Between Lattice Boltzmann Method and Navier Stokes High Order Schemes for Computational Aeroacoustics*. Journal of Computational Physics, Vol. 228, No. 4, 2009, pp. 1056–1070.
- [42] S. Mendez, M. Shoeybi, S.K. Lele, and P. Moin. *On the use of the Ffowcs Williams-Hawkings equation to predict far-field jet noise from large-eddy simulations*. Under consideration for publication in International Journal of Aeroacoustics.
- [43] S. Mertens. *Wind Energy in the Built Environment*. PhD dissertation, Delft University of Technology, 2006.
- [44] National Aerospace Laboratory (NLR). *Evaluatie en verbetering van de prestaties van een kleinschalige diffuser augmented wind turbine (dawt); 1e fase*. 2008.
- [45] National Aerospace Laboratory (NLR). *Ontwerp van een kleinschalige diffuser augmented wind turbine (dawt); 2e fase*. 2008.
- [46] S. Oerlemans. *An explanation for enhanced amplitude modulation of wind turbine noise*. NLR, Report NLR-CR-2011-071.
- [47] S. Oerlemans. *Introduction to aeroacoustics*. Lecture slides, TU Delft, 2016.
- [48] S. Oerlemans, P. Sijtsma, and B. Méndez Lopez. *Location and quantification of noise sources on a wind turbine*. Journal of Sound and Vibration 299 (2007) 869–883.
- [49] Y. Ohya and T. Karasudani. *A Shrouded Wind Turbine Generating High Output Power with Wind-lens Technology*. Energies 2010, 3, 634–649.
- [50] D.G. Phillips. *An investigation on diffuser augmented wind turbine design*. Doctoral Thesis, University of Auckland, New Zealand, 2003.
- [51] W.J. Rainbird and G.M. Lilley. *A Preliminary Report on the Design and Performance of a Ducted Windmill*. Report (102), 1956.
- [52] Kyushu University division of renewable energy dynamics RIAM. *Offshore hybrid energy farm experiment in hakata-bay with wind-lens turbines*. URL http://www.riam.kyushu-u.ac.jp/windeng/en_Hakatawan.html.

- [53] S.W. Rienstra and A. Hirschberg. *An Introduction to Acoustics*. Eindhoven University of Technology, 2016.
- [54] T.D. Rossing. *Springer handbook of acoustics*. Springer Science+Business media, LLC, New York, 2007.
- [55] M. Sanuki. *Studies on biplane windvanes ventilator-tubes and cup anemometers*. Papers in meteorology and geophysics, 1(2), 1950, 279 – 290.
- [56] S. Takahashi, Y. Hata, Y. Ohya, T. Karasudani, and T. Uchida. *Behavior of the blade tip vortices of a wind turbine equipped with a brimmed-diffuser shroud*. Energies 2012, 5, 5229-5242.
- [57] J. Tang, F. Avallone, and G.J.W. Van Bussel. *Experimental study of flow field of an airfoil shaped diffuser with a porous screen simulating the rotor*. Int. J. Comp. Meth. and Exp. Meas., Vol. 4, No. 4 (2016) 502–512, 2016.
- [58] P.D.C. ten Hoppen. *An Experimental and Computational Investigation of a Diffuser Augmented Wind Turbine*. Master Thesis, Delft University of Technology, 2009.
- [59] G.J.W. van Bussel. *The Science of Making More Torque from Wind: Diffuser Experiments and Theory Revisited*. IOP Publishing: Bristol, UK, 2007; Volume 75.
- [60] W.C.P. Van der Velden. *Computational aeroacoustics approaches for wind turbine blade noise prediction*. PhD dissertation, Delft University of Technology, 2017.
- [61] F.A. Van Dorst. *An improved design for a diffuser augmented wind turbine*. Master Thesis, Delft University of Technology, 2011.
- [62] A. von Betz. *Energieumsetzungen in Venturidusen*. Die Naturwissenschaften, 10, 160–164, 1929.
- [63] M.J. Werle and W.M. Presz. *Ducted wind/water turbines and propellers revisited*. J. Propuls. Power 2008, 24, 1146–1150.
- [64] Q. Zou and X. He. *On pressure and velocity boundary conditions for the lattice Boltzmann BGK model*. Journal of Physics 9, 1997, 1591-1598.